Measurement of seawater refractive index and salinity by means of optical refraction

Instrumentation and Measurement Science

Øyvind Aasen Tengesdal

A thesis submitted in

fulfillment of the requirement for the award of the

Degree of Master of Science

DEPARTMENT OF PHYSICS AND TECHNOLOGY

UNIVERSITY OF BERGEN

MAY 2012

I hereby declare that this thesis entitled “Measurement of seawater refractive index and salinity by means of optical refraction” is the result of my own research except as cited in the references. This thesis has not been accepted for any degree and is not concurrently submitted in candidature of any other degree.

Signature :

Student : Øyvind Aasen Tengesdal

Date : 20th of May, 2012

Supervisor : Professor Lars Egil Helseth

For my beloved wife and my two children

Acknowledgment

Several people has contributed to the work presented in this thesis. I want to start by placing a special thanks to my supervisor Professor Lars Egil Helseth. He has answered every question I have had, at all hours of the day, through out the last year. He has given invaluable inputs to both instrument construction and thesis writing. I consider myself lucky to have a supervisor of such insight and dedication.

I want to thank "The Michelsen Center for Industrial Measurement Science and Technology" for the project funding, making it possible to build a prototype instrument. The mechanical workshop of the Department of Physics and Technology has built several cabinet components and has shown great patience with my hand sketched blueprints. Their contribution to the construction of the instrument has been important. Scientist Emanuele Reggiani and Staff Engineer Solveig Kringstad from the "Bjerkenes Center for Climate Research" provided assistance with the construction of seawater samples and measurements of practical salinities. For this I am very grateful. Head Engineer Werner Olsen and Staff Engineer Per Heradstveit at the Department of Physics and Technology has provided excellent help and assistance with electronic circuit welding. I want to thank my fellow students, particularly Kristian Haar, Rolf K. Hjelmeland and Alexandre Vial, for stimulating discussions and excellent technical input during the last year.

I want to thank my wife for not being too upset over late nights in front of the computer, and my two children for taking my mind of this project. I am very grateful for the babysitting done by my mother and my parents-in-law the last six weeks before the deadline, making it possible to complete the thesis on time. I want to thank my father and my brother for proof reading the thesis and for giving valuable advice in the finishing phase of the project. Lastly I want to

pay tribute to the excellent teaching staff at the Royal Norwegian Naval Academy for providing my basic electrical engineering education, and the Royal Norwegian Navy for giving me the opportunity to expand my academic education.

Øyvind Aasen Tengesdal, Bergen

Abstract

The aim of this work has been to construct and test a compact refractometer for accurate measurement of seawater refractive index and salinity. The specific goal was to measure the refractive index of the water sample with an accuracy of 10^{-6} refractive index units (RIU). The size goal was set to be a cylindrical container with a height of $80\,mm$ and a diameter of $36\,mm$.

The realization of the instrument resulted in a cuboid measurement chamber with a length of $70\,mm$ and a width of $40\,mm$ and an additional electronics compartment. The instrument's basic concept is a laser beam which is transmitted through a prism setup. The water sample is brought into the sample compartment by using a water pump. The lateral displacement of the beam, which changes according to the refractive index of the water sample, is then detected by a position sensitive light detector and the temperature of the water sample is measured with a thermistor. The photocurrent from the detector is amplified and acquired to a computer along with the temperature voltage from the thermistor. A computer simulation has been made to accurately design and describe the instrument. The experiments were conducted by measuring the laser beam displacement and temperature of 10 seawater samples with practical salinity ranging from 0 to 36, as well as 10 samples of crystalline sodium chloride dissolved in pure water with concentration ranging from 0 to $4\,{}^{g}/_{100g}$. The refractive index of the samples were then calculated from empirical algorithms.

The results show that the instrument is capable of measuring the refractive index of seawater with an precision of $1.5 \cdot 10^{-4}$ RIU over long time periods, up to several hours. The main contribution to this uncertainty has been identified to be a temperature dependent drift in the position detector output. The precision within intervals of minutes was found to be $1.2 \cdot 10^{-5}$ RIU.

Contents

Declaration iii

Dedication iv

Acknowledgment v

Abstract viii

List of figures xiv

List of tables xv

List of appendices xvi

List of common symbols xvii

List of acronyms and abbreviations xix

1 Introduction 1

1.1 Background of thesis 1

1.2 Specific objective of thesis 2

1.3 Outline and organization 3

2 Theory and background 5

2.1 Propagation of light 6

2.1.1 Dispersion 6

2.1.2 Polarization and electric fields 9

2.1.3 Thermodynamic relation 14

2.1.4 Sellmeier equation 16

2.1.5 Reflection and refraction 17

2.1.6 Reflectance and transmittance 21

2.2 Light sensing semiconductors 25

2.2.1 P-n junction 25
2.2.2 Photodiode operation 26
2.3 Measurement of refractive index 28
2.3.1 Refractometric methods 28
2.3.2 Interferometric methods 31
2.3.3 Total internal reflection 33
2.3.4 Other techniques 36
2.3.5 Comparison of methods 38
2.4 Basic principles of instrument components 39
2.4.1 Position sensitive detector 39
2.4.2 Quadrant cell photodiode 43
2.4.3 NTC Thermistor 47
2.4.4 Prisms 47
2.4.5 Water samples 52
2.5 Measurement errors and reduction techniques 59
2.5.1 Laser noise 60
2.5.2 Optical sensor noise 61
2.5.3 Shot noise 61
2.5.4 Johnson noise 62
2.5.5 Generation recombination noise 65
2.5.6 Leakage current and ambient light 66
2.5.7 Total noise in optical sensor 67
2.5.8 Amplifier noise 67
2.5.9 Noise and error in data acquisition 68
2.5.10 Total uncertainty 70

3 Instrument design and experimental setup 73
3.1 Instrument setup 73
3.2 Optimization of instrument geometry 77
3.3 Optical power loss 79
3.4 Data acquisition software 81
3.5 Sample frequency 81

4 Experimental results 83
4.1 Measurement of noise sources 83
4.1.1 Data acquisition error 83
4.1.2 Detector noise 84
4.1.3 Laser noise 85
4.2 Thermistor Calibration 90
4.3 Results from Position Sensitive Device 91

4.3.1 Seawater samples 92
4.3.2 Sodium chloride solution 93
4.4 Results from quadrant cell photodiode 94

5 Discussion and Conclusion 97
5.1 Noise 97
5.1.1 Data acquisition noise 97
5.1.2 Detector noise 98
5.1.3 Laser noise 99
5.2 Measurement uncertainty 100
5.2.1 Position sensitive detector 101
5.2.2 Quadrant cell photodiode 104
5.3 Theoretical fit 106
5.3.1 Position sensitive detector 106
5.3.2 Quadrant cell photodiode 108
5.4 Biological fouling errors 109
5.5 Further work 111
5.6 Conclusion 112

References 113

List of Figures

2.1 Polarization resonance 9
2.2 Polarization by electric field 10
2.3 Local electric field at an atom 12
2.4 Geometrical description of the surface area of a spherical cavity 12
2.5 Wave reflection and transmission at an interface 18
2.6 Transmittance and reflectance as a function of the incident angle on a prism water interface where $n_i = 2.58$ and $n_t = 1.33$. 23
2.7 The transmitted angle as a function of the incident angle on a prism-water interface where $n_i = 2.58$ and $n_t = 1.33$. 24
2.8 Schematic overview of a Pulfrich refractometer 29
2.9 Simplified refractometric setup 29
2.10 Schematic overview of a Michelson Interferometer 31
2.11 Schematic overview of a total internal reflection refractometer 34
2.12 Reflected intensity from SPR as a function of incident angle 37
2.13 Schematic cross section of position sensitive detector 40
2.14 Diagram of signal processing circuit Hamamatsu C3683-01 42
2.15 Frequency dependence of gain 42
2.16 Driver circuit of quadrant cell photodiode module 44
2.17 Circular laser beam on quadrant detector 45
2.18 Theoretical position voltage ratio as a function of laser spot displacement X 46
2.19 Voltage divider circuit 48
2.20 Dispersion of prisms 50
2.21 Refractive index of $NaCl$ solution as function of concentration in % 54
2.22 Refractive index as a function of salinity 56
2.23 Refractive index as a function of temperature 57
2.24 Refractive index as a function of pressure in dbar 58
2.25 Model of the predicted noise sources in the instrument. 70

3.1 2-D sketch of instrument with measures in cm. The height of the cabinet walls are 4 cm. 74
3.2 Pictures from the experimental setup 76

4.1 Measured data acquisition mean voltage and its standard deviation for the last 1000 values 84
4.2 Measured dark detector mean voltage and its standard deviation for the last 1000 values 85
4.3 Measured mean SUM voltage and its standard deviation for last 1000 values 86
4.4 Measured mean laser position voltage and its standard deviation for the last 1000 values 87
4.5 Measured laser position voltage standard deviation for water sample 88
4.6 Histogram showing number distribution of laser position deviation magnitude with a superimposed gaussian curve with zero mean. 89
4.7 Picture of laser beam after passing through instrument. Scale of figure in μm 90
4.8 Calibration curve fit for NTC Thermistor 91
4.9 Measured displacement of laser spot versus salinity of seawater samples. 93
4.10 Standard deviation of measured values in figure 4.9. 93
4.11 Measured displacement of laser spot versus concentration of sodium chloride solution samples. 94
4.12 Standard deviation of measured values in figure 4.11. 94
4.13 Measured position voltage ratio versus concentration of sodium chloride solution samples. 95

5.1 Maximum deviation in all seawater series 102
5.2 Hysteresis in seawater series 103
5.3 Maximum deviation in all $NaCl$-series 104
5.4 Hysteresis in $NaCl$-series 104
5.5 Standard deviation of measured position 105
5.6 Calculated refractive index versus measured displacement of laser spot. Plot of equation 5.1 superimposed on measured data. 107
5.7 Calculated refractive index versus measured displacement of laser spot. Plot of equation 5.1 superimposed on measured data. 108
5.8 Calculated refractive index versus measured displacement of laser spot. The adjusted computer simulation is superimposed on measured data. 109

A.1 Laser beam propagation calculation 122
A.2 Laser beam position as a function of refractive index of seawater 124

D.1 Main virtual instrument block diagram 132
D.2 Acquisition loop block diagram 133

List of Tables

2.1	Comparison of methods for measurement of refractive index	38
2.2	Sellmeier coefficients and refractive index for prism substances at room temperature.	49
2.3	Water samples used in the experiment	53
2.4	Coefficients used in simplified Seaver-Millard equation	58
3.1	Specifications of instrument components	75
5.1	Measured data acquisition error and noise	98
5.2	Measured detector noise	98
5.3	Measured laser noise	99
B.1	Region I coefficients	127
B.2	Region II coefficients	127
B.3	Region III coefficients	127
B.4	Region IV coefficients	128
E.1	Mass fractions of seawater ions	134

List of Appendices

A Refractive index as function of beam position displacement 121

B Empirically derived optical equations of state 125

C Statistical representation of noise sources 129

D Screenshots of LabView program 131

E Seawater composition 134

List of common symbols

Vectors are denoted with bold letters

Symbol	Quantity	Unit
n	Refractive index of a medium	Ratio
v_p	Phase speed of light in a medium	m/s
ϵ	Permittivity of a medium	F/m
$\mathbf{p}$	Electric dipole moment vector	$C \cdot m$
$\mathbf{P}$	Polarization vector	C/m^2
q	Electric charge	C
$\mathbf{E}$	Electric field	V/m
$\mathbf{B}$	Magnetic field	T
$\mathbf{k}$	Wavenumber vector	$1/m$
ω	Angular frequency	rad/s
ω_0	Resonance angular frequency	rad/s
σ_s	Surface charge density	C/m^2
I	Intensity	W/m^2
P_x	Power	W
η	Quantum efficiency	Ratio
i_p	Photocurrent	A
S	Responsivity	A/W
Φ_p	Photon flux	$1/s$
Φ_e	Electron flux	$1/s$

Symbol	**Quantity**	**Unit**
X	Laser beam displacement	m
G	Current to voltage gain of amplifier	V/A
T	Temperature	^oC or K
P_r	Pressure	$dbar$
R	Resistance	Ω
ΔQ	Quantity of heat	J/s
c	Specific heat constant	$J/Kg{\cdot}K$
α	Attenuation coefficient	$1/m$
f	Frequency	Hz
τ_0	Average charge carrier lifetime	s
τ_d	Electron transition time	s
ρ	Density	kg/m^3
$\bar{x}$	Mean value of a population	
σ	Standard deviation	

List of acronyms and abbreviations

Abbreviation	Explanation
LASER	Light amplification by stimulated emission of radiation
USB	Universal serial bus
CCD	Charge-coupled device
DC	Direct Current
PSD	Position sensitive detector
SPR	Surface plasmon resonance

Chapter 1

Introduction

1.1 Background of thesis

Measurement of sea water salinity is important for several industrial, research related and military applications. Oceanography plays a leading role in climate research and the need for precise measurements of oceanographic variables is imperative. The research history on this particular topic is extensive, spanning over 100 years and using different techniques such as measuring dry residue after evaporation, titration of seawater against silver nitrate and in recent times measurement of electrical conductivity.[1, 2] The overall goal has been to measure the seawater salinity as accurately as possible.

There are several ways to quantify salinity in sea water. An intuitive way of expressing salinity is in terms of mass fraction of dissolved solids per kilogram seawater and denoted S_R. It is expressed in units $[g/_{100g}]$ and was used in conjunction with the evaporation method. The introduction of conductivity measurements called for a new reference standard. The ratio of the conductivity of the water sample to the conductivity of a specific reference solution of potassium chloride defines the Practical Salinity Scale of 1978. Even if the measure is dimensionless, the term practical salinity unit (psu) is used to describe the magnitude, denoted S_p. The relationship between the two ways of quantifying salinity is [3, 4] :

$$S_R \approx 0.10047 \cdot S_p.$$

Modern sensors for measuring sea water salinity are primarily based on conductivity measurements. They are relatively simple constructions, inexpensive and

reliable. The measurement principle is based on measuring the conductivity of sea water by sending a current pulse between an anode and a cathode.[5] The relationship between conductivity and salinity is heavily dependent on temperature and pressure. Therefore both a temperature sensor of some sort, and a pressure sensor, is required to make a valid measurement of the salinity. The sensors system is thereby named Conductivity-Temperature-Pressure or CTD. The CTD sensor has a given reliability and accuracy based on these three measurements.[6]

Conductivity sensors will only detect the concentration of conductive materials in specific water samples. Other non-conductive materials in a water sample will not be detected, but will contribute to the overall density of the sample. A measurement of the refractive index of the water sample could account for this contribution. Refractive index can be measured in a number of optical techniques, but due to technological limitations it has not found widespread use. [7, 8]

Advances in both laser and light detector technology in recent decades, however, have made optical techniques relevant.[6] Several instruments based on optical techniques have been developed [9, 10, 11, 12], and laboratory type instruments are commercially available. The development of working in-situ sensors has produced some results [13], but has not resulted in equipment superior to the existing conductivity sensors.[14] Thus its is therefore interesting to investigate the performance of an optical instrument for refractive index measurement.

1.2 Specific objective of thesis

In this thesis we will investigate the realizability and performance of a refractive index and salinity measurement sensor based on the principle of the refractometer. The general idea on which this thesis is based is a theoretical article from 2010 by Philippe Grosso et al. in Ref [6]. It describes the concept of using a laser beam refracted in a prism to seawater surface, and a state of the art position sensitive detector to measure the displacement of the laser beam.

My specific goal is to make a compact prototype refractometric instrument with an accuracy in the refractive index measurement of 10^{-6} refractive index units. The thesis will cover the theoretical background, the actual construction and the experimental testing of the refractometer. The instrument will be tested in a laboratory environment, but several design considerations will be

decided by in-situ requirements. The self imposed size requirement of my prototype is based on commercially available Aanderaa Data Instruments (AADI) modular oceanographic sensors [15], which are cylindrical constructions with a diameter of $36\,mm$ and a height of $80\,mm$. As the construction of a cylindrical measurement chamber was considered unpractical, a cuboid design with similar volume is the specific goal.

The experiments will be conducted by measuring the salinity of two sets of water samples. The first set is composed of seawater samples of different practical salinity. The second set of samples is composed of sodium chloride dissolved in pure water at different concentrations. We will conduct experiments using two different detection techniques to evaluate which is best suited for the task. The main focus will be on using a position sensitive device, while the possibility of using a quadrant cell photodiode will be explored in a limited experiment.

1.3 Outline and organization

The work will be presented in the following manner:

- Chapter 2 will be used to explain the underlying physical theory of light propagation, refractive index and the concept of refraction. The basic physics of the light sensing detectors is explained. It then covers a presentation and brief discussion on different methods for measuring refractive index. The relevant principles of the electrical and optical components in the instrument, as well as the water samples, are presented before the last part of the chapter gives an account of the sources of measurement error in the system.

- Chapter 3 describes the construction of the instrument, covering all design considerations and presenting the final experimental setup.

- Chapter 4 starts by presenting experimentally determined sources of noise and error. It presents the results of the experiments for sample sets of seawater and sodium chloride solutions, measured with the position sensitive detector. The last part presents the results of the limited experiment with the quadrant cell photodiode.

- Chapter 5 contains an evaluation of the achieved experimental performance

of the instrument, along with comments and explanations on the behavior of the experiment. A brief discussion on the impact of biological fouling is given, before potential improvements of the instrument are presented. The last part of the chapter contains the conclusion and focuses on how well the specific objectives of the thesis has been reached.

Chapter 2

Theory and background

This chapter will present the necessary theoretical background to understand the operation of the instrument that has been constructed. The first section describes the concept of refractive index, as well as its dependence on the frequency on the incident light. The refractive index relation to the concentration of different materials in a mixture, such as in seawater, and also the temperature and pressure is then explained. The propagation of a plane wave with an oblique incident on an interface between to materials of different refractive index is described by Snells law, which will be derived in this section along with the Fresnel coefficients describing the ratios of the light power being transmitted and reflected in the given interface. The next section describes the function of light sensitive semiconductor devices and how a p-n junction diode can be used to measure the intensity of incident light.

We go on to describes various methods of measuring refractive index. The methods are presented and evaluated to a set of criteria to determine which methods are best suited to perform in a given instrument setup. Then the basic functions and properties of the electrical and optical components of the instrument, as well as the water samples used in the experiment, will be presented. The last part of the chapter describes sources of noise which are known to be present in a instrument based on optical detection.

2.1 Propagation of light

The index of refraction, n, of an optical material is defined as the ratio of the speed of light in vacuum, c, to the phase speed of light in the medium, v_p.

$$n = \frac{c}{v_p}. \tag{2.1}$$

The speed of light in vacuum is by definition $c = \sqrt{\frac{1}{\epsilon_0 \mu_0}}$, where ϵ_0 is electromagnetic permittivity of free space and μ_0 is electromagnetic permeability of free space. The phase speed in a medium can be derived from the wave equation for electromagnetic waves to be $v_p = \sqrt{\frac{1}{\epsilon_r \mu_r}}\sqrt{\frac{1}{\epsilon_0 \mu_0}}$, where ϵ_r is the relative permittivity of the medium and μ_r is the relative permeability of the medium.[16] For non-magnetic substances the relative permeability is very close to unity, which further simplifies the expression. This gives a the following expression for the refractive index:

$$n = \sqrt{\epsilon_r \epsilon_0} = \sqrt{\epsilon}, \tag{2.2}$$

where ϵ is the permittivity of the medium.

2.1.1 Dispersion

The relative permittivity, and also the refractive index, is a function of the frequency of the electromagnetic wave which passes through the medium. This phenomenon is referred to as dispersion. The description of the physical nature of dispersion would require a complex derivation using quantum electrodynamics taking into account the interactions of molecules and their environment. It is however possible to derive a simple classical model of dispersion which has been found to adequately describe many molecular systems. [17]

If a non-polar molecule, having no permanent dipole in the absence of an external field, is subject to an electric field, the positive nuclei and the negative electrons would be displaced a distance $\mathbf{r}$ relative to the center of the molecule to create a dipole moment. The dipole moment is defined as $\mathbf{p} = q\mathbf{r} = -e\mathbf{r}$, where e is the electron charge and $\mathbf{r}$ is the displacement vector. If we consider a substance with a given number of molecules per unit volume N, we can define polarization $\mathbf{P} = N\mathbf{p}$ as the dipole moment per unit volume.[18]

To determine how polarization is related to the frequency of the electric

field, we have to express the displacement of an electron from its equilibrium, $\mathbf{r}$, as a function of the electric field. Lorentz law states that an electron subjected to an electromagnetic field is acted upon by a force [17]:

$$\mathbf{F} = -e(\mathbf{E} + \mathbf{v} \times \mathbf{B}), \tag{2.3}$$

where $\mathbf{E} = \mathbf{E}_0 e^{i(\mathbf{k}\cdot\mathbf{r}-\omega t)}$ is the electric field, $\mathbf{B} = B_0 e^{i(\mathbf{k}\cdot\mathbf{r}-\omega t)}$ is the magnetic field and $\mathbf{v}$ is the velocity of the electron with charge $-e$. $\mathbf{k}$ is the wave number vector giving the propagating direction of the electromagnetic wave . If we assume that $\mathbf{v}$ is small compared to the speed of light in vacuum, the contribution from the magnetic field will be negligible. This can be shown by the use of Faradays law on differential form:

$$\nabla \times \mathbf{E} = -\frac{\partial \mathbf{B}}{\partial t}.$$

If we express the electric field curl as $\nabla \times \mathbf{E} = \mathbf{k} \times \mathbf{E}$ we get:

$$\mathbf{k} \times \mathbf{E} = i\omega \mathbf{B}. \tag{2.4}$$

We know that $\omega = 2\pi \mathrm{f}$, that $k = {}^{2\pi n}/_{\lambda}$, and that $c = \lambda f$. Since $\mathbf{E} \perp \mathbf{k}$, and hence $|\mathbf{k} \times \mathbf{E}| = k\,|\mathbf{E}|$, we can write:

$$|\mathbf{B}| = \frac{n}{c}\,|\mathbf{E}|\,.$$

If we, as in equation 2.3, express the cross product of the velocity vector of the electron and the magnetic field, we get

$$|\mathbf{v} \times \mathbf{B}| = n\frac{v}{c}\,|\mathbf{E}|\,,$$

if we assume that the angle between the vectors $\mathbf{v}$ and $\mathbf{B}$ is 90^o. This means that if ${}^{nv}/_{c} \ll 1$ then $|\mathbf{v} \times \mathbf{B}| \ll |\mathbf{E}|$. This means that we can simplify equation 2.3 to the following:

$$\mathbf{F} \approx -e\mathbf{E}.$$

Even though the displacement of electrons in an atom is governed by quantum mechanics, it is valid to express the force $\mathbf{Q}$ holding an electron in equilibrium by a simple approximation. This could be derived from a Taylor series expansion of Coloumbs law, where the nucleus attracts the electron, and the other electrons repel the electron.[17] If we only keep the first order term of the Taylor expansion we get a quasi-elastic Hooke's law equivalent, valid for small

values of displacement:

$$\mathbf{Q} = -\kappa \mathbf{r}, \tag{2.5}$$

where κ is a constant determined by the number of electrons and nuclides in the atom or molecule. If m is the mass of the electron, Newtons second law postulates that

$$\mathbf{F} + \mathbf{Q} = -e\mathbf{E} - \kappa \mathbf{r} = m\ddot{\mathbf{r}},$$

which is a linear inhomogeneous second order differential equation with constant coefficients. This formula does not account for the damping effects which are present in the system. For example, the vibrating electrons will emit photons which will take energy out of the system. This can be expressed by adding a term representing a resistive force $m\gamma\dot{\mathbf{r}}$ to the previous expression:

$$m\ddot{\mathbf{r}} + m\gamma\dot{\mathbf{r}} + \kappa\mathbf{r} = -e\mathbf{E}. \tag{2.6}$$

Since the electric field oscillates harmonically as $\mathbf{E} = \mathbf{E}_0 e^{-i\omega t}$, we could suggest a trail solution for $\mathbf{r}$ on the same form, $\mathbf{r} = \mathbf{r}_0 e^{-i\omega t}$. By inserting the trial solution into equation 2.6 we have a valid solution for the differential equation, where $\omega_0 = \sqrt{\kappa/m}$ is the angular resonance frequency.

$$\mathbf{r} = -\frac{e\mathbf{E}}{m(\omega_0^2 - \omega^2 - i\omega\gamma)}. \tag{2.7}$$

We have now described the electrons displacement oscillation from its equilibrium position and have determined that it is a function of the frequency of the electromagnetic wave. The polarization of the atom will be determined by the displacement of the electrons and the nucleus. If we consider that the nucleus of the atom is much heavier than the electron, we can assume that the contribution to the polarization moment is primarily determined by the electron. If we also assume that the atom only has one electron, we can express the polarization moment of the atom by $\mathbf{p} = -e\mathbf{r}$. The total polarization vector would then be the product of the number of atoms per unit volume and the polarization moment of each atom:

$$\mathbf{P} = N\mathbf{p} = -Ne\mathbf{r} = N \cdot \frac{e^2\mathbf{E}}{m(\omega_0^2 - \omega^2 - i\omega\gamma)}. \tag{2.8}$$

It is clear that the polarization is in fact a complex quantity because of the introduction of the loss mechanism mentioned earlier. Figure 2.1 shows a plot of the amplitude of equation 2.8, as well as a plot of the undamped expression.

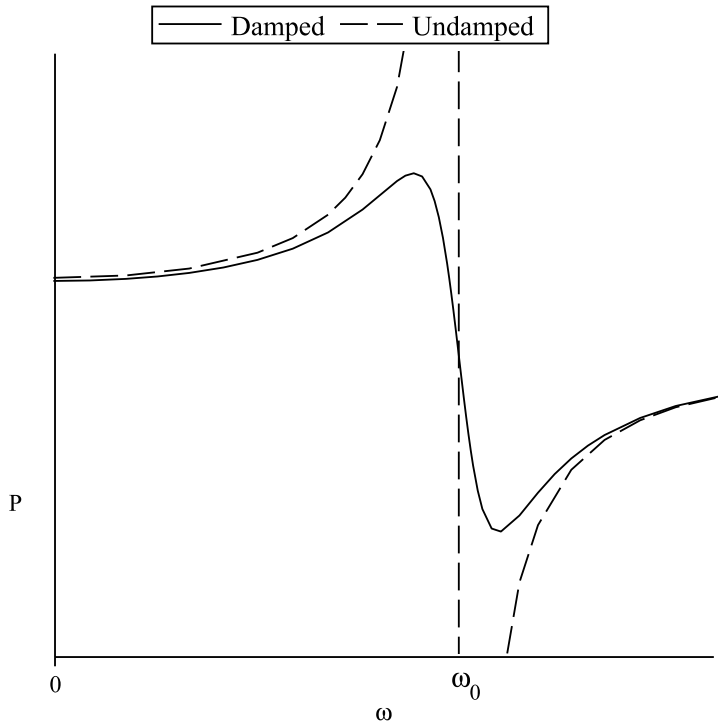

Figure 2.1: Graph showing the polarization as a function of frequency. Observe the singularity at the resonance frequency, which does not occur when damping is taken into account.

2.1.2 Polarization and electric fields

To connect the polarization to the relative permittivity and refractive index it is necessary to describe the electric field that is in fact being experienced at an atomic level. It cannot be assumed that the local electric field E_{local} at a given point in the body is the same as the field measured over body. [18]

In addition to the external electric field $\mathbf{E_0}$ being applied to a given body , the electric fields of the charges in the body will also contribute to the total field. We define the average field over a volume V' of the body at a point $\mathbf{r}_0$, referred to as the macroscopic field,

$$\mathbf{E}(\mathbf{r_0}) = \frac{1}{V'} \int dV \mathbf{e}(\mathbf{r}), \tag{2.9}$$

where $\mathbf{e}(\mathbf{r})$ is the microscopic field.[18] The electric field generated by uniform polarization can be simplified to equal the electric field of a fictitious surface

charge density $\sigma_s = \hat{\mathbf{n}} \cdot \mathbf{P}$ on the surface of the body. $\hat{\mathbf{n}}$ is the unit vector normal to the surface of the body. If this assumption is applied to an ellipsoid shape of dielectric material, as sketched in figure 2.2, the electric field produced by uniform polarization is equal to the field generated by the fictitious surface charge density on the surface of the ellipsoid. Ellipsoids have the property that a uniform polarization produces a uniform depolarization field inside the body.[18] It is possible to decompose the polarization vector into components for each axis in a three dimensional cartesian coordinate system, P_x, P_y and P_z. This gives the components of the depolarization field:

$$E_{1x} = -\frac{P_x}{\epsilon_0} M_x \,, \quad E_{1y} = -\frac{P_y}{\epsilon_0} M_y \,\text{and}\; E_{1z} = -\frac{P_z}{\epsilon_0} M_z, \tag{2.10}$$

where the factors M_x, M_y and M_z are the depolarization factors. The values are based on the ratios of the principal axes of the ellipsoid, and the sum of all three equals unity. For a sphere, their values are $M_x = M_y = M_z = \frac{1}{3}$.[18] The field

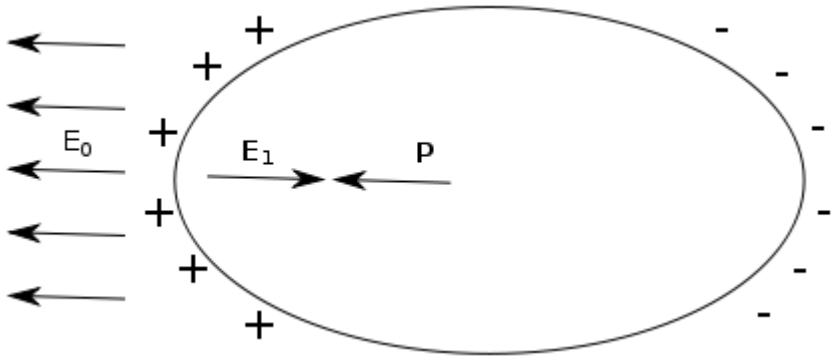

Figure 2.2: Sketch illustrating the electric field $\boldsymbol{E_1}$, established by the estimation that the uniform polarization $\boldsymbol{P}$ can be considered as creating a surface charge density on the specimen. [18]

$\mathbf{E_1}$, referred to as the depolarization field, tends to oppose the external field $\mathbf{E_0}$. A uniform applied field $\mathbf{E_0}$ will induce a uniform polarization in an ellipsoid. The relationship between the macroscopic field $\mathbf{E}$ and polarization $\mathbf{P}$ is given by the dielectric susceptibility χ.[18]

$$\mathbf{P} = \epsilon_0 \chi \mathbf{E}. \tag{2.11}$$

If we assume an ellipsoid shaped body being subjected to an external field $\mathbf{E_0}$ parallel to one of its principal axes, for instance the z-axis, we can express the macroscopic field as

$$E = E_0 - \frac{M_z P}{\epsilon_0}, \tag{2.12}$$

and then express the polarization as a function of the external field and the

depolarization factor:

$$P = \frac{\chi\epsilon_0}{1 + \chi M_z} \cdot E_0. \tag{2.13}$$

Local electric field at an atom If we consider atoms in a cubic arrangement in a volume of spherical shape, the macroscopic electric field inside the sphere is $\mathbf{E} = \mathbf{E}_0 + \mathbf{E}_1 = \mathbf{E}_0 - \frac{\mathbf{P}}{3\epsilon_0}$. If we then look at the the local field $\mathbf{E}_{local}$ that acts on the atom at the center of the sphere, it is clear that the field is a result of the contributions from all the dipoles in the sphere, as well as the external field $\mathbf{E}_0$. By assuming that the dipoles are aligned parallel to the z axis with a magnitude p, we can define the z component of this field as:

$$E_{dipole,z} = \frac{p}{4\pi\epsilon_0}\sum_i \frac{3z_i^2 - r_i^2}{r_i^5} = \frac{p}{4\pi\epsilon_0}\sum_i \frac{2z_i^2 - x_i^2 - y_i^2}{r_i^5}. \tag{2.14}$$

Because of the symmetry of the sphere and the cubical arrangement the x, y and z directions will be equivalent [18]:

$$\sum_i \frac{z_i^2}{r_i^5} = \sum_i \frac{x_i^2}{r_i^5} = \sum_i \frac{y_i^2}{r_i^5}, \tag{2.15}$$

resulting in $E_{dipole,z} = 0$. This means that the local field $\mathbf{E}_{local} = \mathbf{E}_0$ for this particular instance of lattice and geometrical shape. It is clear that the macroscopic average field is not equal to the local field.

We need to develop a model for the local field at a general lattice site and not depending on cubic symmetry. We can define $\mathbf{E}_{local}$ as a sum of the contributions from the external field $\mathbf{E}_0$ and the contribution from the dipoles in in the body. We decompose the electric field from the dipoles into three contributions, $\mathbf{E}_1$, $\mathbf{E}_2$ and $\mathbf{E}_3$ and get an expression for the local electric field at an atom:

$$\mathbf{E}_{local} = \mathbf{E}_0 + \mathbf{E}_1 + \mathbf{E}_2 + \mathbf{E}_3. \tag{2.16}$$

The sketch in figure 2.3 gives an overview of the model. $\mathbf{E}_0$ is the external field and $\mathbf{E}_1$ is the depolarization field generated by a surface charge density on the surface of the specimen. $\mathbf{E}_2$ is the Lorentz cavity field which is the field from polarization on the inside of a imaginary sphere cut out of the specimen, centered on the reference atom. By doing this the field in the region between the outer boundary of the specimen and the inner boundary created by the imaginary sphere is the sum $\mathbf{E}_1 + \mathbf{E}_2$, which is attributed to uniform polarization of the of the

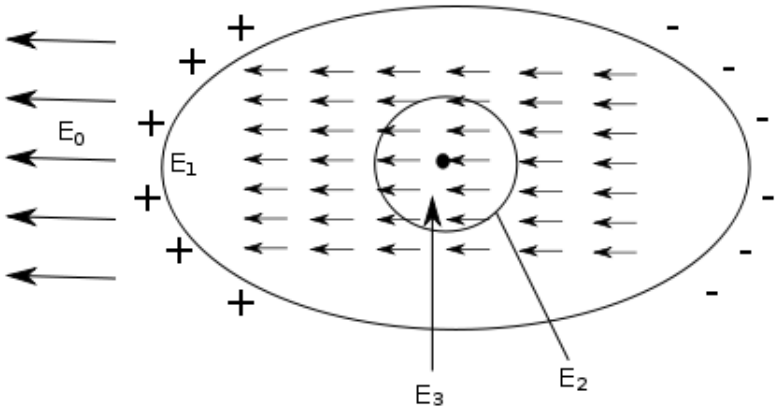

Figure 2.3: Sketch showing the fields of equation 2.16, contributing to the local electric field at an atom in the center. [18]

specimen. The dipoles at a greater distance than about 10 lattice constants from the center atom will make smoothly varying contributions to the sum in equation 2.16, and can be replaced by a surface integral. $\mathbf{E}_3$ will be the contribution from the other dipoles inside the imaginary sphere and also closer than 10 lattice constants and must therefore be considered to make discrete contributions, but due to the expected symmetry of polarization vectors inside the imagined spherical cut out, $\mathbf{E}_3$ equals zero.

To calculate the Lorentz cavity field $\mathbf{E}_2$, we let the surface charge density on the inside of the imaginary sphere cut out be defined by a a polar angle Θ from the polarization direction, as shown in figure 2.4:

$$\sigma_s = -P \cdot cos(\Theta).$$

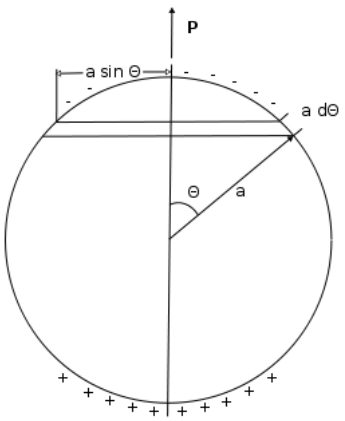

Figure 2.4: Figure of spherical cavity in a uniformly polarized medium. The infinitesimally small surface area is $dA = 2\pi a \cdot sin(\Theta) \cdot a \cdot d\Theta$. [18]

The electric field on the atom in the center of the sphere with radius

a will then be given by an integration of Coloumbs Law, where the charge dQ_c is given by the surface charge density multiplied with an infinitesimally small surface region of area $dA = 2\pi a \cdot sin(\Theta) \cdot a \cdot d\Theta$, and the unit vector from this area to the central atom is given by $\mathbf{r}$=$cos(\Theta)$.

$$\mathbf{E}_2 = -\frac{1}{4\pi\epsilon_0}\int_0^\pi \frac{dQ_c}{a^2}\mathbf{r} = -\frac{1}{4\pi\epsilon_0}\int_0^\pi \frac{\sigma_s \cdot dA}{a^2} cos(\Theta). \tag{2.17}$$

This gives the following expression for the electric field as a function of the polarization:

$$\mathbf{E}_2 = \frac{\mathbf{P}}{2\epsilon_0}\int_0^\pi cos^2(\Theta) \cdot sin(\Theta) d\Theta = \frac{\mathbf{P}}{2\epsilon_0}\left[-\frac{1}{3}cos(\Theta)\right]_0^\pi = \frac{\mathbf{P}}{3\epsilon_0}.$$

If we compare this result with that of equation 2.12 and assume a spherical outer boundary for the specimen, we see that these fields are directly opposite and the sum $\mathbf{E}_1 + \mathbf{E}_2 = 0$. For a random ellipsoid outer boundary the expression for the local electric field at the reference atom is

$$\mathbf{E}_{local} = \mathbf{E}_0 + \mathbf{E}_1 + \mathbf{E}_2 = \mathbf{E} + \frac{\mathbf{P}}{3\epsilon_0}, \tag{2.18}$$

where $\mathbf{E} = \mathbf{E}_0 + \mathbf{E}_1$ is the macroscopic electric field which can be measured. This is called the Lorentz relation.

Dielectric constant and polarizability The dielectric constant ϵ of a isotropic medium relative to vacuum is given by the macroscopic field E [18]:

$$\epsilon = \frac{\epsilon_0 E + P}{\epsilon_0 E} = 1 + \chi, \tag{2.19}$$

where χ is electric susceptibility as given in equation 2.11. If we define the molecular polarizability α in terms of the local electric field at the molecule we get

$$p = \alpha E_{local},$$

where p is the dipole moment. The polarizability is dependent on the structure and shape of the molecule. We can approximate the polarization in a medium by

a sum over the products of the molecular polarizabilities and local electric field

$$P = \sum_j N_j p_j = \sum_j N_j \alpha_j E_{local}(j), \tag{2.20}$$

where N_j is the number of molecules per unit volume, α_j is the molecular polarizability and $E_{local}(j)$ is the local electric field at the atom site j. We can now connect the dielectric constant to the polarizability through the relation between the macroscopic electric field and the local electric field given by the Lorentz equation. By inserting equation 2.18 into equation 2.20 we get

$$P = (\sum_j N_j \alpha_j)(E + \frac{P}{3\epsilon_0}),$$

which can be turned around to

$$\frac{P}{E} = \frac{\sum_j N_j \alpha_j}{1 - \frac{1}{3\epsilon_0} \sum_j N_j \alpha_j}.$$

From equations 2.11 and 2.19 we know that $P = \epsilon_0 \chi E$ and $\epsilon = 1 + \chi$ which in turn gives an expression for the relationship between the dielectric constant and the polarizability:

$$\epsilon_0(\epsilon - 1) = \frac{\sum_j N_j \alpha_j}{1 - \frac{1}{3\epsilon_0} \sum_j N_j \alpha_j}.$$

By rearranging this equation we get

$$\frac{\epsilon - 1}{\epsilon + 2} = \frac{1}{3\epsilon_0} \sum_j N_j \alpha_j, \tag{2.21}$$

which is called the Clausius-Mossotti relation. This relationship is valid for several substances, as long as the Lorentz local field can be written as $\mathbf{E} + \frac{\mathbf{P}}{3\epsilon_0}$.

2.1.3 Thermodynamic relation

If we consider a liquid material it is logical to assume that both temperature and pressure will influence the dielectric constant, because the density of molecules will be affected by a change in both temperature and pressure in the liquid. By

assuming a homogeneous liquid, the sum in equation 2.21 can be realized

$$\frac{\epsilon - 1}{\epsilon + 2} = \frac{1}{3\epsilon_0} N\alpha, \tag{2.22}$$

where N is the number of molecules per unit volume and α is the molecular polarizability. If we alter the equation as done in [19], by replacing α with molecular refractivity $A = \frac{1}{3\epsilon_0} N_A \alpha$, we get a new equation showing the dielectric constant as a function of molecular refractivity and number density,

$$\frac{\epsilon - 1}{\epsilon + 2} = \frac{N}{N_A} \cdot A, \tag{2.23}$$

where $N_A = 6.02 \cdot 10^{23}$ is Avogadros number. We know that $N = \frac{N_m}{V}$ where N_m is the number of molecules and V is the volume. The ideal gas law states that

$$P_r V = N_m kT = \frac{N_m}{N_A} RT,$$

where P_r is the pressure, T is the absolute temperature, and $R = 8.314\ {}^{J}/_{mol \cdot K}$ is the ideal gas constant.[16] The ideal gas law is not directly valid for a liquid substance, as the expression would include several corrective terms as a liquid is virtually incompressible, but the first order term would be valid as an approximation. [19] By further modification we can include this in equation 2.23 and get:

$$\frac{\epsilon - 1}{\epsilon + 2} = \frac{AP_r}{RT}, \tag{2.24}$$

This equation relates the permittivity to the molecular refractivity, the pressure and the temperature of the substance. As for instance seawater is a mixture of water and several dissolved salts, it is necessary to express the molar refractivity by a sum weighted by each of its i components. N_i is then the number density of molecules and A_i is the molar refractivity of substance i.

$$A = \sum_i A_i \cdot N_i \ where\, i = 1,\, 2,\, 3 \ldots$$

By reviewing equation 2.24 analytically it is apparent that an increase in temperature results in a decrease in the permittivity. An increase in the pressure results in an increase in the permittivity, and an increase in the molar refractivity also results in an increase in permittivity. The refractive index is, as described in equation 2.2, the square root of the permittivity and will react in the same manner as the permittivity in terms of the changing parameters described above. One can replace the dielectric constant with the refractive index in equation 2.22,

which in fact gives the Lorentz-Lorenz relation discovered separately at almost the same time as the Clausius-Mossotti relation.[17]

The polarization per unit volume is given as $\mathbf{P} = N\alpha\mathbf{E}$. In combination with equation 2.8 this expresses the molecular polarizability as a function of angular frequency:

$$N\alpha(\omega) = N \cdot \frac{e^2}{m(\omega_0^2 - \omega^2 - i\omega\gamma)}. \tag{2.25}$$

By combining equations 2.24 and 2.25 we get an expression for the permittivity or refractive index based on temperature, pressure and frequency:

$$\frac{\epsilon - 1}{\epsilon + 2} = \frac{1}{3\epsilon_0}\frac{P_r N_A}{RT}\sum_i \frac{N_i e^2}{m(\omega_i^2 - \omega^2 - i\omega\gamma)}) \tag{2.26}$$

or

$$\frac{n^2 - 1}{n^2 + 2} = \frac{1}{3\epsilon_0}\frac{P_r N_A}{RT}\sum_i (\frac{N_i e^2}{m(\omega_i^2 - \omega^2 - i\omega\gamma)}) \tag{2.27}$$

where ω_j is the resonance frequency of the ith component.

2.1.4 Sellmeier equation

The derivation made in the previous chapter is often represented in a different way, called the Sellmeier equation. This equation gives the refractive index as a function of frequency, but does not take the Lorentz local field into account. Even if its lacking physical accuracy, it has found widespread use as a way to express the refractive index of optical materials. To derive it we start by combining equations 2.11 and 2.19 giving an expression for the permittivity.

$$\epsilon = 1 + \frac{\mathbf{P}}{\mathbf{E}\epsilon_0}.$$

If we then combine the result with that of equation 2.8 we get

$$\epsilon - 1 = \frac{Ne^2}{m\epsilon_0(\omega_0^2 - \omega^2 - i\omega\gamma)},$$

which also can be written in terms of the refractive index as

$$n^2 - 1 = \frac{Ne^2}{m\epsilon_0(\omega_0^2 - \omega^2 - i\omega\gamma)}.$$

If we assume that the operating frequency ω is far away from the resonance frequency, the effect of the damping γ can be neglected and γ equals zero. By converting the angular frequency to wavelength by the relation $\omega = {}^{2\pi c}/_{\lambda}$ we get

$$n^2 - 1 = \frac{\frac{Ne^2}{m\epsilon_0}\lambda_0^2\lambda^2}{(2\pi c)^2(\lambda^2 - \lambda_0^2)} = \frac{B\lambda^2}{\lambda^2 - C}, \tag{2.28}$$

where $B = \frac{Ne^2\lambda_0^2}{(2\pi c)^2 m\epsilon_0}$ is the resonance strength and $C = \lambda_0^2$ is the resonance wavelength. For solid materials, B and C must be found empirically as they are depending on the Lorentz local field as well as the external field. Up until now it has been assumed that the electric field acting on the molecule in question only affects the vibration of the electrons, as described in section 2.1.1. Depending on the substance, other modes of vibration may also be excited by an incident light beam. This means that equation 2.28 must be expanded to include all relevant vibrational modes. [20, 21]

$$n^2 - 1 = \sum_i \frac{B_i\lambda^2}{\lambda^2 - C_i}. \tag{2.29}$$

This is the Sellmeier Equation with Sellmeier constants B_i and C_i. The sum is often reduced to either two or three terms in the visible frequency range, as this proves to be sufficient to describe the refractive index accurately. The Sellmeier equation can describe the refractive index of all kinds of substances, as long as they have clearly defined resonance peaks.

2.1.5 Reflection and refraction

When a light beam is incident on an interface between two isotropic substances of different refractive index, a portion of the energy will pass through the surface and the rest will be reflected back. Based on the angle of incidence and the refractive indices of the substances either side of the interface, the angle of the refracted beam will change. This is known as refraction.[22] To physically explain this phenomenon we start by expressing the electric field of the light beam as given by solving the electrical wave equation:

$$\mathbf{E}(\mathbf{r}, t) = \mathbf{E}_0 e^{i(\mathbf{k}\cdot\mathbf{r} - \omega t)}. \tag{2.30}$$

The notation is on complex form, but the electric field will always be the real part of this vector. We can decompose the electric field into two components to account for polarization of the wave. This wave polarization should not be confused with the polarization of molecules mentioned in the previous chapters. The transverse nature of the electromagnetic wave, meaning that the oscillations of the wave are perpendicular to the propagation direction, gives rise to the property of polarization. If we consider the electric component of the wave, the two-dimensional plane in which the field oscillates can be fixed in a single direction or it can change over time. If we consider a wave propagating along the z-axis we can express the electrical field in terms of an x and a y component as [22]:

$$\mathbf{E}_0 = E_{0,x} + E_{0,y}, \tag{2.31}$$

where $E_{0,x}$ and $E_{0,y}$ are complex amplitudes. If the phase information in the two components are equal, the orientation of oscillation will be fixed, referred to as linear polarization. But if the phase information is different, the resulting oscillation direction will change over time. The result is that the plane of oscillation will rotate in an elliptical manner, known as elliptical polarization. If the phase difference between the two components are $\pi/2$ the special case of circular polarization occurs.

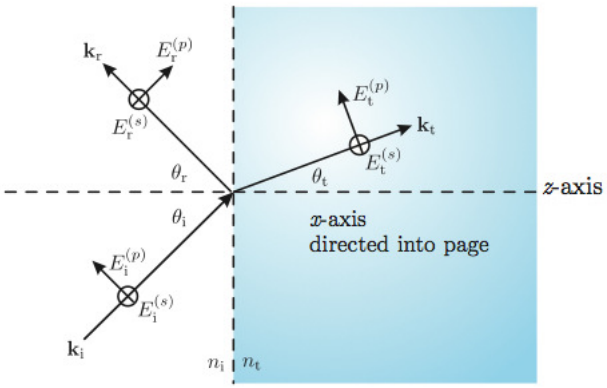

Figure 2.5: Incident wave E_i, reflected wave E_r and transmitted wave E_t at an interface between two substances of different refractive index. [22]

To explain the concept of refraction we want to explain the dependency of the transmitted angle θ_t to the incident angle θ_i and the refractive indices n_i and n_t of the two substances as figure 2.5 depicts. We have an incident wave $\mathbf{E}_i$, a reflected wave $\mathbf{E}_r$ and a transmitted wave $\mathbf{E}_t$ each propagating in directions given by $\mathbf{k}_i$, $\mathbf{k}_r$ and $\mathbf{k}_t$. If the y-z plane is the plane of incidence, as shown on the figure, and the x-axis has a positive direction into the paper, we can decompose the wave

number vectors in y and z components, where $\mathbf{x}$, $\mathbf{y}$ and $\mathbf{z}$ are unit vectors for each direction:

$$\begin{aligned}\mathbf{k}_i &= k_i(\mathbf{y}\cdot sin\,\theta_i + \mathbf{z}\cdot cos\,\theta_i)\\ \mathbf{k}_r &= k_r(\mathbf{y}\cdot sin\,\theta_r - \mathbf{z}\cdot cos\,\theta_r)\\ \mathbf{k}_t &= k_t(\mathbf{y}\cdot sin\,\theta_t + \mathbf{z}\cdot cos\,\theta_t)\end{aligned} \tag{2.32}$$

Each wave on the form given in 2.30 can be decomposed into two components as done in equation 2.31, but with new descriptive letters. The direction represented by a circled x represents the direction into the paper, perpendicular to the plane of incidence, and is denoted $E^{(s)}$. The direction parallel to the plane of incidence is denoted $E^{(p)}$.

$$\begin{aligned}\mathbf{E}_i &= (E_i^{(p)}(\mathbf{y}\cdot cos\,\theta_i - \mathbf{z}\cdot sin\,\theta_i) + E_i^{(s)}\cdot\mathbf{x})e^{i(k_i(y\cdot sin\,\theta_i + z\cdot cos\,\theta_i)-\omega_i t)}\\ \mathbf{E}_r &= (E_r^{(p)}(\mathbf{y}\cdot cos\,\theta_r + \mathbf{z}\cdot sin\,\theta_r) + E_r^{(s)}\cdot\mathbf{x})e^{i(k_r(y\cdot sin\,\theta_r - z\cdot cos\,\theta_r)-\omega_r t)}\\ \mathbf{E}_t &= (E_t^{(p)}(\mathbf{y}\cdot cos\,\theta_t - \mathbf{z}\cdot sin\,\theta_t) + E_t^{(s)}\cdot\mathbf{x})e^{i(k_t(y\cdot sin\,\theta_t + z\cdot cos\,\theta_t)-\omega_t t)}\end{aligned} \tag{2.33}$$

With the description of the electric fields in place, the next step is to apply a boundary condition at the interface. It can be shown by the use of Faradays law that the electric fields parallel to an interface must be equal on both sides of the interface. This means that at the interface a $z = 0$, the fields in the x and y-direction must be equal on both sides [22]:

$$\begin{aligned}&(E_i^{(p)}(\mathbf{y}\cdot cos\,\theta_i) + E_i^{(s)}\cdot\mathbf{x})e^{i(k_i y\cdot sin\,\theta_i-\omega_i t)} + (E_r^{(p)}(\mathbf{y}\cdot cos\,\theta_r) + E_r^{(s)}\cdot\mathbf{x})e^{i(k_r y\cdot sin\,\theta_r-\omega_r t)}\\ &\qquad = (E_t^{(p)}(\mathbf{y}\cdot cos\,\theta_t) + E_t^{(s)}\cdot\mathbf{x})e^{i(k_t y\cdot sin\,\theta_t-\omega_t t)}.\end{aligned} \tag{2.34}$$

If this equation should be valid for all values of y and t, all the exponential factors must be equal:

$$k_i y\cdot sin\,\theta_i - \omega_i t = k_r y\cdot sin\,\theta_r - \omega_r t = k_t y\cdot sin\,\theta_t - \omega_t t.$$

This requires the angular frequency components ω of the waves to be equal:

$$k_i\cdot sin\,\theta_i = k_r\cdot sin\,\theta_r = k_t\cdot sin\,\theta_t.$$

We also know that the wave number $k = \omega/v_p$ where v_p is the phase speed in the medium and we have the definition of refractive index as $n = c/v_p$, which gives:

$$k = \frac{\omega\cdot n}{c}. \tag{2.35}$$

As both k_i and k_r are propagating in the same medium with the same refractive index, the values vil be the same. This gives the relationship between the incident

and the reflected angle:

$$\theta_i = \theta_r.$$

The relationship between the incident and the transmitted angle will be

$$n_i sin(\theta_i) = n_t sin(\theta_t), \tag{2.36}$$

which is known as Snells law and describes the concept of refraction. We can also express the value of the electric field as a function of the incident and reflected angles. Since the exponential factors of equation 2.34 are equal we can simplify the analysis and divide it into one equation for each direction x and y:

$$\begin{aligned} x - direction: \ E_i^{(s)} + E_r^{(s)} &= E_t^{(s)} \\ y - direction: \ (E_i^{(p)} + E_r^{(p)})cos\,\theta_i &= E_t^{(p)} cos\,\theta_t \end{aligned} \tag{2.37}$$

To get expression for the electric field on both sides of the interface we must use a second boundary criteria, which states that the magnetic fields parallel to the interface must be equal on both sides of the interface. To relate the electric and magnetic field we use Faradays law from equation 2.4 which states that the magnetic field can be written as [22]:

$$\mathbf{B} = \frac{\mathbf{k} \times \mathbf{E}}{i\omega} = \frac{n}{c}\mathbf{u} \times \mathbf{E},$$

where $\mathbf{u}$ is a unit vector pointing in the same direction as the $\mathbf{k}$-vector. We can now make expressions for the magnetic fields based on the equations in 2.33, where the orientation of the fields have changed according to the cross product

$$\begin{aligned} \mathbf{B}_i &= \tfrac{n_i}{c}\left[(-E_i^{(p)} \cdot \mathbf{x} + E_i^{(s)}(\mathbf{y}{\cdot}cos\,\theta_i - \mathbf{z} \cdot sin\,\theta_i))e^{i(k_i(y \cdot sin\,\theta_i + z \cdot cos\,\theta_i) - \omega_i t)}\right] \\ \mathbf{B}_r &= \tfrac{n_i}{c}\left[(E_r^{(p)} \cdot \mathbf{x} + E_r^{(s)}(-\mathbf{y}{\cdot}cos\,\theta_r - \mathbf{z} \cdot sin\,\theta_r))e^{i(k_r(y \cdot sin\,\theta_r - z \cdot cos\,\theta_r) - \omega_r t)}\right] \\ \mathbf{B}_t &= \tfrac{n_t}{c}\left[(-E_t^{(p)} \cdot \mathbf{x} + E_t^{(s)}(\mathbf{y}{\cdot}cos\,\theta_t - \mathbf{z} \cdot sin\,\theta_t))e^{i(k_t(y \cdot sin\,\theta_t + z \cdot cos\,\theta_t) - \omega_t t)}\right] \end{aligned} \tag{2.38}$$

By applying the boundary condition, demanding that the magnetic fields parallel to the interface are equal on both sides of the boundary, and the fact that the different exponential factors as well as the incident and reflected angles are equal we get a new equation for $z = 0$:

$$n_i\left[-E_i^{(p)} \cdot \mathbf{x} + E_i^{(s)}\mathbf{y}{\cdot}cos\,\theta_i\right] + n_i\left[E_r^{(p)} \cdot \mathbf{x} - E_r^{(s)}\mathbf{y}{\cdot}cos\,\theta_i\right] = n_t\left[-E_t^{(p)} \cdot \mathbf{x} + E_t^{(s)}\mathbf{y} \cdot cos\,\theta_t\right].$$

This can a be simplified in a similar manner as done in equation 2.37 giving:

$$\begin{aligned} x-direction:\ n_i(E_i^{(p)} - E_r^{(p)}) &= n_t E_t^{(p)} \\ y-direction:\ n_i(E_i^{(s)} - E_r^{(s)})cos\,\theta_i &= n_t E_t^{(s)} cos\,\theta_t \end{aligned} \tag{2.39}$$

These equations in combination with the equations in 2.37 gives a complete description of the electric fields on both sides of the interface. We can express these relationships even simpler by construction coefficients relating the reflected and transmitted field to the incident field. By first examining the perpendicular component $E^{(s)}$ of the electric field, we know from equations 2.37 and 2.39 that:

$$\begin{aligned} E_i^{(s)} + E_r^{(s)} &= E_t^{(s)} \\ n_i(E_i^{(s)} - E_r^{(s)})cos\,\theta_i &= n_t E_t^{(s)} cos\,\theta_t \end{aligned}$$

By applying Snells law from equation 2.36 and the rearranging the expressions we arrive at equations for $\frac{E_t^{(s)}}{E_i^{(s)}}$ and $\frac{E_r^{(s)}}{E_i^{(s)}}$.

$$\begin{aligned} t_s \equiv \frac{E_t^{(s)}}{E_i^{(s)}} &= \frac{2sin\,\theta_t\,cos\,\theta_i}{sin\,\theta_t\,cos\,\theta_i + sin\,\theta_i\,cos\,\theta_t} \\ r_s \equiv \frac{E_r^{(s)}}{E_i^{(s)}} &= \frac{sin\,\theta_t\,cos\,\theta_i - sin\,\theta_i\,cos\,\theta_t}{sin\,\theta_t\,cos\,\theta_i + sin\,\theta_i\,cos\,\theta_t} \end{aligned} \tag{2.40}$$

By doing the same thing for the parallel component $E^{(p)}$, we get a similar set of equations:

$$\begin{aligned} t_p \equiv \frac{E_t^{(p)}}{E_i^{(p)}} &= \frac{2sin\,\theta_t\,cos\,\theta_i}{sin\,\theta_i\,cos\,\theta_i + sin\,\theta_t\,cos\,\theta_t} \\ r_p \equiv \frac{E_r^{(p)}}{E_i^{(p)}} &= \frac{sin\,\theta_t\,cos\,\theta_t - sin\,\theta_i\,cos\,\theta_i}{sin\,\theta_i\,cos\,\theta_i + sin\,\theta_t\,cos\,\theta_t} \end{aligned} \tag{2.41}$$

We have now defined a set of coefficients describing the electrical field on the two sides of the interface. These coefficients are know as Fresnel coefficients and will be used to derive expressions for fractions of light intensity being transmitted and reflected in the next section.

2.1.6 Reflectance and transmittance

As explained in the last section, the phenomenon of refraction causes a light ray of oblique incidence on an interface between two substances of different refractive index to be transmitted with a different angle than that of the incident beam. It was also explained that a portion of of the light was reflected back with an angle equal to that of the incident angle. The last section concluded with a set of equations describing the electric field on both sides of the interface. These

last equations will be used in this section, where the concept of reflectance and transmittance will be explained. Reflectance describes the fraction of the incident intensity which will be reflected at the interface, whereas the transmittance gives the fraction being transmitted.[22] The relationship between intensity I and the electric field E in plane wave is given as

$$I = \frac{c\epsilon_0 n}{2} |E|^2 , \tag{2.42}$$

where the intensity is the power per unit area. The intensity of the incident wave can be expressed as a sum of the intensities of the two polarization components since they are orthogonal:

$$I_i^{tot} = I_i^{(p)} + I_i^{(s)} = \frac{c\epsilon_0 n}{2}(\left|E_i^{(p)}\right|^2 + \left|E_i^{(s)}\right|^2).$$

As the reflected wave is propagating in the same medium as the incident wave, and therefore experiences the same refractive index, the reflected intensity can then be expressed as

$$I_r^{tot} = I_r^{(p)} + I_r^{(s)} = I_i^{(p)} \cdot |r_p|^2 + I_i^{(s)} \cdot |r_s|^2 , \tag{2.43}$$

where the squared Fresnel coefficients from equations 2.40 and 2.41 are used to express the reflected intensity as a function of the incident intensity. The intensity of the transmitted wave cannot be expressed in the same way because of the difference in refractive index in the two substances. To work around this problem, we alter equation 2.43 to express the power in place of the intensity [22]:

$$P_r^{tot} = P_r^{(p)} + P_r^{(s)} = P_i^{(p)} \cdot R_p + P_i^{(s)} \cdot R_s, \tag{2.44}$$

where $R_p = |r_p|^2$ and $R_s = |r_s|^2$ are the reflectance coefficients. The law of conservation of energy states that the energy of a closed system will be preserved. That means that we can express an energy balance at the interface

$$P_i^{tot} = P_t^{tot} + P_r^{tot},$$

and by inserting it into equation 2.44 we get an expression for the transmitted power

$$P_t^{tot} = P_i^{(p)} \cdot (1 - R_p) + P_i^{(s)} \cdot (1 - R_s),$$

where $(1 - R_P) \equiv T_p$ and $(1 - R_s) \equiv T_s$ are the transmittance coefficients. We can now express the transmitted intensity as a function of the incident intensity

and the transmittance coefficients:

$$I_t^{tot} = I_i^{(p)} T_p + I_i^{(s)} T_s.$$

Figure 2.6 shows an example of the relationship between the transmittance and reflectance coefficients and the incident angle and the refractive indices on both sides of the interface. The refractive indices used in the figure are taken from a specific prism-water interface in the instrument which was constructed for the thesis.

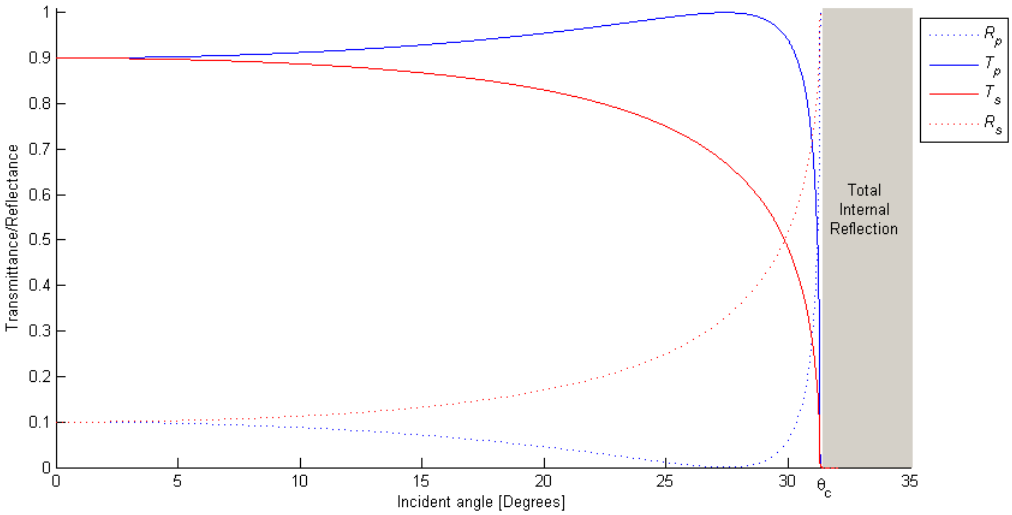

Figure 2.6: Transmittance and reflectance as a function of the incident angle on a prism water interface where $n_i = 2.58$ and $n_t = 1.33$.

Total internal reflection To conclude this section, two special cases involving refraction will be discussed. The first case involves an investigation of Snells law. If we express the transmitted angle as a function of the the refractive indices and the incident angle

$$\theta_t = sin^{-1}(\frac{n_i}{n_t} sin\,\theta_i),$$

we see that if $n_i > n_t$ there exists an incident angle θ_i resulting in the argument of the inverse sinus function being 1, giving a transmitted angle of 90^o. This angle is referred to as the critical angle θ_c. By inserting the transmitted angle of 90^o into the expressions for r_p and r_s from equations 2.40 and 2.41, we get reflectance coefficients $R_p = R_s = 1$. This is called total internal reflection. Figure 2.7 presents an example on this phenomenon. The figure describes a specific prism-water interface in the instrument which was constructed for the thesis.

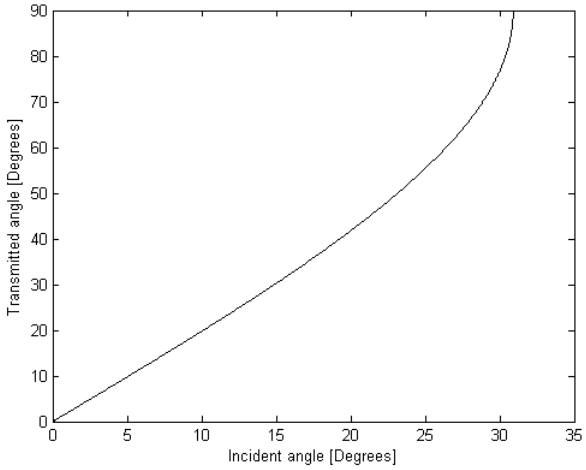

Figure 2.7: The transmitted angle as a function of the incident angle on a prism-water interface where $n_i = 2.58$ and $n_t = 1.33$.

Evanescent waves The second special case describes evanescent waves. When the incident angle exceeds the critical angle, causing total internal reflection, we also get a wave traveling parallel to the plane of incidence on the opposite side of the boundary. To derive its properties we start by modifying Snells law from equation 2.36 by using the relation $sin^2\phi + cos^2\phi = 1$ and get [22]:

$$cos\,\theta_t = i\sqrt{\frac{n_i^2}{n_t^2}sin^2\theta_i - 1} \quad (\theta_i > \theta_c). \tag{2.45}$$

If we input this into the expression for the electric field of the transmitted wave $\mathbf{E}_t$ from equation 2.30 we get:

$$\mathbf{E}_t = \left[E_t^{(p)}(\mathbf{y}\cdot i\sqrt{\frac{n_i^2}{n_t^2}sin^2\theta_i - 1} - \mathbf{z}\cdot\frac{n_i}{n_t}sin\,\theta_i) + E_t^{(s)}\cdot\mathbf{x}\right] \tag{2.46}$$
$$\cdot\, e^{-k_t z\cdot\sqrt{\frac{n_i^2}{n_t^2}sin^2\theta_i - 1}}\, e^{i(k_t y\cdot\frac{n_i}{n_t}sin\,\theta_i - \omega_t t)}$$

We see from the expression that we have an electric field on the transmitted side of the boundary. From the exponential function describing the z-direction we see that the it no longer describes a standard wave, but instead a exponentially decaying wave along the z-axis. From the last exponential we can see that the wave is propagating along the y-axis, parallel to the plane of incidence. We also see that the wavenumber k_t is modified by a factor of $\frac{n_i}{n_t}sin\,\theta_i$. This means that the wavenumber of the evanescent wave will change as the incident angle is

changed in the region $\theta_c < \theta_i < 90^o$.

2.2 Light sensing semiconductors

The operating principle of a light sensing semiconductor is that incident photons of wavelength λ and energy $E = {}^{hc}/_{\lambda}$, where $h = 6.63 \cdot 10^{-34J}/_{s}$ is Planck's constant, excites the atoms of a semiconductor. This semiconductor material has a given energy gap E_G between the valence band, in which the electrons are tied to their atoms, and the conduction band, where the electrons are free and will contribute to the conductivity of the semiconductor. If the energy of the photons match the energy gap of the semiconductor, the photons will excite electrons from the valence band to the conduction band, leaving behind a vacant space in the valence band known as a hole. Light of a certain range of wavelengths, with a peak at $\lambda_0 = {}^{hc}/_{E_G}$, will create electron-hole pairs known as charge carrier pairs, in a material with a given E_G. As the light intensity increases, the conductivity of the semiconductor will increase as well. [16]

2.2.1 P-n junction

A pure semiconductor is referred to as an intrinsic material or i-type material. It has a temperature dependent gap between the valence band and conduction band. The size of the band gap is low compared to an insulator and is in the region of 0.5 to $3.5\,eV$. One of the most common semiconductor materials is Silicon with a band gap energy of $1.11\,eV$ at $302K$. This corresponds to a peak wavelength of $\lambda_0 = {}^{hc}/_{1.11eV} = 1.12\mu m$. A conductor has little or no gap between these bands, whereas insulators have a large gap. By using a p-n junction instead of a pure semiconductor material we can control the properties of the diode and especially expand the range of wavelengths that can be detected. A p-n junction is a semiconductor device consisting of a p-type and an n-type semiconductor material joined at a junction. P-type and n-type refers to semiconductor materials with deliberately added impurities, known as doping.

A n-type material is a semiconductor material doped with a number of atoms containing a higher number of protons and electrons than that of the semiconductor material. The added impurities will create covalent bonds with the existing structure of semiconductor atoms, but since there are too many electrons compared to what is needed in the given structure, the extra electrons will be

bound very loosely to the mother atom. The added impurity acts as a donor of electrons.[16, 23]

A p-type material adds impurities in the form of atoms containing less protons and electrons than the semiconductor material in which it is added. This leads to a lack of electrons to completely tie the added impurity to the structure with covalent bonds. This lacking electron or "hole" can move through the material and act as a charge carrier. As the added impurity is one electron short, compared to the semiconductor atoms, it is called an acceptor as it accepts other electrons. In both p-type and n-type materials it is the generated charge carriers that actually move through the material, not the introduced atoms themselves.

By joining the two materials at an interface, we get a p-n junction. As long as no voltage is applied, the area near the junction will reach a state of equilibrium as the extra electrons from the n-type material on and near the junction bonds with the holes on and near the junction of the p-type material. The region in which both p-type and n-type charge carriers are bonding is called the depletion zone, as no charge carriers exist in this region. It also means that an electric field is created, pointing from the n-side to the p-side. If a photon is incident on the depletion region or close by it, the excited electron will be immediately affected by the electric field. The electron will move towards the n-type layer or cathode and the hole left behind will move towards the p-type layer or anode. By applying a potential to the n-type layer and a positive potential to the p-type layer, called a reverse-biased voltage, the voltage across the junction and the size of the depletion zone increases. As the area of the depletion zone increases, it will detect light more effectively. [16, 23]

2.2.2 Photodiode operation

The photodiode can operate in two different modes. The photovoltaic mode is when the photodiode is connected to an external circuit consisting of a resistor. When incident light produces charge carriers in the p-n junction, the current through the circuit is increased and consequently the voltage over the resistor increases while the voltage across the p-n junction remains constant. The ratio between the number of generated charge carrier pairs N_e versus number of photons incident on the semiconductor N_ν is referred to as quantum efficiency η and measured in percent:

$$\eta = \frac{N_e}{N_\nu}.$$

This relationship is dependent on the wavelength of the photons as described earlier in this section. It can also be expressed as the ratio between the photo voltage produced by a given incident power with the unit $^{V}/_{W}$. Then it is referred to as responsivity or spectral responsivity if expressed as a function of the wavelength. The current produced will be proportional to the incident power of the light beam. At the peak wavelength corresponding to the exact band gap energy, η could be as high as $80 - 90\%$ in a photodiode. There are three primary effects reducing the quantum efficiency of the photodiode. One effect is that some of the incident light will hit the detector outside the depletion region. If this happens the excited electron will recombine with the hole because there is no electric field to move the electron in this region. Some of the incident light will also be reflected in the semiconductor surface resulting in a reduced quantum efficiency. Lastly, not all of the incident light will be absorbed in the semiconductor material. A material with a given absorption coefficient needs a certain depth to make sure that all the light is absorbed in the material. If the material is to thin in relation to the given absorption coefficient, a portion of the incident light will pass through the detector, resulting in reduced quantum efficiency.[23]

The photoconductive mode requires the p-n junction to be reverse biased. The operating principle is the same as the photovoltaic mode, but the diode is connected in a circuit and we measure the photocurrent instead of the voltage. This also requires the definition of responsivity to be the ratio of the produced photocurrent to the incident power with the unit $^{A}/_{W}$. The reverse voltage makes the depletion region larger, making the probability of photon-electron interaction larger. The larger electric field also contributes to accelerate the electrons more and the response time of the circuit will be lowered with a higher reverse bias voltage. [23]

To quantify the generated photocurrent i_p we define the number of photons that interface with the semiconductor per unit time as photon flux Φ_p. A given photon flux would produce an electron flux $\Phi_e = \eta\Phi_p$. This means that the photocurrent will be $i_p = \eta e\Phi_p$ where e is the electron charge. If we relate the photon flux to optical power we get that $P_o = hf\Phi_p$.[23] This gives an expression for the photocurrent produced as a function of both incident power and frequency:

$$i_p = \frac{\eta e P_o}{hf}. \tag{2.47}$$

For a given frequency we can define a responsivity $S = {}^{\eta e}/_{hf}$ giving a simplified

expression for the generated photocurrent as:

$$i_p = S \cdot P_o. \tag{2.48}$$

2.3 Measurement of refractive index

There exists several methods of measuring the refractive index of a medium. This section will give a brief background of how some of the different methods work. The refractometric method will be described thoroughly, while the other methods will be briefly discussed. The focus of the section will be to highlight the benefits and disadvantages of the available methods when it is assumed to be used in a sensor platform deployed in the ocean. The setting is that the sensor is placed on a measuring pod autonomously in the ocean for several days/weeks without the possibility of any maintenance. Two reference criteria have been chosen to evaluate and compare the different methods:

1. The ratio of sensitivity to change in the refractive index to the size of the instrument is important. As the sensor is to operate from either a measurement pod or other underwater crafts such as floats, gliders or unmanned submarines, the degree of miniaturization is of major importance.

2. The degree of immunity to the basic environmental factors such as temperature and pressure must be considered. The construction of rugged subsea equipment will not be discussed, neither will models describing the structural integrity of the instrument as functions of environmental effects be presented, but a qualitative perspective of the effects will be given.

2.3.1 Refractometric methods

The concept on which the design in this project is based, is a refractometric setup often referred to as a Pulfrich refractometer.[24] Figure 2.8 shows a schematic overview of the Pulfrich refractometer. The laser beam hits the air-prism interface perpendicularly and continues without refraction to the prism-sample interface. Here the laser beam makes an incident angle with the interface and based on the refractive index of both the prism and the sample, the refracted angle is different from the incident angle, as Snell´s law describes. If the refractive index of the sample is grater than that of the prism, the refracted angle will be less than

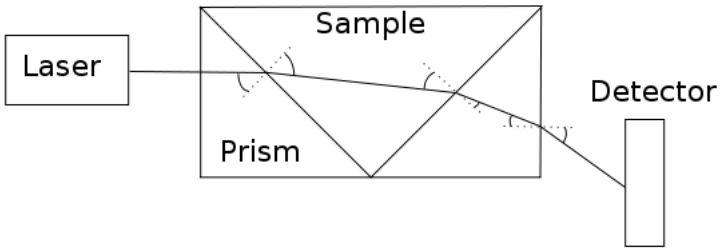

Figure 2.8: Schematic overview of a Pulfrich refractometer. [24]

the incident angle, and vice versa. The laser beam then propagates through the sample and hits the sample-prism interface, with the same phenomenon taking place. The beam is then refracted one last time in the prism-air interface before it hits the detector. The detector measures the lateral displacement of the laser beam, and based on a geometrical expression derived from the refractometric setup, one can derive the refractive index of the sample. We can simplify figure 2.8 by only looking at one prism-water interface, as done in figure 2.9, we can easily show the theoretical minimum detectable change in refractive index. The transmitted angle θ_t from the prism-water interface can be expressed through Snell's Law by the following equation:

$$\theta_t = arcsin(sin(\theta_i) \cdot \frac{n_{prism}}{n_{sample}}), \tag{2.49}$$

where θ_i is the incident angle on the prism-water interface, n_{prism} is the refractive index of the prism and n_{sample} is the refractive index of the water sample.

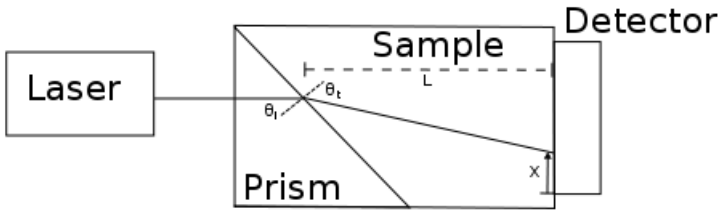

Figure 2.9: Simplified refractometric setup

If we express a small change of the transmitted angle as a function of a small change of the refractive index of the water sample we get the following expression through differentiation:

$$\frac{\delta\theta_t}{\delta n_{sample}} = \frac{\delta}{\delta n_{sample}}(arcsin(sin(\theta_i) \cdot \frac{n_{prism}}{n_{sample}})) = -\frac{sin(\theta_i) \cdot n_{prism}}{n_{sample}^2\sqrt{1 - (\frac{n_{prism}sin(i)}{n_{sample}})^2}}. \tag{2.50}$$

We can express a small change of laser position displacement at the sensor, δX, in terms of a small change of transmitted angle $\delta\theta_t$ and the length between the prism-water interface and the detector, L:

$$\delta X \approx \delta\theta_t \cdot L. \tag{2.51}$$

If we then rearrange equation 2.50 we get an expression for the minimum detectable change of refractive index of the water sample.

$$\delta n_{sample} = \frac{\delta X \cdot n_{sample}^2}{n_{prism} sin(\theta_i) \cdot L} \cdot \sqrt{1 - (\frac{n_{prism} sin(\theta_i)}{n_{sample}})^2}.$$

The value of δX is given as the minimum detectable displacement of the sensor. We see that a larger path length L and a lower minimum detectable displacement δX will result in a lower δn_{sample} and hence better resolution in the salinity measurement. If we define the variables in the equation with sensible values as $L = 10\,cm$, $\delta X = 0.3\,\mu m$, $\theta_i = 60^o$, $n_{prism} = 1.5$ and $n_{sample} = 1.33$, we get a theoretical sensitivity in refractive index measurements of magnitude 10^{-7}.

As one can observe in figure 2.8 and 2.9, the lateral displacement is dependent on the path length of the laser beam, from the point of its first refraction and all the way to the sensor, as well as the refracted angles. That means that a small change in the refractive index of the sample, resulting in a small change in the refracted angle, will give a small lateral displacement if the path length of the laser beam is small. If the path length increases, so does the lateral displacement. This is of major importance to the construction of refractometric measurement systems. It is in principle possible to create a measurement system capable of measuring salinity very accurately, assuming the path length is long. The deciding factor is the minimum detectable displacement of the detector. Recent advances in detector technology, resulting in micron scale minimum detectable displacement has paved the way for construction of compact refractometers with very good resolution.[6, 25]

To evaluate the criteria of miniaturization in a refractometer on must take into account the resolution of the detector. A displacement detector with very high spatial resolution will allow for construction of refractometers with small path lengths. Given the spatial resolution of commercially available detectors, the path length still is in the region of 10 cm.[6] As the laser and detector also requires space, the overall size of the sensor will exceed this length.

The effect of temperature and pressure will affect the structural integrity of the sensor cabinet. This will cause degradation of the measurement accuracy as the optical path will be slightly modified. Modeling of the environmental effects on the cabinet will to some extent reduce the impact of this effect.

2.3.2 Interferometric methods

The concept of interferometry is based on the superposition of two light waves, creating a measurable interference pattern. By combining two waves of the exact same wavelength, referred to as a coherent process, one can extract information about the phase difference of the waves by observing the interference pattern. In practical application one uses a laser which is split into two rays by a beam splitter. The two rays then travel down separate paths and is then merged before hitting a detector or a screen. If the two paths are identical in terms of length and light propagation speed, the result will be constructive interference as phase difference is zero. If either the length or light propagation speed is lower in one of the paths, the result will differ from the constructive interference pattern. If the difference in path length is a whole number of wavelengths of the light, the result is constructive interference. If the path difference is a half number of wavelengths, the result is destructive interference. [16]

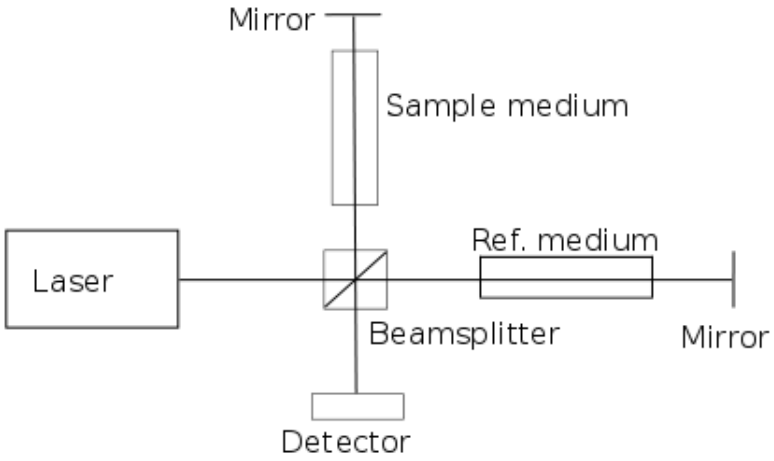

Figure 2.10: Schematic overview of a Michelson Interferometer

As equation 2.1 shows, the refractive index is given by the phase speed of light through a medium. If one of the paths were to pass through a seawater sample with an unknown refractive index, while the other passes through a reference medium with a known refractive index, we detect the difference in refractive index between two media, and are thereby able to detect changes in the unknown refractive index. Figure 2.10 shows one implementation of this principle known

as a Michelson interferometer. The light is split into two waves. One is passing through a reference medium of known refractive index and the other is passing through the sample medium. Both waves are reflected in a mirror and returns to the beamsplitter where they are merged into one beam directed downward to the detector. We can express the electric part off the electromagnetic wave as done in equation 2.30 to describe each wave:

$$\mathbf{E}_{ref} = \mathbf{E}_0 e^{i(\mathbf{k}_{ref}\cdot\mathbf{r}-\omega t)} \text{ and}$$
$$\mathbf{E}_{sample} = \mathbf{E}_0 e^{i(\mathbf{k}_{sample}\cdot\mathbf{r}-\omega t)},$$

where k_{ref} is the wave number for the reference medium, k_{sample} is the wavenumber for the sample under test and r is the distance through the medium, assumed to be equal for the reference and sample medium. We then express the electric field at the detector as a superposition of the real part of both waves. We get the real part from multiplying the electric field with its complex conjugate and divide by two. Since the detector is sensitive to the intensity we see from equation 2.42 that the total intensity will be:

$$\mathbf{I}_{tot} = \frac{nc\epsilon_0}{2} |\mathbf{E}_{ref} + \mathbf{E}_{sample}| \cdot |\mathbf{E}_{ref} + \mathbf{E}_{sample}|^* \tag{2.52}$$

$$\mathbf{I}_{tot} = \frac{nc\epsilon_0}{2}\mathbf{E}_0 \cdot \mathbf{E}_0^*(2 + e^{i((\mathbf{k}_{ref}-\mathbf{k}_{sample})\cdot\mathbf{r})} + e^{-i((\mathbf{k}_{ref}-\mathbf{k}_{sample})\cdot\mathbf{r})})$$
$$\mathbf{I}_{tot} = nc\epsilon_0\mathbf{E}_0 \cdot \mathbf{E}_0^*(1 + cos[(\mathbf{k}_{ref} - \mathbf{k}_{sample}) \cdot \mathbf{r}]).$$

If $\Delta\mathbf{k} \cdot \mathbf{r} = (\mathbf{k}_{ref} - \mathbf{k}_{sample})\mathbf{r} = 2m\pi$ where $m = 0, 1, 2..$ denotes the order of interference maxima, the cosine term equals one and we have constructive interference at the detector. If the difference between the refractive indices of the medium and reference is increased in the region $0 < \Delta k < \pi$, the intensity will decline. When $\Delta k \cdot r = \pi$, the cosine term equals zero and we have destructive interference. We know that $k = {}^{2\pi n}/_{\lambda}$, which gives

$$\mathbf{I}_{tot} = nc\epsilon_0\mathbf{E}_0 \cdot \mathbf{E}_0^*(1 + cos\,\Delta\phi), \tag{2.53}$$

where $\Delta\phi = (n_{ref} - n_{sample})\frac{2\pi r}{\lambda}$. If the sample has the same refractive index as the reference medium, the phase difference will be zero. As this method is differential and the results are repeating themselves for every 2π phase transition, it is necessary to make a continuos measurement as the sample medium is injected into the sample cell. If not, it is impossible to extract an unambiguous result. By following ref, [26] we can evaluate the instruments sensitivity to change in refractive index and see how a small change in the detected signal phase difference $\Delta\phi$ corresponds to a small change of refractive index difference $\Delta n = n_{ref} -$

n_{sample}:

$$\frac{\partial n}{\partial \phi} = \frac{\lambda}{2\pi r}.$$

If we input sensible values to the variables in the equation, such as $r = 1\,cm$ and $\lambda = 635\,nm$ we get a value of $\frac{\partial n}{\partial \phi} = 1.0 \cdot 10^{-5}\,{}^{1}/_{rad}$. If we also assume a phase detection resolution of $d\phi = 1^o \approx 0.017\,rad$ we get a minimum detectable change of refractive index $dn = \frac{\partial n}{\partial \phi} \cdot d\phi = 1.7 \cdot 10^{-7}$. [26]

The detection can be done by measuring the intensity of the center fringe, known as homodyne detection.[27] The intensity will be at its highest when the two waves are in phase, and decrease as the phase difference increases. A more refined method of measuring the phase difference is by measuring the electric beat frequency with a lock-in amplifier.[10]

The size criteria favors an interferometric setup. The cell containing the optical components and sample compartments could be made very small as done by [10] or [28]. The other components such as a highly coherent laser diode and detector are also small. The sensitivity to refractive index change can be very good and reported experimental sensitivities are in the region of 10^{-5}. Larger interferometric setups can achieve even better sensitivity, down to 10^{-8}. [25] The interferometric method is considered one of the most precise ways of measuring both refractive index and spatial movement.[29]

Environmental factors such as temperature and pressure will affect the structural integrity of the sensor cabinet, and this will play a major role in an interferometric setup. Spatial displacement of the optical components, even by fractions of the wavelength of the laser light, will severely degrade performance. The use of differential measurement methods and accurate modeling of environmental effects could to some extent compensate for this effect, but all in all this is the biggest limitation for the interferometric setup.[29, 30]

2.3.3 Total internal reflection

The effect of total internal reflection is described in section 2.1.6. When the incident angle of light exceeds the critical angle, dictated by the ratio of the two refractive indices, the transmitted angle is parallel to the interface between the two substances:

$$\theta_t = sin^{-1}(\frac{n_i}{n_t} sin\,\theta_c) = 90^o.$$

By inserting a transmitted angle of 90^o into the Fresnel equations in 2.40 and 2.41 we see that all of the light is reflected. We can also express the critical angle as

$$\theta_c = sin^{-1}(\frac{n_t}{n_i}).$$

If the light source is a collimated laser, this means that no light will pass through

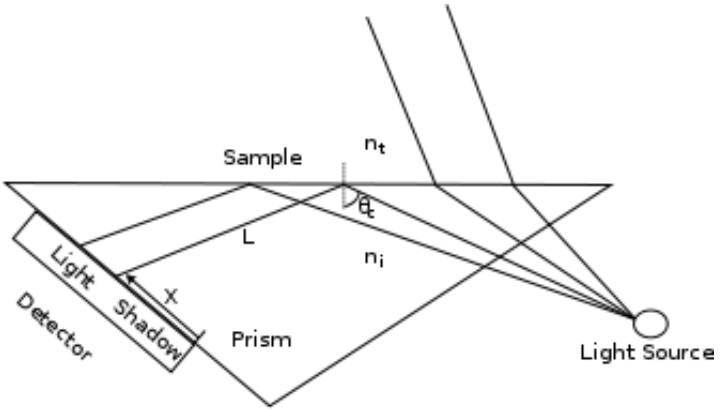

Figure 2.11: Schematic overview of a total internal reflection refractometer

the interface between the two substances. If we use an uncollimated light source instead of a laser we could make use of this effect to measure the refractive index. Figure 2.11 illustrates the concept of such a sensor. The light from the source enters a prism. As the light is unfocused and not in a single beam, we have a continuous light field, illustrated by four beams in the figure. The beams which hit the prism-sample interface at an angle less than that of the critical angle θ_c, will be transmitted through the sample. The beams with incident angles on the prism-sample interface greater than the critical angle will be reflected towards the detector. As illustrated, this will generate a bright and a dark area on the detector, which could be an array of photodiodes or a CCD camera chip. By evaluating the area of the detector where the transition between light and dark occurs, we can determine the critical angle. Due to diffraction from the reflection surface the transition from light to dark is gradual transition. This is further strengthened by the fact that some portion of the light is reflected regardless of the incident angle, and that it increases with increasing incident angle until reaching the maximum of 100% reflection at the critical angle. This means that it could be hard to determine the exact critical angle.

To express this mathematically we define a small change in critical angle as a function of a small change of refractive index in the sample, where it is

implied that the refractive indices in question are positive and $n_i > n_t$, as:

$$\frac{\delta\theta_c}{\delta n_t} = \frac{\delta}{\delta n_t}\left[sin^{-1}(\frac{n_t}{n_i})\right] = \frac{1}{\sqrt{n_i^2 - n_t^2}}.$$

We can then express a small change in the displacement of the light-shadow boundary dX on the sensor as a function of a small change in the critical angle $\delta\theta_c$ as:

$$dX \approx L \cdot \delta\theta_c,$$

where L is the distance from the point of reflection to the sensor, and is assumed, for simplicity in calculations, to be constant. If we the define dX as the sensors inherent minimum detectable displacement, we can express the minimum detectable change of refractive index as:

$$\delta n_t = \frac{dX}{L}\sqrt{n_i^2 - n_t^2},$$

where we see that a larger distance L and a smaller minimum detectable sensor displacement dX will contribute to a lower δn_t and hence a better sensitivity to change in refractive index of the sample. If we define sensible values to the variables, such as $L = 10cm$, $\delta X = 6\mu m$, $n_i = 1.5$ and $n_t = 1.33$ we get a sensitivity in the refractive index of the sample of magnitude 10^{-6}.

Another version of this instrument observes the light transmitted through the sample instead of looking at the reflected light and is called the Abbe refractometer. It was invented by Ernest Abbe in the late 19. century. The version created by Abbe, and still being used today due to its simplicity, did of course not include an electronic sensor. The reading was made by looking at the prism through an eyepiece with markings to determine the refractive index of the sample.

The resolution to size ratio is not as good as the refractometer, being one order of magnitude less. The calculated resolution does not take into account the mentioned difficulties in determining the exact value of the critical angle, which will cause a deterioration of the resolution. The instruments ability to resist environmental factors such as pressure and temperature is most likely very good. It is possible to attach the detector and light source to the prism, which limits the effect of chassis structural changes caused by the environment to a single element, namely the prism. This makes it possible to simulate the effects with a higher degree of certainty than in the other methods mentioned earlier.

2.3.4 Other techniques

There are also other techniques to measure the refractive index of sea water. Without going into specific details, a brief overview of a couple of methods based on published articles will be given. Methods involving the surface plasmon resonance (SPR) effect are used in several articles.[13, 1, 31, 32] A plasma oscillation in a metal is a collective excitation of electrons in a conductor. A given metal has a certain resonance frequency. If the incident photon wavenumber matches the resonance frequency, the photon will transfer some or all of its energy to the oscillation. If the this effect arises on the surface of the metal it is called surface plasmon oscillations. If the surface of the metal interfaces with a dielectric medium, the plasma in the surface area will be a combination of the contribution from the metal and from the dielectric medium. [18]

To couple a light wave to the surface plasmon we can consider the case where light is incident on a prism-water surface with an incident angle greater than the critical angle, which will lead to total internal reflection. Suppose that the surface of the prism in contact with water is coated by a thin layer of metal, and that the evanescent wave described in equation 2.46 is propagating in the metal and slightly into the water parallel to the interface. This evanescent wave will then, if matching the combined resonance frequency of the metal coating and water layer, and fulfilling the necessary boundary conditions, induce surface plasmon resonance.

As the wavelength of the evanescent wave is a function of the incident angle on the interface, the resonance effect will only occur around a given incident angle. If the evanescent wave successfully induces a resonance effect, a portion of the power from the evanescent wave is absorbed. This means that the Fresnel coefficients describing reflection will no longer equal unity, as they would normally do when $\theta_i > \theta_c$. This effect can be used to measure the combined resonance frequency of the metal and water. If the incident angle of light is varied and the intensity of the corresponding reflected wave is measured, we will see a dip in the reflected intensity at a given incident angle θ_{spr}, as sketched in figure 2.12. The resonance frequency is, as mentioned, determined by the inherent resonance frequency of the metal layer combined with the resonance frequency of the water sample, which again depends on the refractive index of the water. When the refractive index of water changes, the resonance frequency and θ_{spr} will also vary accordingly.

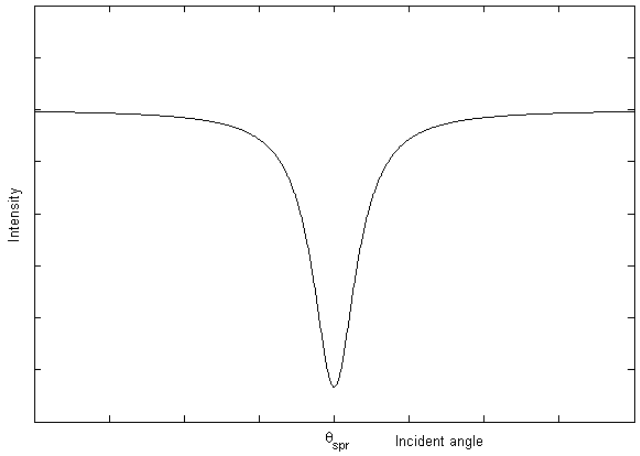

Figure 2.12: Reflected intensity from SPR as a function of incident angle

Some of the articles cited use a fiber optic approach in stead of a prism, measuring the transmitted power through a portion of the fiber where the cladding is removed and replaced by a thin metallic layer. The effect will be the same, but instead of varying the angle of incidence, one tunes the instrument to observe only one of the slopes associated with the resonance dip in figure 2.12 by careful choice regarding the thickness of the metallic layer. It is also possible to keep the angle fixed and use a variable wavelength light source, as this will have the same effect as changing the incident angle. The proposed method requiring a prism could be replaced by placing metal coated nano particles facing the water sample and shine a laser through the liquid and the particles. The same attenuative effect will occur and one can measure the loss in transmitted power through the liquid

The reported sensitivity to refractive index change is of order 10^{-5}. [13] The method has an advantage considering the impact of varying environmental parameters, as it is possible to limit the effect of case structural variations by attaching both the sensor and light source to the prism.

One can also measure the refractive index of a water sample by looking a the reflected power from a fiber optic probe dipped in water. The Fresnel coefficients governing the amount of light being reflected in the interface between the fiberoptic probe and the water sample is dependent on the refractive index of the water sample. A design described in ref [33] measures the reflected optical power from a fiber optic probe immersed in water. The light from the laser source is split, one fiber probe is immersed in the water sample while the other reference probe is in air. They achieve a refractive index sensitivity of $2 \cdot 10^{-5}$.

2.3.5 Comparison of methods

The different methods for measuring the refractive index of a seawater sample are compared and evaluated in table 2.1. The score given to each instrument in the resolution-to size criterion is fairly objective since they are based on calculations and published documentation, while the scores on the environmental immunity are subjective considerations on the authors account. The scores are based on the discussion already presented. To sum this up the interferometer singles itself out in regard to resolution, while all the other methods are capable of average results. The effect of temperature and pressure changes is considered to be most influential for the interferometric method. The other instruments are better suited to resist these effects.

The criteria presented can be interpreted in several ways, depending on which criterion being regarded as most important for the instrument. By simply adding the marks together, the instrument using the total internal reflection method would be favorable. But as this technique is very well known and no method of improving the setup seem obvious, this weakens its position.

The refractometer has a good theoretical sensitivity to change in refractive index and new light displacement sensors makes it possible to achieve a good sensitivity to size ratio. The size criterion is an important one and as discussed earlier, it is possible to construct very sensitive instruments if one has no size constraints. Size versus sensitivity will be a trade off point when designing the instrument. Another advantage is its simple and robust design. That no working in-situ instrument with comparable sensitivity has been found to exist as of today, also makes it more interesting to explore the potential of this method.

Method	**Resolution/size**	**Environment immunity**
Refractometer	**	**
Interferometer	***	*
Total internal reflection	**	***
Other techniques	**	***

Table 2.1: Comparison of methods for measurement of refractive index.
*** = Good, ** = Average, * = Unsatisfactory

2.4 Basic principles of instrument components

This section will present specific theoretical background for the electronic and optical components used in the instrument.

2.4.1 Position sensitive detector

The one dimensional position sensitive device used in this experiment is a Hamamatsu S3932 and the technical specifications are taken from its data sheet [34]. The detector was chosen for of its minimum detectable displacement ΔX_{min}, given in the data sheet as $0.3\mu m$ under ideal circumstances. The active area of the detector has length of $12mm$ and a width of $1mm$. As shown in section 2.2.2, the responsivity of the photodetector is a function of the wavelength of the incident light. The data sheet of the photodetector gives this value as $S \approx 0.4^{A}/_{W}$ at $635nm$.

A Position Sensitive Detector (PSD) is a non-segmented photosensor that gives continuos electrical signals based on the position of the incoming light relative to the center or edge of the active area. The operating concept of the PSD is that light hitting the active area of the device will excite electrons from the valence band into the conduction band through the photovoltaic effect. Figure 2.13 gives a cross sectional view of a typical PSD and describes the PIN type structure of the PSD. The P-type layer is resistive and connected to electrodes at each end, and the N-type layer is connected to ground. The total resistance of the P-type layer is denoted interelectrode resistance R_{ie}. The charge generated by the light spot will cause a photocurrent between the position of the light spot centroid and the two electrodes. The centroid position is defined as a weighted mean position, where a given position X_{pos} is weighted by its intensity I. We can express a one dimensional centroid mathematically as [35]:

$$Centroid = \frac{\sum X_{pos} \cdot I}{\sum I}.$$

The total current will be directly proportional to the level of incident light, as in a common photodiode. [36] We can consider the circuit as an incoming current equaling the photocurrent i_p being divided by current division in two imaginary parallel resistances R_1 and R_2. The two resistances span from the position of the incident light to each electrode X_1 and X_2. We can define the total length of R_{ie} as L_x. We can then find the magnitude of these two resistances by multiplying R_{ie}

with the fraction of the distance from X_1 and X_2 to the point of light incidence to L_x. If we define X_A as the distance from the center of the PSD to the point of light incidence, we can express these resistances as:

$$R_1 = R_{ie}\frac{\frac{L_x}{2} + X_A}{L_x} \text{ and } R_2 = R_{ie}\frac{\frac{L_x}{2} - X_A}{L_x}.$$

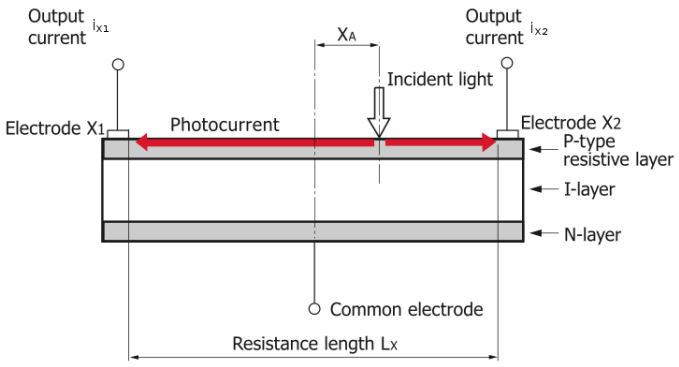

Figure 2.13: Schematic cross section of position sensitive detector. [36]

The current through each of these resistors i_{X_1} and i_{X_2} can be expressed by current division in a parallel circuit as:

$$i_{X_1} = i_p\frac{R_2}{R_1 + R_2} = i_p \cdot \frac{\frac{L_X}{2} - X_A}{L_X} \tag{2.54}$$

$$i_{X_2} = i_p\frac{R_1}{R_1 + R_2} = i_p \cdot \frac{\frac{L_X}{2} + X_A}{L_X}. \tag{2.55}$$

Combining expression 2.54 and 2.55 gives the following expression for the position of the light beam X_A, when $i_p = i_{X_1} + i_{X_2}$

$$\frac{i_{X_2} - i_{X_1}}{i_{X_1} + i_{X_2}} = \frac{i_p(\frac{\frac{L_X}{2}+X_A}{L_X} - \frac{\frac{L_X}{2}-X_A}{L_X})}{i_p} = \frac{2X_A}{L_X}. \tag{2.56}$$

The difference of the two currents, which by itself provides a position information, is divided by the sum of the two signals to normalize the result. This means that the position information is independent of the incident power and total generated photocurrent.

The position detection error of the detector is the difference between the physical position and the calculated position of the laser spot. Slight inaccuracies in the resistive layer in figure 2.13 will give rise to an electrical center position,

which may differ slightly from the geometrical center. This error is largest at the extreme positions and small in the center. This is caused by the fact that some of the light from the laser spot will fall outside the active area of the detector when the beam center position approaches the extreme positions. In this project the laser spot is initially $1\,mm$ wide and the sensor is $12\,mm$ wide. If we consider the case where the center of the light spot approaches one of the ends of the detector, the edge of the spot will reach the edge of the detector when the center of the spot is $0.5\,mm$ from the edge. This reduces the effective part of the active length to $11\,mm$. If we also consider that the laser spot size most likely will be a bit larger after transmission through the prisms, it is fair to conclude that the effective part of the active length is reduced even further. For the purpose of further calculations in this text we define the active length to $10\,mm$.

To extract information from the PSD one needs a circuit with amplifiers and arithmetic components to perform the calculations in equation 2.56. The specific signal processing circuit used in this experiment is a Hamamatsu C3683-01. It is made specifically for the S-3932 PSD. Figure 2.14 describes the circuit which was sketched by the author on the basis of generic Hamamatsu information on similar processing circuits as no diagram of the C3683-1 was available. The two signal currents are pre amplified and converted to voltage, then summed and subtracted as necessary and finally divided in the analog divider. The only parameters given in the data sheet are the feedback resistance and capacitance of the preamplifier. The magnitude of the other resistors are assumed to be neutral in terms of gain at the sum and subtract operational amplifiers. [37] The signal processing circuit is supplied with $\pm 15\,.V$ DC voltage.

The feedback resistor R_f of the preamplifier is given in the data sheet of the driver circuit as $100\,k\Omega$, while $C_f = 1000\,pF$. The current to voltage gain G of an ideal inverting amplifier is defined as the ratio of the output voltage $V_o = -i \cdot Z_f$ to the input current i where $Z_f(f) = \frac{R_f}{1+j2\pi C_f R_f}$ is the feedback impedance. [38]

$$G_{pre}(f) = \frac{V_o}{i} = -\left|Z_f\right| = -\frac{R_f}{\sqrt{1+(2\pi f\, C_f R_f)^2}}. \tag{2.57}$$

If we assign values to the equation and plot the gain as a function of frequency we get the result in figure 2.15. We see that the low frequencies are amplified up to the cutoff frequency of $1588 Hz$, defined as where the amplitude is $\frac{1}{\sqrt{2}} \approx 0.707$ of that in the passband. In this project we can safely assume that the rate at which the refractive index of the ocean water is changing is far below $1.6\,kHz$.

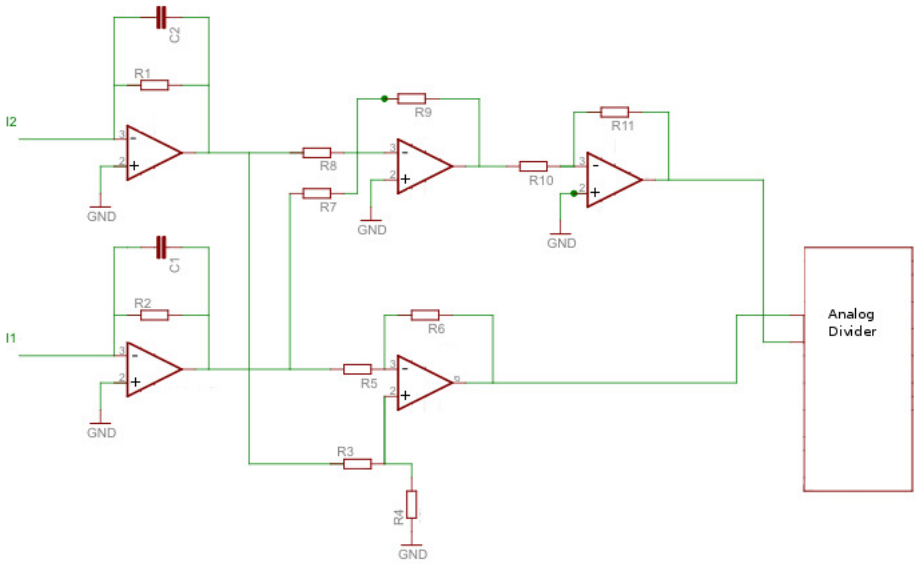

Figure 2.14: Diagram of signal processing circuit Hamamatsu C3683-01

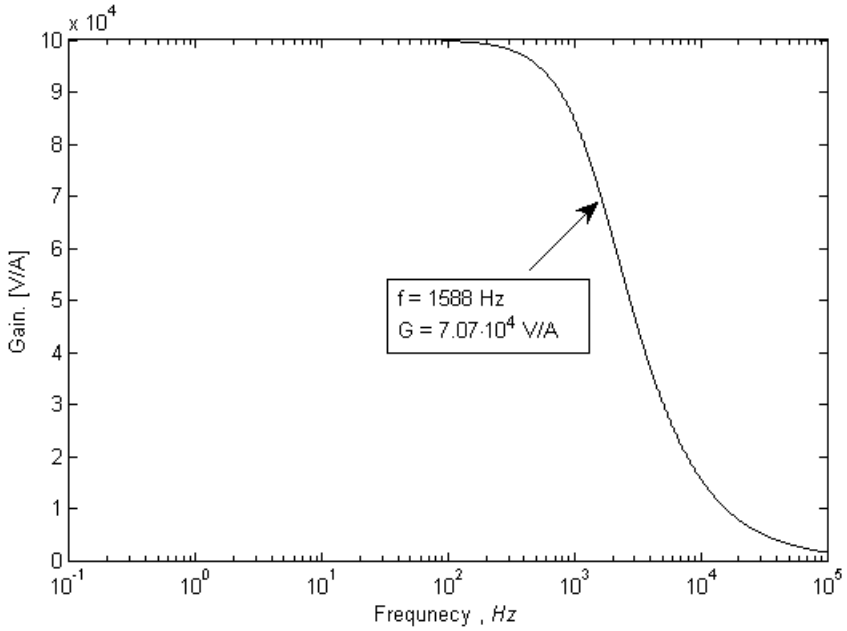

Figure 2.15: Frequency dependence of gain

This means that the pre amplifier gain can be approximated to:

$$G_{pre} \approx -R_f = -1 \cdot 10^5 \frac{V}{A}. \tag{2.58}$$

From figure 2.14, we can see that the signal from the preamplifiers are input to sum and difference inverting amplifiers of unity gain. This makes the overall gain equal to the preamplifier gain, but positive:

$$G \approx -G_{pre} = 1 \cdot 10^5 \frac{V}{A}. \tag{2.59}$$

The saturation current of the photodetector is $i_{sat} = 1 \cdot 10^{-4}\, A$.[34] This gives a maximum output voltage of the preamplifier of $-10\, V$. The output signal V_{pos} of the analog divider will vary between $-10\, V$ and $10\, V$ as described by

$$V_{pos} = \frac{i_{X_2} - i_{X_1}}{i_{X_1} + i_{X_2}} = \frac{2X_A}{L_X}.$$

Depending on the measured position voltage, the position of the incident light beam is given by equation 2.56 when the length of the detector $L_x = 12\, mm$.

$$X_A = V_{pos} \cdot 6 \cdot 10^{-3}\, m. \tag{2.60}$$

The circuit also outputs the sum voltage from $V_{sum} = 0 - 10\, V$, which represents the total generated photocurrent i_p.

2.4.2 Quadrant cell photodiode

The quadrant cell photodiode module acquired for this project is called QD-50-6-18u-2SD and has an integrated driver circuit. The quadrant cell photodiode detector is a segmented light beam displacement sensor. The circular detector is divided into four sectors, each of them being a separate photodiode. The diameter of the detector is $d_{detector} = 7.80\, mm$. The total size of the circuit board with signal processing circuit and detector is only $2.54 \times 3.81\, cm$. The module is supplied with $\pm 15\, V$ DC voltage.

The operating principle of the detector is to measure the generated photocurrent from each of the four sectors of the detector. By comparing the photocurrents measured, which are proportional to the incident light power as de-

scribed in equation 2.48, in each sector it is possible to calculate the position of the center of the light beam. To obtain good results in a displacement measurement it is important that the shape of the laser beam is as symmetrical as possible. The quadrant detector requires the laser spot to be circular if the displacement should be measured in two dimensions and the intensity distribution within the spot should be homogeneously dispersed around the circle at any given distance from the center of the beam. A circuit diagram of the quadrant cell photodiode module with integrated amplifier circuit used for this project is shown in figure 2.16.

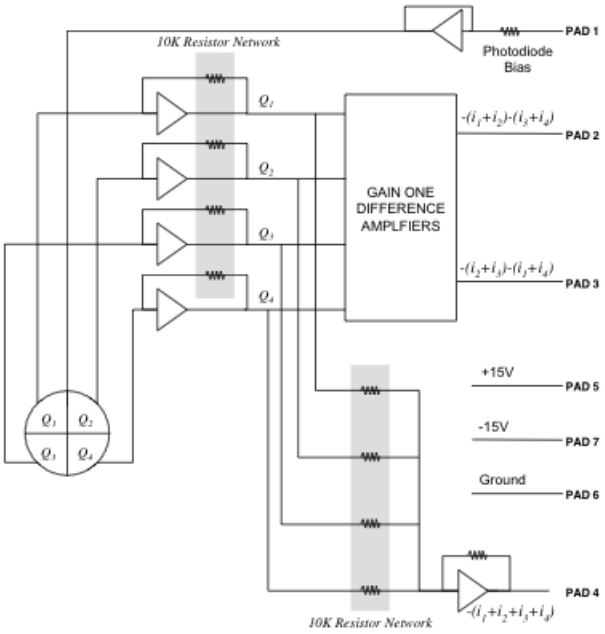

Figure 2.16: Driver circuit of quadrant cell photodiode module. The photocurrent from each photodiode Q_i is preamplified and input to the difference amplifier, which provides the difference signal as output. [39]

The photocurrents i_s from each photodiode Q_s, where $s = 1, 2, 3$ and 4 are amplified in the preamplifiers. As the detector gives displacement information in two dimensions, we must calculate the difference of the two upper versus the two lower sets of diodes to get the vertical displacement along an y-axis, and the difference of the two leftmost versus the two rightmost sets of diodes to get the horizontal displacement along an x-axis. This is done by the unity gain difference amplifiers in figure 2.16. The sum of all the inputs is also calculated, as this will be used to normalize the measurement and make it independent of fluctuations in the incident laser power. As one dimension is sufficient for the measurement in this project, we can forget the vertical difference and express the output voltage

from the horizontal difference as:

$$V_H = G_{quad}\left[(i_1 + i_3) - (i_2 + i_4)\right].$$

The output voltage of the sum will be:

$$V_{sum} = G_{quad}\left[i_1 + i_2 + i_3 + i_4\right].$$

The dimensionless lateral displacement ratio along the x-axis is then found by dividing the position voltage V_H with the total output voltage V_{sum}.

$$\frac{V_H}{V_{sum}} = \frac{(i_1 + i_3) - (i_2 + i_4)}{i_1 + i_2 + i_3 + i_4}. \tag{2.61}$$

To interpret this result and affix a measure of length to it we must examine how the detector works. If we assume that the laser spot is centered on the detector along the y-axis and that $i_1 + i_3 = 0$, the entire laser spot is on the right side of the detector and as long as this is the case, no position information can be gathered. This means that the laser spot diameter d_{laser} should equal half the diameter of the detector $d_{detector}$ to utilize its entire active area. If this is the case, we can affix units of length to equation 2.61. If $i_1 + i_3$ approaches zero we know that the center of the beam is located in the rightmost half, one quarter of the length of the detector diameter away from the center. In this case it will be the position $x = -\frac{d_{laser}}{2}$. The same will apply for the opposite instance when $i_2 + i_4$ approaches zero, giving a position of $x = \frac{d_{laser}}{2}$. Outside these boundaries, we see that the expression 2.61 will assume the value of ± 1 regardless of the value of $i_2 + i_4$.

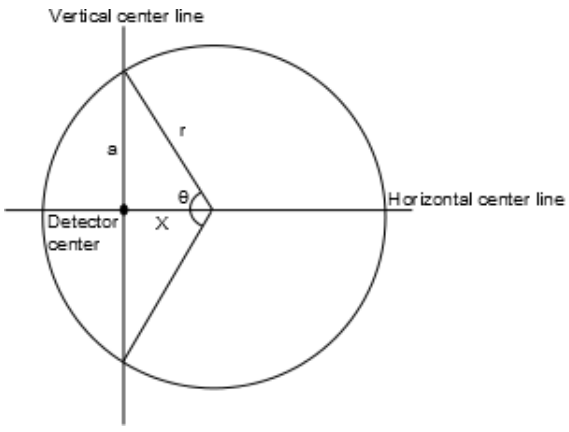

Figure 2.17: Circular laser beam on quadrant detector

In between the boundaries we must consider the shape of the beam to evaluate the fraction of the total beam area occupying each side of the center

line of the detector. If the beam had a square shape the relation would be linear, but the circular shape shown in figure 2.17 gives a more complex relation. The area of the circle sector confined by lines from the center of the beam to the detector vertical center line is given as $A_{sector} = r^2\frac{\theta}{2}$, where r is the radius of the beam spot and θ is the angle defining the circle sector. We can express the angle $\frac{\theta}{2} = arccos(\frac{X}{r})$ where X is the distance from the center of the detector to the center of the beam spot, which we want to quantify. The area of the triangle defined by the lines a, r and X is $A_{triangle} = \frac{X}{2}\sqrt{r^2 - X^2}$. If we subtract the area of the triangle above and below the detector horizontal center line from the area of the circle sector we get the area of the circle occupying the opposite side of the vertical center line compared to the beam center:

$$A_{opposite} = r_{laser}^2 arccos(\frac{X}{r}) - X\sqrt{r^2 - X^2}.$$

The total area of the beam is $A_{circle} = \pi r^2$. We can then replace the elements in the displacement ratio in equation 2.61 and get:

$$\frac{V_H}{V_{sum}} = \frac{A_{opposite} - (A_{circle} - A_{opposite})}{A_{circle}} = \frac{2\left(r^2 arccos(\frac{X}{r}) - X\sqrt{r^2 - X^2}\right)}{\pi r^2} - 1. \tag{2.62}$$

Figure 2.18 shows a plot of this relationship when $r_{laser} = 0.5\,mm$ to make it clear that a linear approximation would not be very accurate when the beam center approaches the edges of the detector. It should also be noted that equation 2.62 assumes a homogeneous intensity distribution, and that a gaussian intensity distribution may alter the plot.

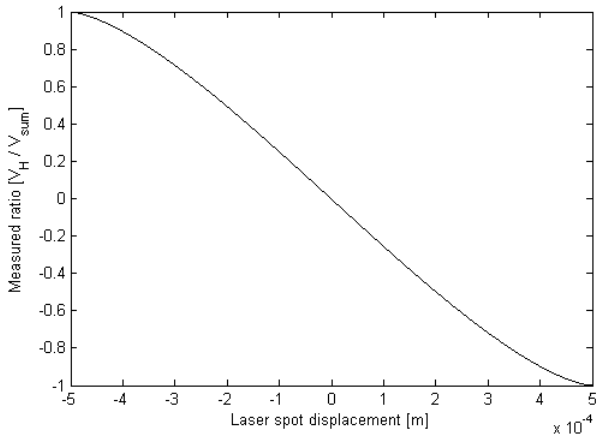

Figure 2.18: Theoretical position voltage ratio as a function of laser spot displacement X

2.4.3 NTC Thermistor

The temperature sensor used in this setup is a negative temperature coefficient thermistor. A thermistor is a resistive temperature element made of semiconductor material. The resistance of these elements decrease with increasing temperature, or can be said to have a negative temperature coefficient. This is caused by the creation of electron-hole pairs in the semiconductor material as the temperature of the thermistor material is increasing. These electron-hole pairs will conduct and that causes the resistance to drop. This is contrary to most metals, in which the resistance increases with temperature. The relationship between temperature and resistance is exponential and can be expressed by [38]:

$$R_T = Ke^{\frac{\beta}{T}}, \tag{2.63}$$

where R_T is the resistance at temperature T in Kelvin. K and β are constants for the thermistor. To utilize a thermistor in a measurement setup it is necessary to construct a signal conditioning element to convert the resistance to a measurable signal, such as a DC voltage signal. This can be done by constructing a Wheatstone deflection bridge or by a simpler voltage divider circuit. If a linear relationship between temperature and output voltage from the signal conditioning element is needed, the deflection bridge is the obvious choice. If a linear transfer function is unnecessary, the voltage divider circuit can be used, as illustrated in figure 2.19. The equation describing the output voltage from this circuit is

$$V = V_{CC}\frac{R_T}{R + R_T}, \tag{2.64}$$

where V_{CC} is the supply voltage, R is a resistor and R_T is the thermistor. The voltage V will be read by the data acquisition device. By combining equations 2.63 and 2.64 we get the expression for temperature as a function of the measured voltage:

$$T = \frac{\beta}{ln\left(\frac{V \cdot R}{K(V_{CC} - V)}\right)}. \tag{2.65}$$

2.4.4 Prisms

The prisms used in this project are made up of two different materials, Zinc Zelenide ($ZnSe$) and borosilicate crown glass $BK-7$ which is made from a

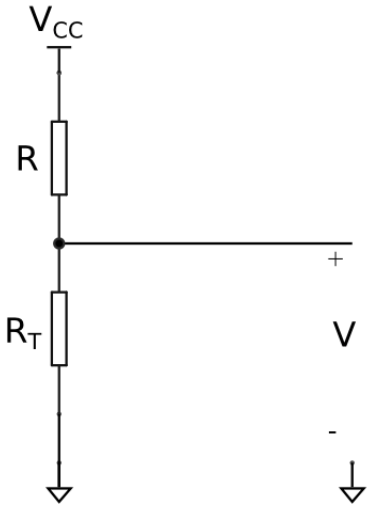

Figure 2.19: Voltage divider circuit

specific ratio mix of boron oxide and silica. The $ZnSe$ prism was chosen for its high refractive index, which was necessary to achieve the desired beam geometry of the instrument. The $BK-7$-prism was chosen because of its low price, as no specific quality was required. This section will explain the important properties of these prisms. The refractive index of a material has been shown to be dependent on the wavelength of the light and this dependence is referred to as dispersion. The Sellmeier equation from 2.29 is used to describe this relationship. The three elements of the sum each describe an absorption resonance of strength B_i and wavelength C_i in the infrared, visible or ultraviolet part of the spectrum. [40, 41, 17]

$$n^2(\lambda) - 1 = \frac{B_1\lambda^2}{\lambda^2 - C_1} + \frac{B_2\lambda^2}{\lambda^2 - C_2} + \frac{B_3\lambda^2}{\lambda^2 - C_3}. \tag{2.66}$$

$B_{1,2,3}$ and $C_{1,2,3}$ are called the Sellmeier coefficients. The empirically determined coefficients and resulting refractive indices for the substances used in the prisms in this project are described in table 2.2. We can try to calculate the value of one of these coefficients by looking at equation 2.28. The resonance strength B can be expressed in terms of number density of molecules N and the resonance frequency λ_0 as:

$$B = \frac{Ne^2\lambda_0^2}{4\pi^2c^2m\epsilon_0}, \tag{2.67}$$

where $e = 1.6 \cdot 10^{-19}\,C$ is the electron charge, $\epsilon_0 = 8.85 \cdot 10^{-12}\,{}^{F}/_{m}$ is the permittivity of free space, $m = 9.1 \cdot 10^{-31}\,kg$ is the mass of the electron and $c = 3 \cdot 10^{8}\,{}^{m}/_{s}$ is the speed of light in vacuum. We can define $N = \frac{N_A}{M_{ZnSe}} \cdot \rho_{ZnSe}$ where $N_A = 6.02 \cdot 10^{23}\,{}^{1}/_{mol}$ is Avogadros number, $M_{ZnSe} = 144.35\,{}^{g}/_{mol}$ is the molar mass of $ZnSe$, and $\rho_{ZnSe} = 5.27\,{}^{g}/_{cm^3}$. We know that C is the square of the resonance frequency. If we chose the value of $C_1 = 0.192\,\mu m^2$ from table 2.2

we can calculate the value of $B_1 \approx 4$. The calculated value deviates a little bit from the empirically determined value in the table. If we do the same calculations for B_2 and B_3 the deviations are much bigger. To explain this deviation we can look at the derivation of the Sellmeier equation. We based our model on the classical model of the oscillations of one electron. In a simple atom such as the hydrogen atom a similar model could be used successfully, [42] but this model will not suffice when dealing with $ZnSe$ which has 74 electrons and has to be treated with a quantum mechanical approach.

Substance	**Zinc Selenide, ZnSe**[41]	**Borosilicate glass, BK-7**[43]
λ	$0.635\mu m$	$0.635\mu m$
B_1	4.2980149	1.03961212
B_2	0.62776557	0.231792344
B_3	2.8955633	1.01046945
C_1	$0.1920630\,\mu m^2$	$0.00600069867\,\mu m^2$
C_2	$0.37878260\,\mu m^2$	$0.0200179144\,\mu m^2$
C_3	$46.994595\,\mu m^2$	$103.560653\,\mu m^2$
Refractive index, n	2.58	1.51

Table 2.2: Sellmeier coefficients and refractive index for prism substances at room temperature.

Dispersion in prisms The Sellmeier equation gives the refractive index as a function of wavelength. A graphical representation of the Sellmeier equation for both prisms is presented in figure 2.20. From table 2.2 we see that the $ZnSe$ prism has a resonance peak at $0.378\mu m$, to which we own the steep decline in the figure. The $BK-7$ prism has no resonance peaks in the immediate vicinity, and therefore the refractive index appear to be constant in the wavelength range in the figure. To determine how the refractive index of a material is dependent on changing wavelength, one can differentiate equation 2.66 with regards to λ and obtain the following result when assuming $\lambda = 0.635\mu m$ and Sellmeier constants for ZnSe and BK-7 respectively:

$$\frac{\partial n_{ZnSe}}{\partial \lambda} = -0.5603\mu m^{-1} \text{ and } \frac{\partial n_{BK7}}{\partial \lambda} = -0.03192\mu m^{-1}.$$

When combined with measurements of laser wavelength fluctuations $\Delta\lambda$, we can express the uncertainty of the refractive indices of the prism.

Thermo-optic properties of prisms The refractive index of a material is not only related to the wavelength of the incoming light. It is also dependent on the

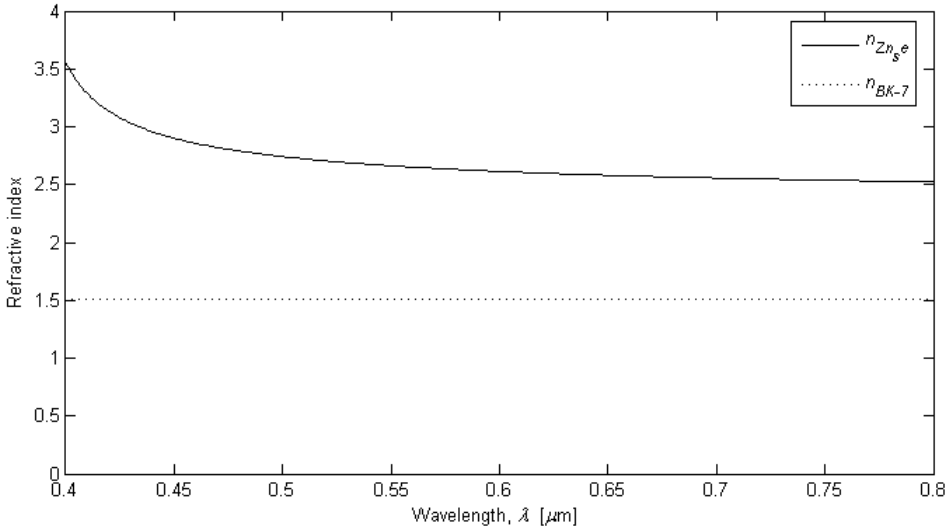

Figure 2.20: Dispersion of prisms

temperature as shown in equation 2.27. We can simplify this equation to:

$$\frac{n^2-1}{n^2+2} = \frac{A}{T},$$

where $A = \frac{P_r N_A N e^2}{3\epsilon_0 m R(\omega_0^2 - \omega^2)}$. This suggest that the refractive index of a prism should drop when the temperature increases, which makes sense as increasing temperature often makes materials less dense resulting in a decreasing refractive index. This is however not the case for the substances used in this instrument. The refractive index of a Zinc Selenide crystal or borosilicate glass actually increases with increasing temperature. [44, 21] This must imply that other temperature dependent mechanisms are dominating the thermal expansion. Increase in temperature will affect how the electrons oscillate when an electromagnetic field is applied, as described in section 2.1.1. This will affect both the resonance frequencies and the resonance strength, which as explained earlier corresponds to the Sellmeier coefficients C and B. [45] This means that these coefficients will be temperature dependent and not constant, as indicated earlier. As the mentioned mechanisms are difficult to quantify theoretically, empirical models for each temperature dependent $ZnSe$ Sellmeier coefficient have been made and fitted to measurement data. [45] The resulting temperature derivative of this temperature dependent Sellmeier equation suggest a thermo-optic coefficient at 20^o for light at a wavelength of $0.635\mu m$ of approximately

$$\frac{\partial n_{ZnSe}}{\partial T} \approx 1.1 \cdot 10^{-4}\, K^{-1}.$$

For the BK-7 prism, a similar method has been used to empirically determine an expression for the thermo-optic coefficient. [21] This suggests a room temperature value of the thermo-optic coefficient at a wavelength of $0.635\mu m$ as

$$\frac{dn_{BK7}}{dT} \approx 9 \cdot 10^{-6}\, {}^{o}C^{-1}.$$

These values describe how the refractive index of the prism changes with temperature. This dependency could affect the sensitivity of the instrument in this project if the temperature of the prisms changes while performing measurements. We can calculate the approximate temperature change dT in a prism of mass m_{prism} and specific heat constant c_{prism} from the quantity of heat dQ flowing into it [16]:

$$dT = \frac{dQ}{m_{prism} c_{prism}}. \tag{2.68}$$

This means that we can calculate the approximate change in refractive index ∂n_{prism} from the thermo-optic coefficient and quantity of heat the prism experiences.

Attenuation in prisms Attenuation in optics is the phenomenon taking place when the power of an electromagnetic wave of is reduced when passing through a medium. It consists of two primary mechanisms, absorption and scattering. Absorption at visible frequencies can be explained as in section 2.1.1. Considering the oscillations of electrons in an atom caused by an incident wave, we see that the differential equation describing electron displacement in equation 2.6 accounts for the loss of energy in this process with the dampening constant γ. If we look at equation 2.27, this absorption is still present in the expression for the refractive index, making the refractive index complex. In most cases involving calculation of refractive index we can disregard the contribution from the imaginary part of the refractive index, especially if the wavelength of the light source is far away from the resonance wavelengths of the medium in which it propagates. However, absorption will take place and must be accounted for.

Scattering is when the direction of travel of the photons are changed by interaction with any kind of matter. This effect causes the photons of the light beam to be scattered away from the detector, causing less power to reach the detector. As the instrument setup is based on transmission, the effect of scattering will not be significant apart from the power loss. The most convenient way to threat the apparent power loss in a medium is by the use of the Lambert-

Beer law given as [16]

$$I = I_0 e^{-\alpha l}, \tag{2.69}$$

where I is the transmitted intensity, I_0 is the incident intensity, $\alpha = a + b$ is the attenuation coefficient, a is the absorption coefficient, b is the scattering coefficient and l is the length of the medium. α will be dependent on a which again depends on the complex refractive index of the medium and thereby on the dampening constant γ. As the refractive index is frequency dependent, so will also the attenuation coefficient. [17] If we measure the incident and transmitted intensity through a sample we can determine the total attenuation constant.

2.4.5 Water samples

The seawater samples used in this experiment is constructed on the basis of ordinary seawater from "Byfjorden" in Bergen. The samples with salinities lower than ordinary seawater have been diluted with a given amount of H_2O to get a given salinity reading. The sample with higher salinity than the ordinary seawater has been heated to evaporate some of the H_2O. The salinity of the samples are then measured by a Guildline 8410A Portsal salinometer based on the conductivity principle. [46] Its accuracy is given as $0.003\,psu$. The seawater has not been classified by other instruments, and the exact contents of the samples are therefore not known.

In addition to the seawater samples, Sodium Chloride ($NaCl$) solutions will also be used. These samples are constructed from $NaCl$ (99.9% from Sigma Aldrich) in crystalline form and H_2O. By using a balance, the samples have been constructed by adding a given amount of salt to the water, thereby giving exact knowledge of the contents of these samples. Table 2.3 gives an overview over the different samples used to test the instrument.

Seawater		$NaCl$ **solution**	
Sample nr	**Salinity [psu]**	**Sample nr**	**Solution [g/100g]**
0	0	0	0
1	4.9550	1	0.5
2	9.7878	2	1.0
3	14.5825	3	1.5
4	19.4697	4	2.0
5	24.3133	5	2.5
6	28.8126	6	3.0
7	31.6046	7	3.5
8	34.5288	8	3.6
9	36.2654	9	4.0

Table 2.3: Water samples used in the experiment

Refractive index of a sodium chloride solution A sodium chloride solution is a mixture of distilled water and sodium chloride, $NaCl$. The refractive index of the pure water will be governed by the Clausius-Mossotti relationship from equation 2.21. The work by Schiebener et al. in 1990 describes this relation in a semi empirical manner and has been accepted as the international standard for the determination of refractive index in pure water and steam. [47, 48] The work describes the process of curve fitting a set of measurement data by the least square method to the Lorentz-Lorenz function. The Lorentz-Lorenz function, as explained in section 2.1.3, is a variation of the Clausius-Mossotti relation. The measurement data consisted of precise measurements of wavelength, temperature and density, as well as resulting refractive index. The equation is given in appendix B.1. This equation fails to describe the contribution of the sodium chloride content of the solution to the refractive index and a similar thorough investigation of refractive index in a sodium chloride solution has not been found in the literature. Some sources do however give information about the relationship between refractive index and concentration of sodium chloride in a solution. [49, 50] Under constant temperature at 20^o and atmospheric pressure and with a $HeNe$ laser with a wavelength of $632.8\,nm$, the relationship between the refractive index n and the salt concentration C in $^g/_{100g}$ is known to be linear with $\frac{dn}{dC} = 1.7 \cdot 10^{-3} \%^{-1}\, ^{100g}/_g$.

If we combine equation B.1 with the slope $\frac{dn}{dC} = 1.7 \cdot 10^{-3}\, ^{100g}/_g$ we have a relationship combining the refractive index, wavelength, temperature and salt concentration. By first calculating the refractive index of a pure water sample by the formula given by Schiebener et al., and then calculate the refractive index of the solution by adding the product of C and $\frac{dn}{dC}$. We can assigning values to the

variables of equation B.1 in accordance with the instrument setup and assuming a water density ρ of pure water at room temperature of $998\,kg/m^3$ as stated in Ref [51], we get a simplified expression given as:

$$n(T) = \sqrt{\frac{1.411 - 0.250 \cdot 10^{-4} \cdot T}{0.794 - 0.125 \cdot 10^{-4} \cdot T}},$$

where T is the temperature in Celsius. We can then add the slope of the salt concentration function $\frac{dn}{dC}$ and get an expression for the refractive index of the solution as a function of temperature and salinity concentration C in $^{g}/_{100g}$:

$$n(T, C) \approx n(T) + \frac{dn}{dC} \cdot C. \tag{2.70}$$

A plot of this equation for a temperature of 22^oC is shown in figure 2.21. We see that in the concentration range of $0 - 4\,^{g}/_{100g}$ we have a variation in the refractive index $\Delta n \approx 0.068$.

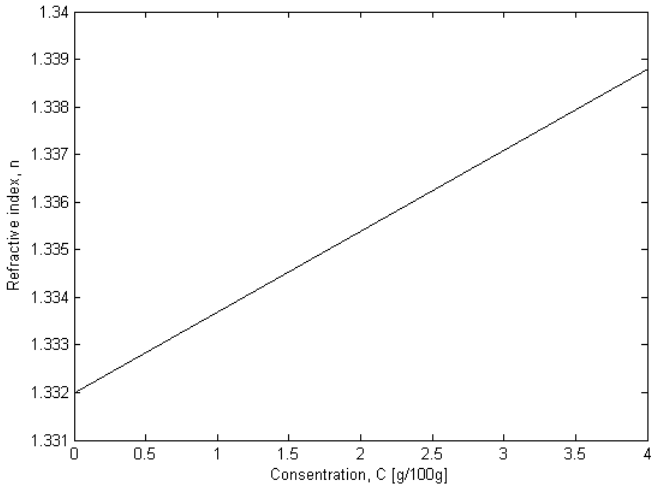

Figure 2.21: Refractive index of $NaCl$ solution as function of concentration in %

Refractive index of seawater The refractive index of seawater is also governed by the Clasusis-Mossotti relation. But as for a sodium chloride solution it is not very practical to take the theoretical approach. Seawater is a very complex composition of salts and other substances, as described in appendix E, and it would be difficult to quantify the contribution of molecular refractivities from all the different substances. The empirical method has therefore been used in an attempt to obtain an "optical equation of state"[14] based on the important parameters such as the wavelength of the incoming light, the pressure and temperature of the water sample. Milliard and Seaver's work on refractive index of seawater pub-

lished in a series of articles during the 1980s culminated in an article 1990 which is a much cited reference in this context. It takes the wavelength, temperature and pressure into account, as well as practical salinity. The relationship, known as the Seaver-Millard equation is given as follows [52]:

$$n(T,\, P_r,\, S,\, \lambda) = n_I(T,\, \lambda) + n_{II}(T,\, \lambda,\, S) + n_{III}(P_r\,, T,\, \lambda) + n_{IV}(S,\, P_r,\, T). \quad (2.71)$$

The total equation consist of 27 terms and is presented in appendix B.2. The four independent variables are T (temperature in ^oC), P_r (pressure in dbar), S (practical salinity in psu) and λ (wavelength in μm). The formula is based on least square method regression over four different data sets describing the refractive index of sea water at different variable values. Together these data sets span the normal oceanographic conditions, given as temperatures between $0 - 30\,^oC$, pressure in the range of $0 - 110\,MPa$ and salinity in the range of $0 - 40\,psu$. The formula is constructed for wavelengths within $0.50 - 0.70\,\mu m$. Since the formula was constructed on the basis of four different data sets with independent accuracy, the standard deviation of the refractive index calculated by the equation will vary from $4 \cdot 10^{-7}$ for distilled water in atmospheric pressure to $8 \cdot 10^{-5}$ for seawater at high pressure.[52, 14]

The work of Quan and Fry from 1995 describes a similar equation based on one of the same data sets used by Millard and Seaver.[53] Their equation is not dependent on pressure, and thereby only applicable at the surface or shallow waters and will not be discussed.To make the instrument as flexible as possible, the Seaver-Millard equation will be used to describe the relationship between refractive index, salinity, temperature and pressure at a fixed wavelength of the laser light.

Salinity dependence We can examine the independent contribution to the refractive index of seawater from each of the variables by assigning values to three of them, while varying the last one. We can start by looking at the refractive index as a function of practical salinity. Figure 2.22 is based on equation 2.71 and shows the refractive index of seawater at standard atmospheric pressure of $10.13\,dbar$ and a temperature of $22\,^oC$, with a laser wavelength of $635\,nm$, giving the following expression [52]:

$$n(T = 22^oC,\, P_r = 10.13dbar,\, S,\, \lambda = 635\,nm) = 1.331518 + 1.806441 \cdot 10^{-4} \cdot S.$$

We see that the refractive index is a linear function of salinity, which correlates with the similar relationship in a $NaCl$ solution described in equation 2.70.

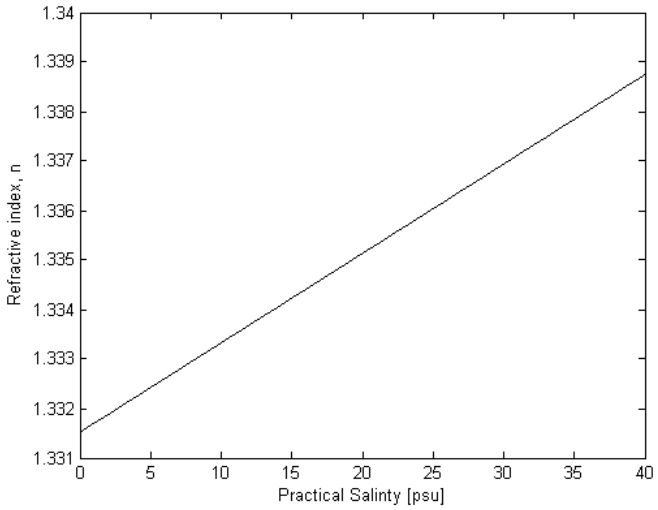

Figure 2.22: Refractive index as a function of salinity

Temperature dependence The refractive index of water is also dependent on the temperature. Figure 2.23 shows this dependence by plotting refractive index as a function of temperature at a salinity of $35\,psu$, wavelength of $635\,nm$ and standard atmospheric pressure of $10.13\,dbar$, from the following equation [52]:

$$\begin{aligned} n(T,\, P_r = 10.13 dbar,\, S = 35\,psu,\, \lambda = 635\,nm) = \\ 1.339522 - 0.3255 \cdot 10^{-4} \cdot T - 0.2623 \cdot 10^{-5} \cdot T^2 \\ + 3.3269 \cdot 10^{-8} \cdot T^3 - 2.0863 \cdot 10^{-10} \cdot T^4 \,. \end{aligned} \tag{2.72}$$

It is clearly visible from the figure that a precise measurement of the temperature is needed to make accurate salinity measurements. At room temperature of 22^oC, in which the experiments will be conducted, the slope of the temperature dependency can be found by differentiating equation 2.72 with regards to the temperature:

$$\frac{dn}{dT}(T = 22^o) = -1.08 \cdot 10^{-4}\ {}^1\!/_{^oC}.$$

This means that the refractive index will vary 1 unit on the fourth decimal for each degree of temperature change.

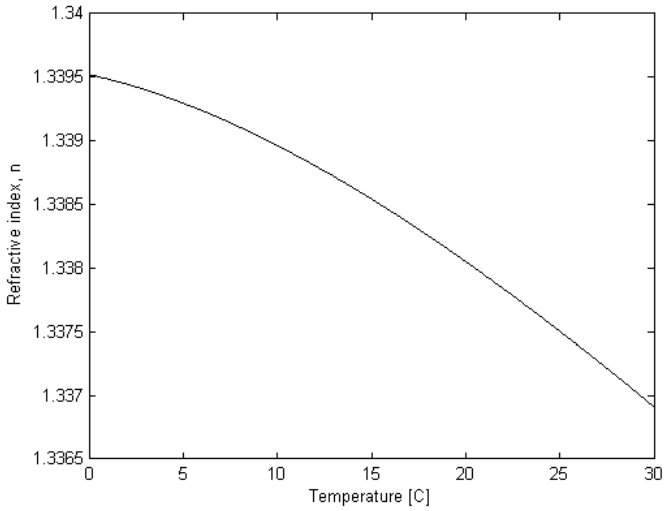

Figure 2.23: Refractive index as a function of temperature

Pressure dependence The refractive index of water is also dependent on the pressure. Although this relation is weak, as the water is almost incompressible, the very high pressure in deep ocean waters of up to $10000\,m$ will contribute significantly to the measurement.[54] The pressure dependence of the refractive index is presented in figure 2.24, with the temperature at 22^oC, the salinity at $35\,psu$ and the wavelength at $635nm$. This gives the following equation [52]:

$$n(T = 22^oC,\, P_r,\, S = 35\,psu,\, \lambda = 635\,nm) = \\ 1.3378266 + 0.14329 \cdot 10^{-5} \cdot P_r - 1.29294 \cdot 10^{-11} \cdot {P_r}^2\,. \tag{2.73}$$

The range of the pressure corresponds to the limits of equation 2.71. If we look at the slope of the pressure dependency we see that it equals approximately $1.4 \cdot 10^{-6}\ {}^1\!/_{dbar}$. The ambient air pressure usually varies no more than $1\,dbar$ in total and within the timeframe of a measurement even less. In standard atmospheric conditions, such as inside a laboratory, the effect of pressure change can therefore be neglected.

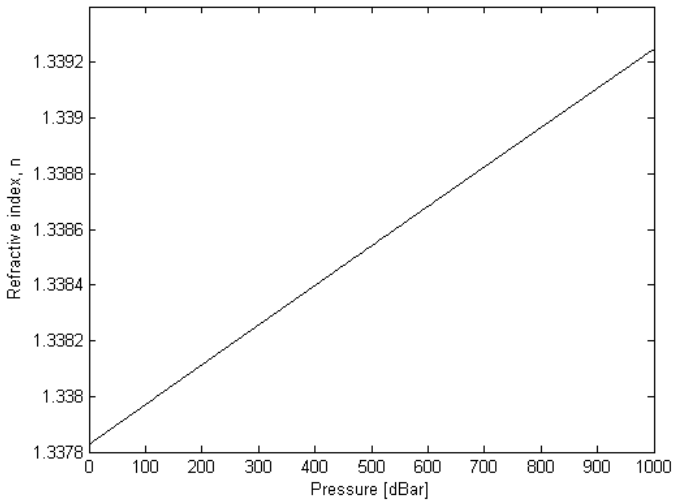

Figure 2.24: Refractive index as a function of pressure in dbar

Salinity as function of refractive index and temperature We can simplify the expression for the Seaver-Millard equation under certain circumstances. Firstly we will disregard the pressure dependency as the variations of atmospheric pressure will be small and their contribution to the measurement will be negligible. We have also determined a constant laser wavelength of $\lambda = 0.635\mu m$. The expression will then be:

$$n(S,T) = A + BT - CT^2 + DT^3 - ET^4 + FS - GST + HST^2 + IST^3. \quad (2.74)$$

The coefficients used in the expression are described in table 2.4, and should not be confused with the coefficients used in equation 2.71. They originate from the original Seaver-Millard constants, but also incorporate the constant laser wavelength and pressure.

Coefficient	Value
A	1.332651769
B	$0.1288718901 \cdot 10^{-5}\, {}^{o}C^{-1}$
C	$0.2937661166 \cdot 10^{-5}\, {}^{o}C^{-2}$
D	$2.904145256 \cdot 10^{-8}\, {}^{o}C^{-3}$
E	$2.086317800 \cdot 10^{-10}\, {}^{o}C^{-4}$
F	$0.1962913218 \cdot 10^{-3}\, psu^{-1}$
G	$9.669553394 \cdot 10^{-7}\, psu^{-1}{}^{o}C^{-1}$
H	$8.966186356 \cdot 10^{-9}\, psu^{-1}{}^{o}C^{-2}$
I	$1.207880000 \cdot 10^{-10}\, psu^{-1}{}^{o}C^{-3}$

Table 2.4: Coefficients used in simplified Seaver-Millard equation

Attenuation in water samples Attenuation in seawater follows from the same derivation as for prisms as described in section 2.4.4. We still define the attenuation as a sum of absorption and scattering. When we consider seawater, we must take into account that it will be composed of several different substances and it will be very difficult to give a theoretically deduced expression for either scattering or absorption. The theoretical explanation of absorption in water at visual frequencies is comparable with that of the prism, being based the loss factor in electron oscillations caused by the incident electric field. As the attenuative effects are simply a source of laser beam power reduction, a simple empirical value for the attenuation coefficient will suffice.

2.5 Measurement errors and reduction techniques

A common property of a measurement system is that it may be sensitive to changes in other parameters than the one it is actually measuring. Some of these error mechanisms may be systematic, since they may influence the instrument in a measurable way. One such example from this project is the way temperature and pressure influence the refractive index of the water. The effect of these parameters on the refractive index is known, and we can compensate for this by measuring their value. The user of the instrument may introduce error by not following the guidelines. Other errors may be random in nature and will cause the measured value to fluctuate around an average value. It is common to assume, and rightly so, that the fluctuations are distributed by a known statistical distribution such as Gaussian distribution. This type of error is called noise and its origin can often be determined by specific measurement methods. There also exists noise caused by interference from the power grid through a power supply or other coupling methods.[55]

This section will describe the sources of error which are assumed to be present in this instrument, and the ways one could reduce its effect on the system. The primary focus will be on the noise sources inherent in optical measurement systems with readout electronics. The noise sources will be presented in the logical order in which they appear, starting with the laser noise and ending with the data acquisition device.

2.5.1 Laser noise

Random fluctuations in the laser power output is a source of noise in an optical measurement system. It is caused by several mechanisms such as mode-hopping, spontaneous emission and laser light feedback. In the generation of laser light from a diode laser, the light generated by the diode is released in an optical cavity or resonator. The light is reflected back onto the laser diode to achieve stimulated emission and amplification of the light power by mirrors. The position of the mirrors in the optical resonator affects the resonant frequency and the possible resonant modes of the resonator. Temperature changes causes thermal expansion and contraction of the mirrors mounts, and thereby causes variations in resonant modes, mode hopping or excitation of multiple modes at the same time, so called mode competition. If the laser is supposed to operate in single mode, this will lead to noise in the from of varying output wavelength of the laser.[56]

If laser light is reflected back into the optical resonator this will cause interference and degradation of the generated laser beam. In the setup of the instrument in this thesis it is avoided by not having any mirrors or lenses at right angles to the laser beam. In addition to this, the current supplied to the laser diode could be infected with noise from the power supply unit, which again will contribute to the total noise output of the laser. To quantify the mentioned noise sources we can describe the electric field of the output of the laser as:

$$E(t) = E_0 \left[1 + \delta_l(t)\right].$$

The noise is described by $\delta_l(t)$ which is a dimensionless, complex quantity and $|\delta_l(t)| \ll 1$. The intensity of the laser is proportional to the electric field, as described in equation 2.52, giving us an expression for the power P as:

$$P \propto |E_0|^2 \left(1 + \delta_l(t) + \delta_l^*(t) + |\delta_l(t)|^2\right) \approx P_0(1 + 2Re\left[\delta_l(t)\right]).$$

This means that the root mean square of the laser power noise equals $2P_0 \left\langle Re\left[\delta_l(t)\right]^2 \right\rangle^{1/2}$ and the generated laser noise current in the detector is given by the responsivity from equation 2.48:

$$i_{ln} = 2P_0 S \Delta l, \tag{2.75}$$

where $\Delta l = \left\langle Re\left[\delta_l(t)\right]^2 \right\rangle^{1/2}$. To measure the laser noise we must first determine the other sources of noise in the detector and detector circuit. When these noise sources are determined we can quantify the the laser noise current by measuring the output of the detector and subtract the other noise sources. While the

fluctuations in output power alone will contribute to noise, it may also affect the beam shape or focal point of the beam. In this instrument, the position of the centeroid of the laser spot is the pivotal point in this matter. We can measure the beam shape and pointing stability over time by using a beam profiler camera. [56, 57, 58]

2.5.2 Optical sensor noise

This section will describe the noise sources associated with the photodetector. We can define four predominant sources of noise in the detector and they will be discussed below. All of these noise sources can be classified as fundamental, meaning that it is not possible to eliminate them entirely. But as the derived expressions will show, we can limit them by modifying certain parameters in the instrument.

2.5.3 Shot noise

Shot noise is noise generated from random generation and flow of mobile charge carriers.[59] If we consider a case with two parallel metal plates at different potential at a distance d from each other, along an axis x, electrons will be released at random from the plate with lower potential to the plate with higher potential with a time average rate of $\bar{N}$. This average rate can be expressed in terms of the ratio of the average current $\bar{I}$ and the electron charge e as $\bar{N} = \bar{I}/e$. We can then go on to define the current pulse from a single electron, as observed in the external circuit as

$$i_e(t) = \frac{ev(t)}{d},$$

where $v(t)$ is the speed of the electron. This is valid as the current $i_e(t)$ is the number of electrons per unit time. We can then Fourier transform the expression for the current pulse [59]:

$$I(\omega) = \mathcal{F}\left[i_e(t)\right] = \frac{e}{2\pi d}\int_0^\tau v(t)e^{-i\omega t}dt,$$

where τ is the time an electron emitted from one plate at $t = 0$ uses to reach the other plate. If $\tau\omega \ll 1$, we can approximate the exponential function to unity. This means that the current pulse can be described by a Dirac δ-function, which has a Fourier transform of unity. This simplifies the expression, and by writing

$v(t) = {}^{dx}/_{dt}$ we get:

$$I(\omega) = \frac{e}{2\pi d} \int_{x(0)}^{x(\tau)} dx = \frac{e}{2\pi d} x(\tau) = \frac{e}{2\pi}.$$

The power spectral density of the this function is given by the Wiener-Kinchin Theorem through the autocorrelation function as [59]:

$$S_i(\omega) = \frac{1}{\pi T} \int_{-\infty}^{\infty} \int_{-T/2}^{T/2} I(t+\tau) I(\tau) e^{-i\omega t} dt\, d\tau = 4\pi \bar{N} \left[I(\omega)\right]^2 = 4\pi \bar{N} (\frac{e}{2\pi})^2 = \frac{\bar{I} e}{\pi}.$$

If we integrate the power spectral density over the desired bandwidth we get the total noise power in this region, represented by a current source with mean squared amplitude of [59]:

$$i_{sn}^2 = \int_{\omega}^{\omega+\Delta\omega} \frac{\bar{I} e}{\pi} d\omega = \frac{\bar{I} e}{\pi} (\omega + \Delta\omega - \omega) = 2\bar{I} e \Delta f. \tag{2.76}$$

This type of noise will exist in a photodetector, as the depletion zone in a p-n junction will act as the two plates of different potential mentioned in the beginning of this section. We see that the noise is not dependent on temperature and is only based on the bandwidth of the signal. From this we can conclude that it is not possible to reduce the effect of this specific noise with modulation to a given frequency band or temperature control at the detector. The only way to reduce the shot noise is to reduce the photocurrent $\bar{I}$ generated in the detector or to reduce the bandwidth Δf. It is very difficult to measure shot noise, and is most conveniently quantized by equation 2.76. We can determine the maximum shot noise current when the maximum average current $\bar{I} = 1 \cdot 10^{-4}\, A$ is the same as the saturation current of the detector and the bandwidth $\Delta f = 10\, Hz$ as:

$$i_{sn} \approx 1.8 \cdot 10^{-11} A.$$

2.5.4 Johnson noise

Johnson noise or thermal noise is a noise source that is always present in electronic circuits. It is caused by random movement of charge carriers in resistive material R due to temperature T_r, and is present even without a current source in the circuit.[59] The position sensitive detector described in section 2.4.1 has a resistive

layer which will cause this noise to contaminate the output signal. The noise also exists in all other resistors, such as amplifiers which will be discussed later.

The following derivation considers the fluctuations in a circuit consisting of two resistors of equal magnitude R connected by a transmission line with characteristic impedance $Z_0 = R$ so that no reflections are present. The two resistors are kept at equal temperature. In this case, the length of the circuit is denoted L, along an axis x. The voltage wave in the circuit can be described as [59]:

$$v(t) = A \cdot cos(\omega t \pm kx),$$

where $k = {}^{2\pi}/_{\lambda}$. If we, as a boundary condition, require that the solutions are periodic at distance L, and assume that we can describe the wave at distances larger than L we get:

$$v(t) = A \cdot cos(\omega t \pm k(x + L)) = A \cdot cos(\omega t \pm kx).$$

This is valid when $kL = 2m\pi$ where $m = 1, 2, 3...$ The number of modes N_m that have values of k between 0 and $k+$ can be found by

$$N_m = \frac{kL}{2\pi} = \frac{fL}{c},$$

where f is the frequency and c is the speed of light. We limit the consideration to waves with positive values of k, traveling in the positive direction on the x-axis. This can then be expressed as the number of modes per frequency interval:

$$\frac{dN_m(f)}{df} = \frac{L}{c}. \tag{2.77}$$

Considering the power flowing in the positive direction through an imagined plane across the transmission line, this power must originate from the resistor at the left side of the circuit. The power is transferred on the different modes of the system. The power can be expressed as energy per time, or energy multiplied by velocity divided by the distance. If we assume that the waves propagate with the speed of light c we can express the power P as the product of the speed of light c, the number of modes per frequency interval $\Delta N_m(f) = \frac{L}{c}\Delta f$ and the energy per mode E_m, all divided by the distance L.[59] In thermal equilibrium the energy E_m of one mode is given by Planck's radiation law as

$$E_m = \frac{hf}{e^{\frac{hf}{kT_r}} - 1},$$

where T_r is temperature of the resistor in Kelvin, h is the Planck constant and k is the Boltzmann constant.[16] This gives an expression for the power being transferred from one resistor to the other:

$$P = \frac{hf\Delta f}{e^{\frac{hf}{kT_r}} - 1}.$$

As long as $f \ll {}^{kT_r}/_{h}$, which is the case in room temperature, we can approximate the exponential function by the first two parts of its Maclaurin series expansion:

$$e^{\frac{hf}{kT_r}} \approx 1 + \frac{hf}{kT_r},$$

and we can approximate the entire expression to:

$$P \approx kT_r\Delta f.$$

If we model the noise power to originate from a current source connected in parallel to the resistors in the circuit, the magnitude of the source will be

$$i_{jn}^2 \approx \frac{4kT_r\Delta f}{R}, \tag{2.78}$$

as the noise current from the source is divided equally on the two resistors. We see that thermal noise is white as it is independent of frequency. To reduce thermal noise we can reduce the temperature in the circuit or reduce the bandwidth of the system. In the instrument being constructed for this thesis, temperature control of the circuit is not considered an option due to size constraints.

We can measure the noise generated in the photodetector by measuring the output current when no light is stimulating the detector. When no photocurrent is generated, the only contribution is from the leakage current noise and Johnson noise in the interelectrode resistor. We can determine the approximate magnitude of the Johnson noise current by using equation 2.78, when the resistor in the detector is $R_{ie} = 50k\Omega$, the temperature is $T_r = 293K$, the bandwidth is $10\,Hz$ and the Boltzmann constant $k = 1.38 \cdot 10^{-23}J/K$:

$$i_{jn} = 1.8 \cdot 10^{-12}A.$$

2.5.5 Generation recombination noise

When photons are incident on a photodetector, the generated charge carrier flux Φ_e is a function of the incident photon flux Φ_p and the quantum efficiency η of the detector, as explained in chapter 2. It is however important to acknowledge that the process is random and that η actually describes the probability that an incident photon will produce a charge carrier pair. In addition to this randomness we must also consider that a generated charge carrier has a lifespan of τ before it recombines, and that the charge carrier will only contribute to the generated photocurrent inside its lifetime.[59] We can express the current pulse of lifetime τ as:

$$i(t) = \begin{cases} \frac{e\bar{v}}{d} & 0 \leq t \leq \tau \\ 0 & otherwise \end{cases}$$

where e is the electron charge, $\bar{v}$ is the average electron velocity and d is the distance between two metal plates at different potential. This can be Fourier transformed and squared:

$$|I(\omega,\tau)|^2 = \frac{e^2\bar{v}^2}{4\pi^2\omega^2 d^2}(2 - e^{-i\omega\tau} - e^{i\omega\tau}). \tag{2.79}$$

The probability function describing the possibility that a charge carrier lives τ seconds is given as $g(\tau) = \frac{1}{\tau_0}e^{-\frac{\tau}{\tau_0}}$, where τ_0 is the average lifetime of a charge carrier. We can then time average equation 2.79 over all possible values of τ [59]:

$$\overline{|I(\omega)|^2} = \int_0^\infty |I(\omega,\tau)|^2 \, g(\tau)d\tau = \frac{2e^2\bar{v}^2\tau_0^2}{4\pi^2 d^2(1+\omega^2\tau_0^2)}.$$

We can then find the power spectral density by Carson's Theorem [59]:

$$S(f) = 8\pi^2\bar{N}\overline{|I(2\pi f)|^2} = \frac{4\bar{N}e^2\frac{\tau_0^2}{\tau_d^2}}{(1+4\pi^2 f^2\tau_0^2)},$$

where $\bar{N}$ is the number of charge carriers generated per second and $\tau_d \equiv {}^{d}/_{\bar{v}}$. This expression can be simplified even more if we define the average current $\bar{I}$ as the product of the average number of charge carriers generated per second $\bar{N}$ and the average charge per charge carrier in the external circuit ${}^{e\tau_o}/_{\tau_d}$:

$$S(f) = 8\pi^2\bar{N}\overline{|I(2\pi f)|^2} = \frac{4\bar{I}e\frac{\tau_0}{\tau_d}}{(1+4\pi^2 f^2\tau_0^2)}.$$

We find the mean squared noise current from generation recombination noise as:

$$i_{gn}^2 = S(f)\Delta f = \frac{4\bar{I}e\frac{\tau_0}{\tau_d}\Delta f}{(1+4\pi^2 f^2 \tau_0^2)}. \tag{2.80}$$

We see that the generation recombination mean squared noise current is inversely proportional to the square of the frequency, meaning that it will contribute less at higher frequencies. It is also proportional to the average generated photocurrent and the bandwidth. To reduce the effect of this noise source we can reduce the bandwidth, minimize the generated photocurrent or measure at higher frequencies. To determine its magnitude we must identify the magnitudes of the variables in the equation. The average lifetime is dependent on the doping level of the semiconductor. If we assume a p-type doped silicon semiconductor with a typical dopant density we get $\tau_0 \approx 10^{-5}s$. [60] We can then find $\tau_d = \frac{d}{\bar{v}}$ where $d = 1.2\,cm$ is the distance between the electrodes of different potential, assumed to be the entire length of the detector, and $\bar{v}$ which is the drift velocity of the electrons. The drift velocity is defined in terms of the electric field E and the carrier mobility in the silicon. If we assume an electric field $E \approx 1^{V}/_{cm}$ and a silicon carrier mobility of $\mu_{Si} = 1350\,^{cm^2}/_{V\cdot s}$ we get $\bar{v} = \mu_{Si}E = 1350\,^{cm}/_{s}$.[18, 59] We then get $\tau_d = 9 \cdot 10^{-4}\,s$. If we use the same values for $\bar{I}$ and Δf as before we get a value for the maximum generation-recombination noise current:

$$i_{gn} \approx 2.6 \cdot 10^{-12} A.$$

2.5.6 Leakage current and ambient light

Leakage current in a p-n junction will also contribute to the total noise figure, even without incident light on the detector. Thermal excitation of minority charge carriers can will cause a leakage current in the detector. Background noise or ambient noise is also an important factor when designing an optical instrument. This is hard to quantify theoretically. It is therefore important to shield the detector from external sources of photons to reduce the impact of background noise. It will however be hard to eliminate this noise contribution completely and it must be accounted for. We can define the combined contribution from the leakage current and ambient current as i_{an}. We can assume that this current is fairly constant if the light conditions remain unchanged during a measurement.

2.5.7 Total noise in optical sensor

To express the total noise in the optical sensor, including all the mentioned noise sources, we must combine them into one to be able to compare it to the experimental values. The fundamental noise sources which can not be eliminated, from the laser in equation 2.75, shot noise in equation 2.76, Johnson noise in equation 2.78, generation recombination noise in equation 2.80 and the ambient/leakage current i_{an}^2, are assumed to be uncorrelated and independent of each other and can therefore be summed to get an expression for the total noise current from the photodetector as done in ref [57]:

$$\begin{aligned} i_n^2 &= i_{ln}^2 + i_{sn}^2 + i_{jn}^2 + i_{gn}^2 + i_{an}^2 \\ &= (2P_0 S\Delta l)^2 + 2\bar{I}e\Delta f + \frac{4kT_r\Delta f}{R} + \frac{4\bar{I}e\frac{\tau_0}{\tau_d}\Delta f}{(1+4\pi^2 f^2\tau_0^2)} + i_{an}^2 \end{aligned} \tag{2.81}$$

The expression for total noise in the detector is a function of output power P_0 the laser and its noise factor Δl, the bandwidth of the system Δf, the average generated photocurrent $\bar{I}$, the temperature of the circuit T_r, different resistors R in the detector and amplifier, the average lifetime of a generated charge carrier τ_0 and the frequency f.

2.5.8 Amplifier noise

The circuit diagram of the amplifier used in the experiment is shown in figure 2.14. The two photocurrents from the detector are pre amplified, then the voltages are summed and eventually entered into the analog divider. The circuit will generate noise of its own, as well as amplify the noise from the sensor. The primary source of noise in the circuit will be that of Johnson noise from the resistors. To analyze the effect of noise in a amplifier network we can apply the Friis noise equation.[61] It defines the noise figure F of an amplifier as the ratio of the signal to noise ratios of the input versus the output as:

$$F = \frac{S_i/N_i}{S_o/N_o},$$

where the input signal equals the generated photocurrent from the detector $S_i = i_p$ and the input noise is the total noise in the optical detector $N_i = i_n$. The output signal $S_o = i_p G$ is the input signal multiplied with the current to voltage gain G of the amplifier and the output noise $N_o = i_n G + N_a$ is the sum of the

input noise multiplied by the gain G and the noise generated in the amplifier N_a. The output signal to noise ratio then becomes:

$$\frac{S_o}{N_o} = \frac{S_i G}{N_i G + N_a}.$$

By inserting this into the expression for the noise figure we get

$$F_1 = 1 + \frac{N_a}{N_i G_1}.$$

By cascading two amplifiers the expression for the total noise figure of the circuit becomes:

$$F_{tot} = F_1 + \frac{F_2 - 1}{G_1},$$

where $F_2 = 1 + {}^{N_a}/_{G_2 N_i}$. From this expression we can se that the contribution from the first amplifier will dominate the total noise figure of the circuit, if we assume that the gain G_2 of the second amplifier is small compared to the gain G_1 in the first amplifier. This means that we can approximate the noise generated by the amplifier network to the contribution from the preamplifier.[61] As the primary source of noise in the amplifier is the Johnson noise we can define

$$N_a = V_{jn} = \sqrt{4kT_r R_{amp} \Delta f}. \tag{2.82}$$

The Johnson noise in the amplifier used in this project is generated in the feedback impedance which at a bandwidth of $10\,Hz$ is purely resistive with a value of $R_f = 100k\Omega$. If the temperature is $T_r = 293K$, and the Boltzmann constant $k = 1.38 \cdot 10^{-23} J/K$, equation 2.82 gives the mean squared value of $V_{jn} = 2 \cdot 10^{-7}\,V$.

2.5.9 Noise and error in data acquisition

In addition to the noise sources already mentioned, the data acquisition device will introduce error and noise. The primary task of a data acquisition device is to convert an analog voltage to a digital number. The limiting factor in analog to digital conversion is that while an analog signal can assume an infinite number of values between a given minimum and maximum value, the digital representation of this value can only assume a discrete value with a defined finite precision. The analog to digital converter used in this instrument has a resolution of 24 bits [62], making it able to represent $2^{24} - 1 = 16777215$ different values. When its measurement range is $20V$, the smallest possible voltage difference it can detect is $\Delta V_{daq} = {}^{20V}/_{2^{24}} \approx 1.2 \cdot 10^{-6} V$. If we consider how a binary number is represented,

this value corresponds to the value of the least significant bit. From equation 2.59 we can find the corresponding minimum detectable photocurrent as $\Delta I_{daq} = 1.2{\cdot}10^{-11}A$. This is 6 to 7 orders of magnitude less than the expected photocurrent at approximately $1 \cdot 10^{-4}\,A$.

Because of the minimum detectable voltage difference, the difference between the analog signal and its digitally assigned value will be a source of error. The process of assigning a digital value to a measured value is called quantization. A measured value will be quantized to the digital value to which it is nearest. The maximum value of this error will be half of the minimum detectable voltage difference[38]:

$$V_{qn} = \pm\frac{\Delta V_{daq}}{2} = \pm 6 \cdot 10^{-7} V.$$

As this error will occur randomly, due to the random properties of the photocurrent, it is often referred to as quantization noise. There will also be thermal noise and shot noise present in the data acquisition unit. This is not possible to calculate as the electrical schematics and magnitudes of components in the data acquisition device is unknown. We denote the sum of the quantization noise and the electronic noise as V_{adc}. We can measure the magnitude of this noise by short-circuiting the input channel and look at the standard deviation of the measured signal.

Without going into detail in the internal workings of the analog to digital converter, its voltage input to binary output can be represented by an ideal linear transfer function. Error sources inside the converter, such as the specific size of amplifier resistors, can make the slope of the real transfer function slightly different from the ideal case. The difference between the real and ideal transfer function represent a measurement error which is dependent on the input voltage. The contribution from this gain error is therefore given as a percentage of the measured value. [62]

The real transfer function of the converter may also be offset from the ideal transfer function with a fixed value, caused by temperature dependencies of the components in the converter. The magnitude of this error can be determined by measuring the output value of short-circuited channel and subtract this value from later readings. Changes in temperature will cause the offset value to drift by a given voltage to temperature factor. In this project the analog to digital converter is placed in room temperature and will not experience temperature changes.[62]

2.5.10 Total uncertainty

If we look at all the mentioned noise sources we can make a model of how they contribute to the overall uncertainty of the system. Figure 2.25 describes where in the measurement process the noise is introduced. The noise generated in the laser and photodetector are uncorrelated and independent and their combined value is given as i_n in equation 2.81. The output from the amplifier V_A is a function of the photocurrent and the gain of the amplifier, and adds a thermal noise term V_{jn}. The data acquisition device then adds quantization and electric noise V_{adc}. The output uncertainty σ_{tot} from the data acquisition device will then describe the total noise in the system.

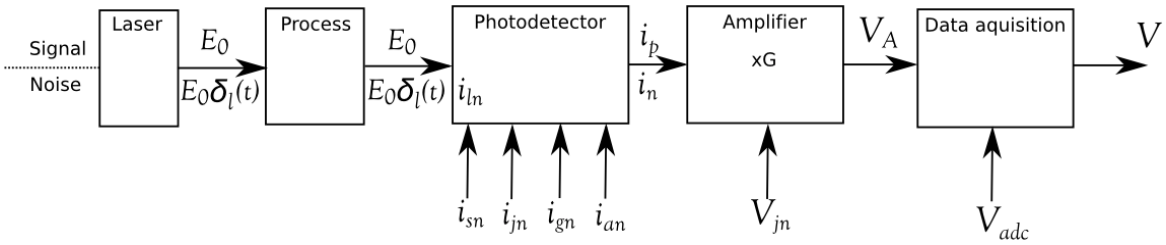

Figure 2.25: Model of the predicted noise sources in the instrument.

If we assume that the noise in the detector is gaussian with zero mean we can express the uncertainty of the noise as its root-mean-square value, as described in appendix C.

$$\sigma_{i_n} = \sqrt{\bar{i_n^2}}.$$

If we also assume that the thermal noise generated in the amplifier V_{jn} and the noise in the data acquisition device V_{adc} are gaussian, their standard deviations can be expressed in the same way as

$$\sigma_{V_{jn}} = \sqrt{\bar{V_{jn}^2}} = \sqrt{4kT_r R_{amp}\Delta f} \text{ and } \sigma_{V_{adc}} = \sqrt{\bar{V_{adc}^2}}.$$

The expression for the output voltage of the amplifier is

$$V_A = (i_p + i_n)G + V_{jn}.$$

The standard deviation of the amplifier output σ_{V_A} is given by the formula in appendix C. The standard deviation of the gain is considered to be zero. The expression for the measured voltage of the data acquisition device is:

$$V = V_A + V_{adc}.$$

We can then express the standard deviation of the measured voltage of the data acquisition device, which also is the total standard deviation as:

$$\sigma_{tot} = \sqrt{G^2 i_n^2 + \sigma_{V_{jn}}^2 + \sigma_{V_{adc}}^2}. \tag{2.83}$$

Chapter 3

Instrument design and experimental setup

This chapter describes the instrument which was created for this thesis. A detailed outline of the instrument will be given by presenting figures and arguments for the design choices.

3.1 Instrument setup

A sketch of the instruments physical construction and electrical connection is shown in figure 3.1. The electrical components in black are not drawn to scale. Details on the components described in the figure are listed in table 3.1. Figure 3.2 shows pictures of the important instrument components. The upper left picture shows the instrument container with the laser mounted and the detector bracket removed. The two other pictures show the two position detectors mounted in their brackets. The brackets fit perfectly into the instrument, to hinder detector movement. The material from which the instrument container is made is a transparent acrylic glass. The components are glued together with optical adhesives. We can see that the container is divided into two compartments, separated by a watertight wall in the middle. The wall consists of a plastic barrier and the prisms used in the optical path. The upper compartment is covered completely by acrylic glass walls. The sample is introduced through a rubber tube inserted in the bottom of the upper compartment by a water pump. The lower compartment is housing the electrical components of the instrument and is filled with air.

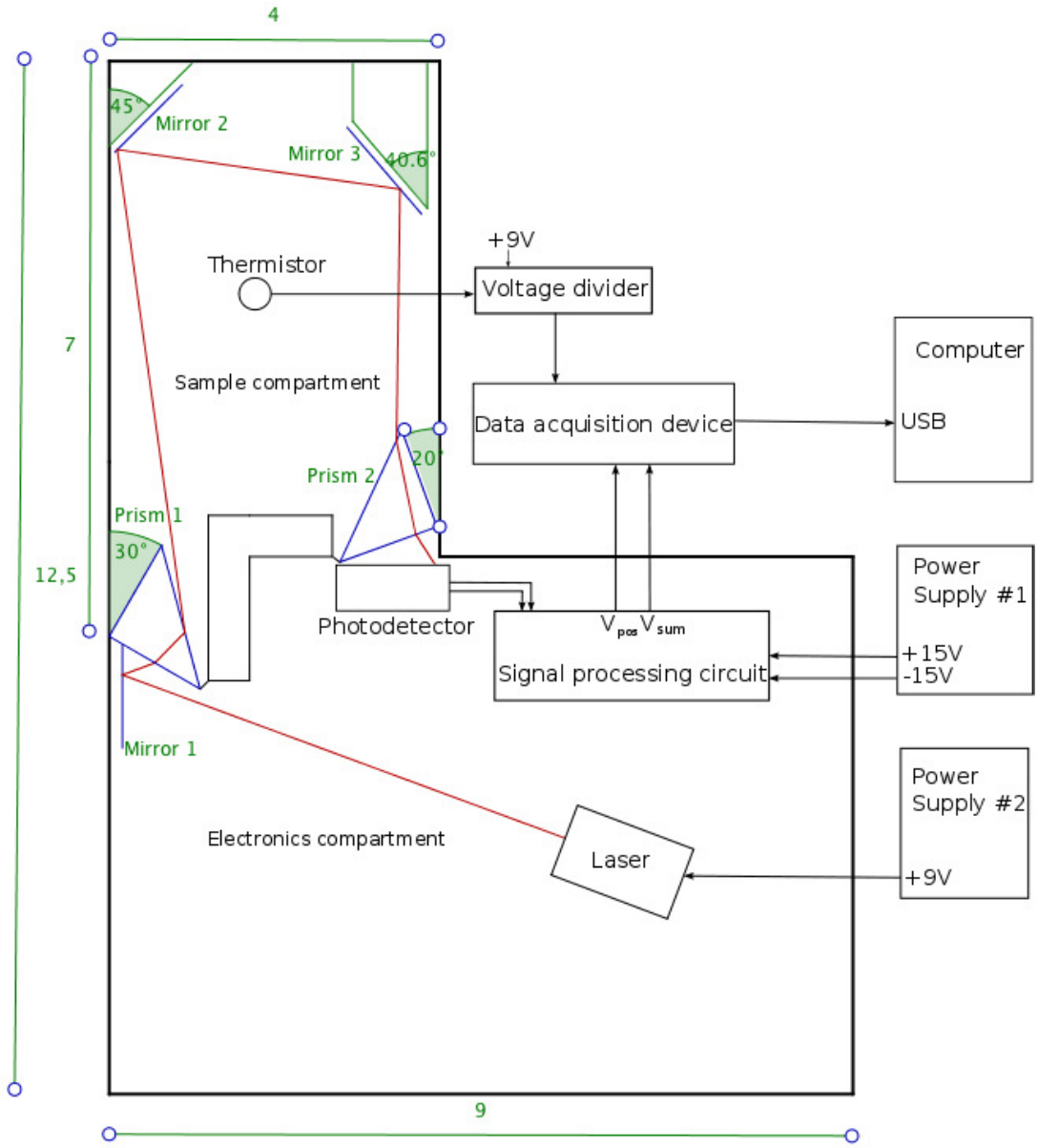

Figure 3.1: 2-D sketch of instrument with measures in cm. The height of the cabinet walls are $4\,cm$.

In the upper corners of the sample compartment there are placed mirrors to fold the beam. This makes it possible to achieve a long path length for the laser, which is imperative for proper sensitivity, while the size of the instrument is kept small. From the figure we can see that the size of the sample compartment is comparable to the design goal of a cylinder of length $86\,mm$ and diameter of $36\,mm$, resulting in a volume of $81\,cm^3$. Because of the prototype nature of the project, the electronics compartment has been made a lot bigger than necessary. This is done to be able to experiment with different types of lasers and photodetectors. The size of the cabinet is described in figure 3.1. The height

Component	Description	Vendor
Laser	Coherent VHK circular beam diode laser operating at $635\,nm$ with an output power of $0.95\,mW$.The beam diameter is $1mm$.	Edmund Optics
Position sensitive detector (PSD)	Hamamatsu S3932 Position sensitive detector. Responsivity $S \approx 0.4\,{}^{A}/_{W}$ at $635\,nm$, Minimum detectable displacement $0.3\,\mu m$.	Hamamatsu
Signal processing circuit for PSD	Hamamatsu C3683-01 Signal Processing Circuit	Hamamatsu
Quadrant cell photodiode	OSI Optoelectronics QD-50-6-18u-2SD quadrant cell photodiode with integrated amplifier circuit.	BFi Optilas
Data acquisition device	NI-USB 9239 data acquisition device. The resolution of its analog to digital converter is 24 bit. Its minimum sample frequency is $1.613\,kHz$.	National Instruments
Thermistor	B57500K0103A001 - $10\,k\Omega$ negative temperature coefficient thermistor with $\beta = 3795$	Elfa Elektronikk
Power supply #1	TTi EX354RD - Precision DC power supply with dual terminal output. Constant voltage up to 35 V.	Supplied by UoB
Power supply #2	TTi QL355P - High precision DC power supply with single terminal output. Constant voltage up to 35 V.	Supplied by UoB
Water pump	Manostat Vera Varistaltic pump	Supplied by UoB
Prism 1	The first prism is made of chemical vapor deposited Zinc-Selenide (ZnSe) with a refractive index of 2.58 at $635\,nm$. The legs are $12.5\,mm$.	Edmund Optics
Prism 2	The second prism is made of fine borosilicate crown glass (BK-7) with a refractive index of 1.51 at $635\,nm$. The legs are $12.5\,mm$.	Edmund Optics
Mirrors	The mirrors are first surface mirrors, as the light is reflected on the surface of the mirror. The surface accuracy λ of the mirrors are 4-6.	Edmund Optics
Data acquisition software	National Instruments Labview 8.0 is used to present the measurements and to generate data files.	National Instruments
Analysis software	Mathworks Matlab 2009 is used to analyze the measured data and generate figures presented in this thesis.	MathWorks

Table 3.1: Specifications of instrument components

of the cabinet is $4\,cm$. This is also much larger than necessary. The height of the cabinet could be reduced $1.25\,cm$ to still be able to fit the prisms and laser module. The overall volume of the entire instrument cabinet is $330\,cm^3$. With reduced height the volume would be $103\,cm^3$. The choice of geometry is a result of manual optimization through simulation. The simulations have been conducted using a simple dynamic raytracing tool called CarMetal [63]. This program has enabled the simulation of changing refractive index in the water sample and the resulting beam displacement on the photo detector surface. To achieve the optimal sensitivity of this setup, the lateral displacement of the laser beam incident on the detector surface must sweep the entire length of the detector active area as the refractive index changes from minimum to maximum value of the defined measurement range.

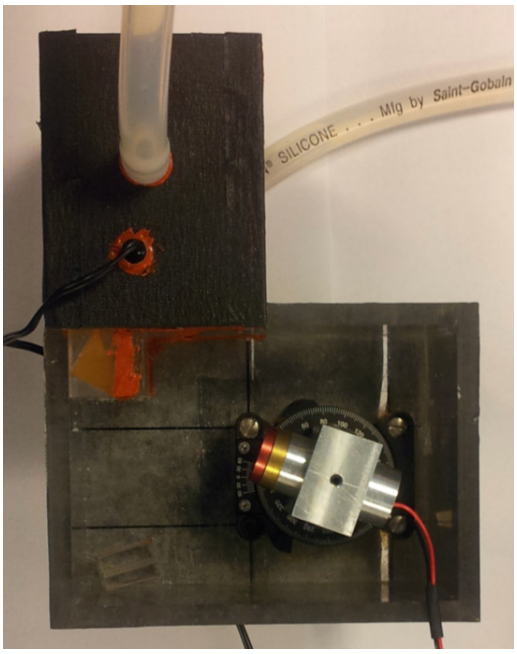

Instrument cabinet with laser mounted on rotational platform

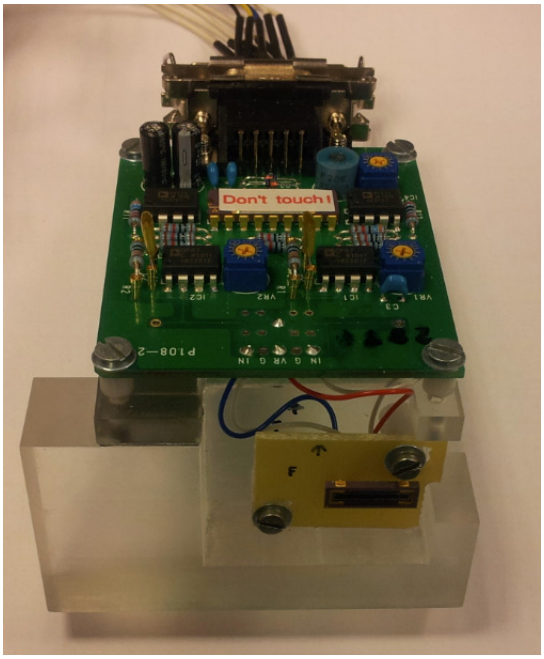

Position sensitive detector and amplifier circuit mounted on bracket

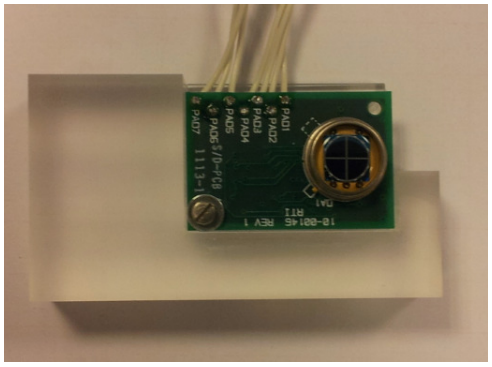

Quadrant cell detector mounted on bracket

Figure 3.2: Pictures from the experimental setup

3.2 Optimization of instrument geometry

The optimization process was complex, as several design choices influences the achieved refractive index sensitivity. All references to prisms and mirrors in this section refers to figure 3.1. The first and most important consideration is the incident angle of the laser beam on the prism-water interface of Prism 1. Snells law (equation 2.36) defines how the the transmitted angle is dependent on the incident angle and the ratio of the refractive index of the two substances.

$$\theta_t = arcsin\left[\frac{n_i}{n_t} sin(\theta_i)\right].$$

If we assume that $n_t < n_i$ and investigate this expression by plotting the value of the transmitted angle as a function of the incident angle we will see, as in figure 2.7, that the slope of the function is increasing as we approach the critical angle. This means that the transmitted angle will be more sensitive to a small change in refractive index the closer we get to the critical angle. This fact can be used to our advantage, as the instrument will be more sensitive if the incident angle is approaching the critical angle, at the cost of loss of linearity.

When approaching the critical angle we must consider the reflected and transmitted power as dictated by the reflectance and transmittance, based on the Fresnel coefficients described in equations 2.40 and 2.41. The transmittance and reflectance coefficients for the parallel polarization are $T_p = 1 - |r_p|^2$ and $R_p = |r_p|^2$, and for the perpendicular polarization $T_s = 1 - |r_s|^2$ and $R_s = |r_s|^2$ as derived in section 2.1.6. We can plot these values as functions of the incident angle as shown in figure 2.6. The critical angle θ_c is also shown in the figure. We see that the transmitted power drops fast as the incident angle increases towards the critical angle. If we want the highest possible change in transmitted angle when the refractive index changes, figure 2.7 tells us to chose an incident angle just less than the critical angle. But if we input the chosen angle into figure 2.6, we see that only a small fraction of the light will be transmitted. This might not be a problem if the incident laser power is high, but if a less powerful laser is chosen the transmittance coefficient must be considered. As this instrument will be assembled by hand, which may lead to slight inaccuracies in the placement of the prisms, it would be wise to err on the side of caution regarding the incident angle.

If the incident angle is 30.7^o, we will experience the increased change in transmitted angle to change in refractive index while having a transmittance co-

efficient of about 0.7 if unpolarized light is assumed. We will also have some room for error in the placement of the prism. As one can see from figure 3.1, the same considerations must be made at the interface of the second prism. The complete power record with loss calculations for every interface and for the absorption in the water sample will be presented later in this chapter.

The next phase of the design is to place the first-surface mirrors in the upper part of the sample compartment. While placing Mirror 2, an angle of 45^o was chosen to reflect the laser beam towards the second mirror. The only consideration on the placement of this mirror is that the laser beam should be reflected as close to the left edge of the mirror as possible when the refractive index of the sample is on the lowest level of the measurement range. This means that the incident angle on the first prism-water interface is optimized. As the refractive index of the sample is increasing, the transmitted angle of the first prism-water interface will decrease and the laser beam position on Mirror 2 will move towards the right.

The position of Mirror 3 is chosen to reflect the beam from Mirror 2 towards Prism 2, so that the incident angle on the water-prism interface of Prism 2 is optimal. The exact position was determined by manual optimization in the simulation program and must be seen in conjunction with the placement of Prism 2. Prism 2 is angled at 20^o away from the side wall of the container to achieve the wanted transmitted beam out of Prism 2. As the position of laser incidence on the prism is dynamic, unlike at the prism-water interface of Prism 1, the design must accept laser incidence along the entire length of hypotenuse of Prism 2. The projection of the hypotenuse of Prism 2 seen from Mirror 2 will be dependent on the angle the prism makes with the side wall. If the angle is too big, the projection of the hypotenuse seen from Mirror 2 will be to small to accept the variations of the laser beam position dictated by the transmitted angle of Prism 1. If this angle is too small, the transmitted angle at the prism-air interface out of Prism 2 will be too small and it will not be possible for the laser to swipe the entire length of the PSD active area in the measurement range. The choice of 20^o for this angle is a compromise between these two considerations. This leaves the placement of the photodetector where the only consideration is to capture the laser beam from its leftmost position to its rightmost position.

The expression relating the lateral displacement of the laser beam to the refractive index is based on repeated applications of Snells law and is very complex. Its theoretical derivation is presented in Appendix A. The resulting

expression is given as:

$$n = 1.344 - 0.0115 \cdot X + 0.9618 \cdot 10^{-3} \cdot X^2 + 0.1293 \cdot 10^{-3} X^3 + 3.823 \cdot 10^{-6} X^4, \quad (3.1)$$

where $0 \leq X \leq 1.2$ in centimeters. It is apparent that since the instrument is hand made, it will be impossible to replicate the exact angles and lengths presented in the derivation of the expression in the construction process. This will cause the experimental results to deviate slightly from the computer simulated results. We can express the sensitivity of the refractive index to a small change in displacement by differentiating the expression

$$\frac{dn}{dX} = -0.0115 + 1.9236 \cdot 10^{-3} \cdot X + 0.3879 \cdot 10^{-3} X^2 + 1.5292 \cdot 10^{-5} X^3. \quad (3.2)$$

From equation 3.2 we can conclude that the instrument sensitivity is dependent on the exact position of the laser beam. The output value of the expression varies almost linearly from -0.0115 at $X = 0\,cm$ to -0.0085 when $X = 1.2\,cm$. The minimum detectable displacement of the photodetector is given as $\Delta X_{min} = 0.3\mu m = 0.3 \cdot 10^{-4} cm$. This means that the theoretical minimum detectable change in the refractive index will be given as:

$$\Delta n_{min} = \frac{dn}{dX} \cdot \Delta X_{min} \in \left[2.5 \cdot 10^{-7},\, 3.45 \cdot 10^{-7}\right]. \quad (3.3)$$

If we compare this to the postulated sensitivity of the refractometer from section 2.3.1, we see that the instrument has a sensitivity in the same order of magnitude as the ideal instrument described in section 2.3.1, as well as similar refractometric instruments proposed by others.[6]

3.3 Optical power loss

The power output from the laser will be significantly reduced before it reaches the detector. The attenuation of the beam in the prisms (2.4.4) and water (2.4.5) as well as the reflection of a portion of the power at a prism-water interface will cause the power at the detector to be a fraction of the laser output power. To give a total account of the losses we start by considering the attenuation in the $ZnSe$ prism. The output power of the laser is given as $P_0 = 0.95\,mW$. From equation 2.69 we get the remaining power after passing through a substance of attenuation coefficient α and length l. The empirical attenuation coefficient of Zinc Selenide at a wavelength of $0.635\,\mu m$ is given as a log base 10 value $\alpha_{ZnSe} \approx 1.95\,cm^{-1}$.[64]

We can find the length in which the laser beam will propagate through the $ZnSe$ prism by looking at the computer simulation of the instrument. The length is found to be $l_{ZnSe} = 0.5\,cm$. The remaining power after passing through the prism is then

$$P_{prism} = 0.10\,mW.$$

We can also consider the approximate temperature change in the prism caused by the attenuation. If we assume that all of the light is absorbed and that the laser beam still is of diameter $1\,mm$ the power absorbed by the prism is

$$P_{absorbed} = (P_0 - P_{prism}) = 8.5 \cdot 10^{-4} \frac{J}{s}.$$

In equation 2.68 we found that $\Delta T_{prism} = \frac{\Delta Q}{m_{ZnSe} c_{ZnSe}}$. This is not the full truth, as the conduction of heat into and out of the prism is governed by the heat conduction equation and Newtons law of cooling, because of its interface with the sample media and surrounding instrument cabinet. The point is merely to illustrate that the prism will be heated.

We continue the power loss calculations by considering the transmittance of the prism-water interface of the first prism. We established in section 3.2 that the transmittance of the prism water interface is $T_{prism} = 0.7$ under the given conditions of incident angle and refractive indices. If we assume that the area occupied by the laser beam remains unchanged on both sides of the interface, the transmitted intensity from the prism-water interface is:

$$P_{prism_T} = P_{prism} \cdot T_{prism} = 0.073\,mW. \tag{3.4}$$

The attenuation in the water sample is found by the use of equation 2.69. The attenuation coefficient of seawater is reported by Ref. [65] to be $\alpha_{sw} = 0.003\,cm^{-1}$ when the salinity is $35\,psu$ and wavelength is $635\,\mu m$. The path length of the laser beam through the water sample can be found in the computer simulation to be $l_{sw} \approx 13\,cm$. The data sheet from the producer state that BK-7 has an attenuation coefficient very close to zero for the entire visible spectrum, and its contribution to attenuation is therefore neglected. [43] The incident angle on the water-prism interface is far from the critical angle an the transmittance is therefore close to unity. If we assume that the laser spot is still circular with a diameter of $1mm$ the total incident power on the sensor will be:

$$P_{detector} \approx 7 \cdot 10^{-5} W. \tag{3.5}$$

From equation 2.48, this corresponds to a photocurrent of $i_p = 2.8 \cdot 10^{-5} A$ when the responsivity is $S = 0.4\,{}^{A}/_{W}$.

3.4 Data acquisition software

The data acquisition and presentation software used in this project is the National Instruments LabView 8.4 suite. LabView is a graphical development environment widely used in both industrial and research related instrument and measurement applications. It can be used for a lot of different applications, and it appeals to both beginners and experienced developers. It has several built in functions and easily interface to several instrument communication standards out of the box. As the data acquisition device is a product of the same company, the setup of this device is done automatically.

The LabView program that has been developed for this project reads the input signals from the data acquisition device at a given sample frequency and presents them on screen. The input signal voltage is converted to describe the lateral displacement in millimeters by using equation 2.60. The program will also store the data to a file. Screenshots of the program block diagrams are included in appendix D.

3.5 Sample frequency

Before we can start the actual experiment we need to determine a critical measurement variable yet to be properly discussed, namely the sample frequency. We have established that the refractive index is changing very slowly, at least when the sensor is assumed stationary. We know from Nyquists sampling theorem that to avoid aliasing, the sample rate must be at least twice the bandwidth of the signal. [38] As the signal is very close to a DC value for a stationary measurement, we could set the sample rate at for instance $f_s = 10Hz$ or less. If we assume that the sensor must also be able to perform measurements while being moved vertically up or down through the water, we give the refractive index a frequency, assuming that the refractive index actually varies with depth. If we want to measure this at a given vertical speed v_v, and we want N_v measurements

per every D_v meter depth we can express this as:

$$f_s = \frac{N_v v_v}{D_v}.$$

If we assign typical values to this expression where $v_v = 10^m/_s$, $N_v = 100$ and $D_v = 10m$ we get a sample frequency $f_s = 100Hz$.

As was shown in equations 2.81, several noise sources are proportional to the bandwidth. This calls for an infinitely low sample rate to eliminate them completely. This is of course not possible, as the signal would be lost as well. A second consideration is that the cutoff frequency of the preamplifier in the signal processing circuit, as shown in figure 2.15, is $1.6kHz$. A third consideration is the minimum sample rate of the data acquisition device, given as $f_s = 1.613kHz$. This is not optimal as the noise power contribution from the bandwidth dependent noise sources will be much larger than it has to be. This is solved by using a digital low pass filter in the LabView program. We can define the cutoff frequency to $10Hz$ and thereby reduce the effect of the bandwidth dependent noise to a minimum.

Chapter 4

Experimental results

This chapter presents the experiments conducted to describe the instruments characteristics and its performance. The experimental results are presented and briefly commented in this chapter, and then discussed thoroughly in the next chapter.

4.1 Measurement of noise sources

To precisely describe the instrument we want to determine the contribution of noise from the sources described in section 2.5. Some noise sources have already been quantified theoretically. This section will present different custom instrument setups designed to determine the magnitude of the other noise sources. The error contribution will be measured in reverse order in which they occur in the instrument, starting with the data acquisition device. This is done to quantify and possibly eliminate the error before the next component in the chain is examined. The definitions of the statistical measures used to describe the experimental results, the mean and the standard deviation, are given in appendix C.

4.1.1 Data acquisition error

To determine the magnitude of the data acquisition noise and error we start by by connecting the data acquisition device directly to a power supply. We then set the power supply output voltage to $10V$ and $-10V$. If the measured values

differ from the set values, we simply multiply all subsequent measurements by the ratio between the set and the measured value. The offset error is determined by short-circuiting the positive and negative terminal of one channel on the data acquisition device. If the average value is different from 0, it will simply be subtracted from all subsequent measurements. The standard deviation of this measurement will determine the contribution of electronic and quantization noise $\sigma_{V_{adc}}$. The data acquisition error and its statistical parameters were calculated from 60000 samples taken in batches of 1000 a time over a time period of 1 hour. The sampling rate was $1.613\,kHz$ and a digital filter of $10\,Hz$ was applied in the software. The measurement was conducted directly after the start up of the device. The mean value and its standard deviation is shown in figure 4.1.

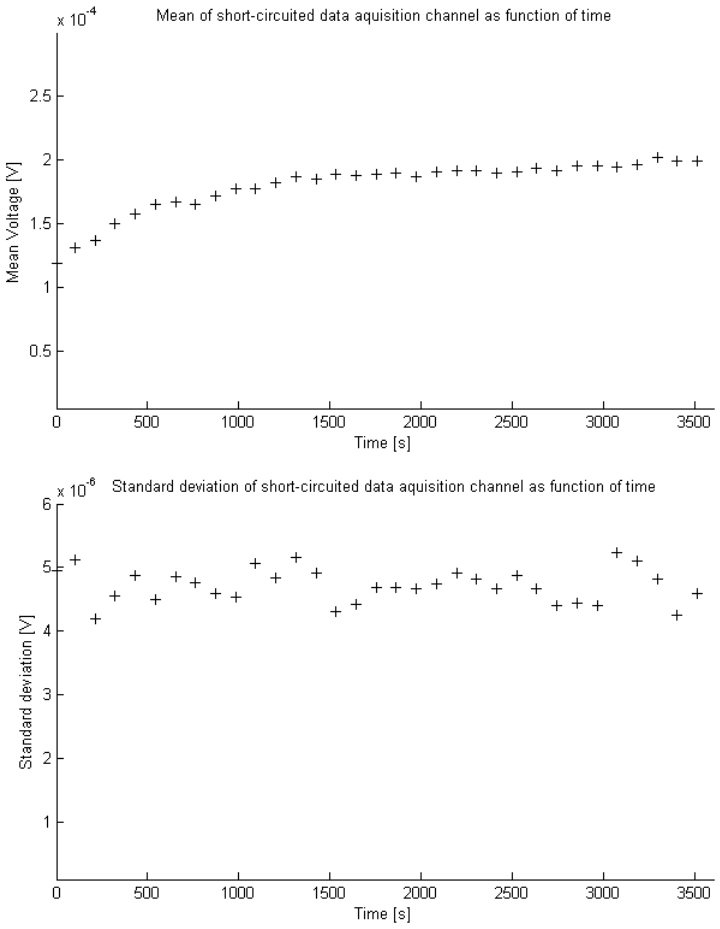

Figure 4.1: Measured data acquisition mean voltage and its standard deviation for the last 1000 values

4.1.2 Detector noise

The detector noise was measured in a completely dark environment. The statistical parameters was calculated from 60000 samples taken in batches of 1000 a

time over a time period of 1 hour. The sampling rate was $1.613\,kHz$ and a digital filter of $10\,Hz$ was applied in the software. The mean value and its standard deviation is shown in figure 4.2.

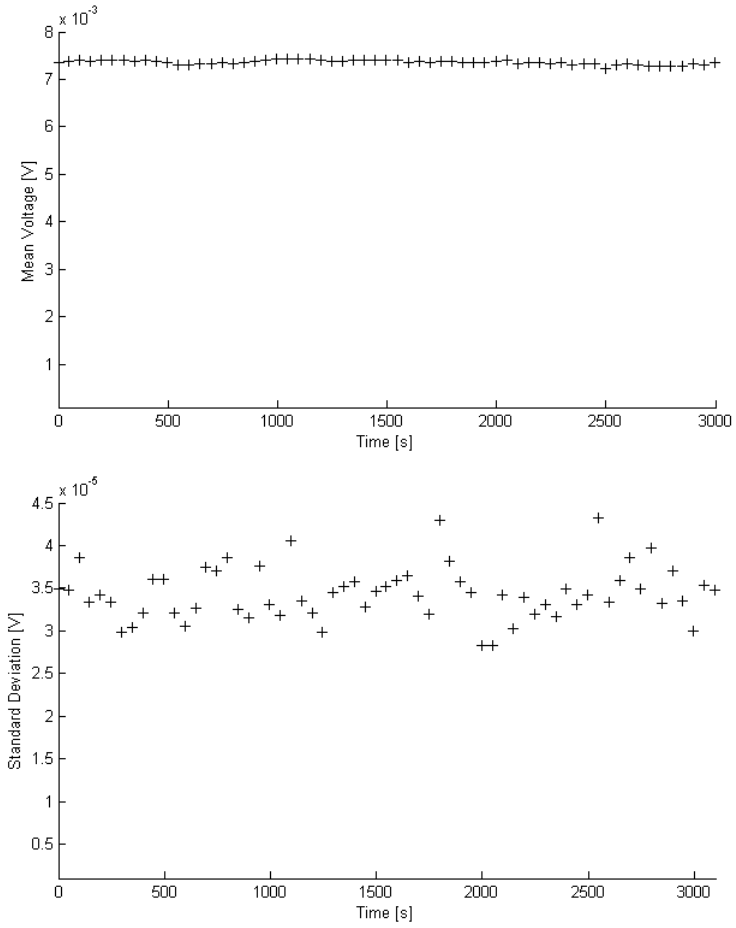

Figure 4.2: Measured dark detector mean voltage and its standard deviation for the last 1000 values

4.1.3 Laser noise

The laser noise current i_{ln} will be the last noise source to be quantified as we must determine all other noise sources and subtract them from the measurement data. This is because all noise in the detector will influence the measurement of the laser power. We do this by placing the detector and the laser outside the measurement chamber, but enclosed to avoid ambient light, and measure the sum voltage output of the detector driver circuit. The values will be measured for 1 hour and the mean value and standard deviation will be used to present the noise.

We also want to measure the pointing stability. This is done in the

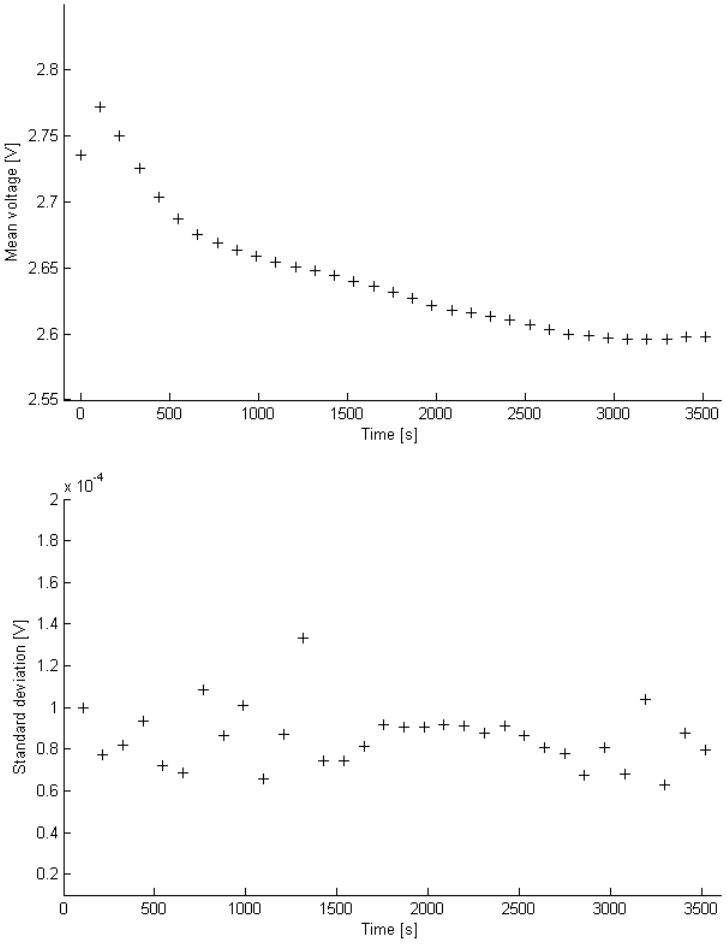

Figure 4.3: Measured mean SUM voltage and its standard deviation for last 1000 values

same measurement as the one described above, but the measured value is the position voltage output. We place the laser at the same distance away from the sensor as it would be if placed inside the chamber. The magnitude of the position standard deviation should be directly comparable to the standard deviation of the measured beam position in the actual experiments. The statistical parameters were calculated from 60000 samples taken in batches of 1000 a time over a time period of 1 hour. The sampling rate was $1.613\,kHz$ and a digital filter of $10\,Hz$ was applied in the software. The mean value of the SUM voltage and its standard deviation over the last 1000 samples is shown in figure 4.3. The means value of the position voltage and its standard deviations is shown in figure 4.4. The laser and detector were then mounted inside the instrument container and the position voltage standard deviation was measured with a pure water sample in the sample compartment. The result is shown in figure 4.5.

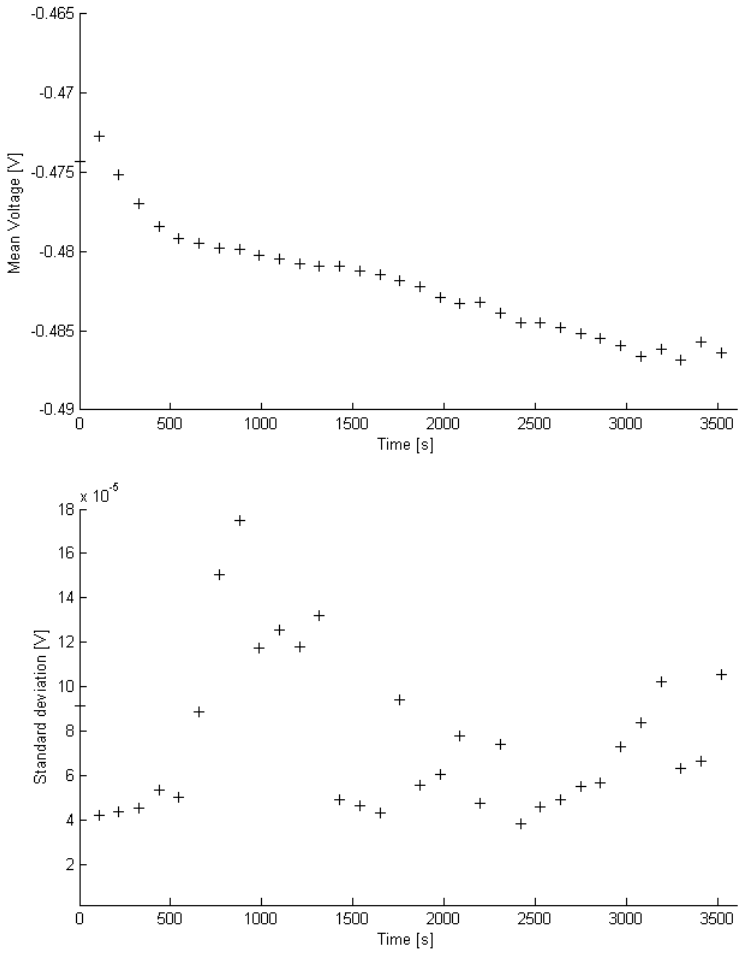

Figure 4.4: Measured mean laser position voltage and its standard deviation for the last 1000 values

Figure 4.3 and 4.4 illustrates a temporal variation of the laser power fluctuations and the laser position fluctuations. The mean SUM voltage and

the mean position voltage behave in the same deterministic manner, having a top at approximately 100 s and then decreasing almost linearly from 500 s to 1 hour. Equation 2.56 shows that the position voltage is normalized to account for changes in the total photocurrent. This fact should make the position voltage independent of the fluctuations in the SUM voltage, but it is clearly visible that the shape of the two plots are similar. We do however see that the variations are about one order of magnitude less in the position voltage plot than in the SUM voltage plot. To explain the initial peak and the following decline it is reasonable to relate it to a thermal process in the detector. Both the detector and the laser had heated properly before the experiment. Thus, it is logical to assume that the peak and decline is caused by the laser beam heating the detector, causing the detector temperature to increase and its characteristics to change until reaching thermal equilibrium. Ideally the measurement should have been conducted over a longer time interval to find out if the value finally stabilizes.

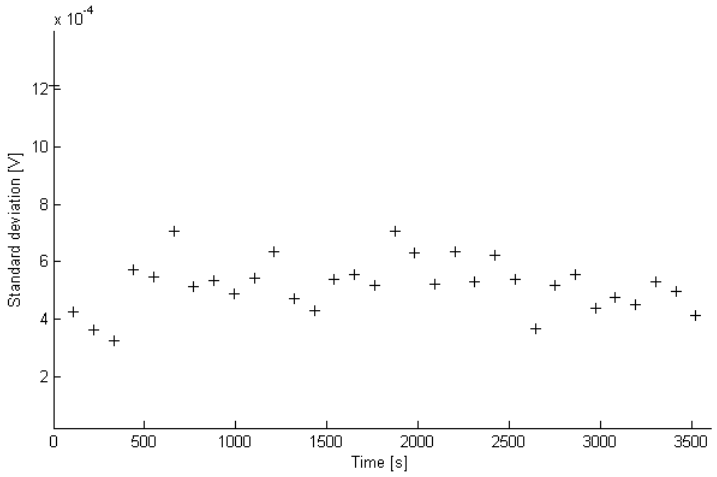

Figure 4.5: Measured laser position voltage standard deviation for water sample

We can present the data from figure 4.5 in a different way. Instead of plotting the standard deviation as a function of time, we plot the deviation of each of the 60000 samples to the mean value in a histogram. Figure 4.6 shows this with a gaussian curve fit, described in appendix C, of standard deviation $\sigma = 6.2 \cdot 10^{-4}\, mm$ and a mean of zero superimposed. We see that a gaussian distribution describes the noise in the instrument fairly well.

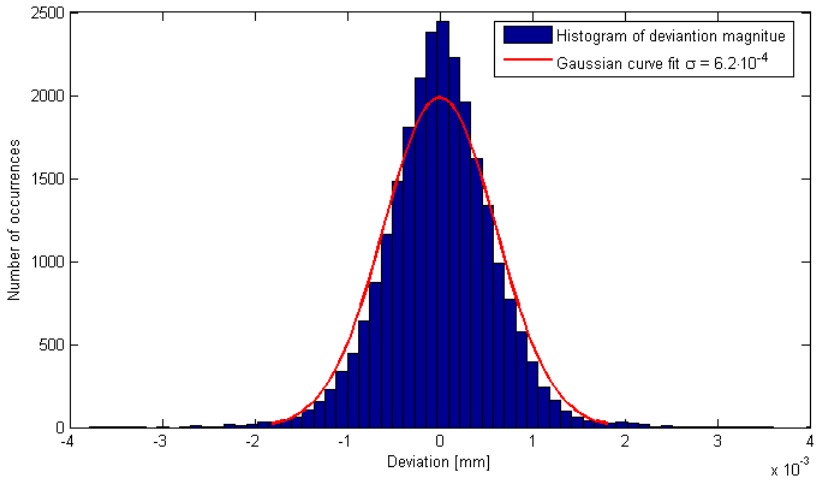

Figure 4.6: Histogram showing number distribution of laser position deviation magnitude with a superimposed gaussian curve with zero mean.

In the presentation of the quadrant cell photodiode we assume that the laser spot remains circular after passing through the measurement chamber. This is verified by measuring the laser beam size and intensity with a Thor Labs BC 106 VIS beam profiler camera. The camera software produces snapshots pictures of the laser beam. Figure 4.7 shows the snapshot picture of the laser beam after passing through the sample chamber. The color of the spot defines the power distribution where red is the highest and black is lowest level of intensity. The scale of the figure is in μm. The yellow circular overlay gives an indication of how circular the beam is. From the picture we see that the intensity is unevenly distributed inside the circle. The radius of the yellow overlay is measured to be $0.38\,mm$.

It is also interesting to measure the exact power of the laser before and after it passes through the measurement chamber. This is done by using a Thor Labs PM 100D power meter. The power of the laser beam before entering the measurement chamber was found to be $P_0 = 1.123\,mW$. After the beam had passed through a pure water sample in the measurement chamber the power was $P_{detector} = 0.210\,mW$.

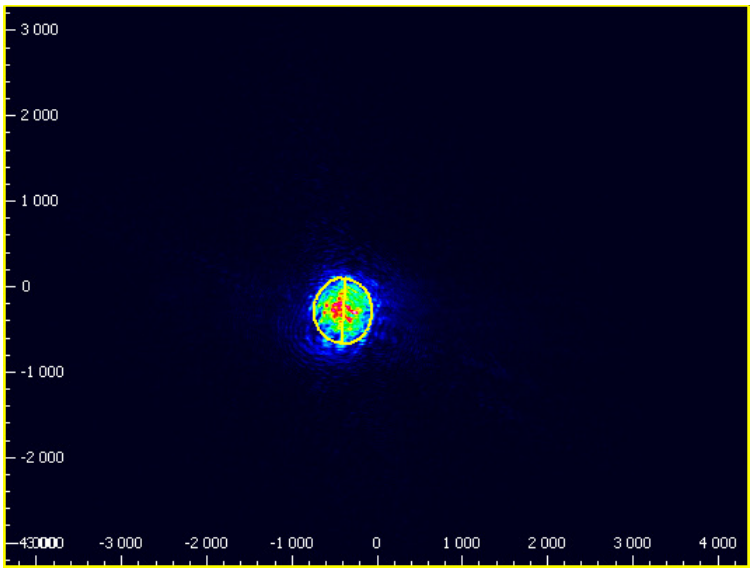

Figure 4.7: Picture of laser beam after passing through instrument. Scale of figure in μm

4.2 Thermistor Calibration

The thermistor was calibrated by exposing it to water of different temperature and measure the output voltage of the thermistor circuit, while at the same time manually log the temperature read by a thermistor probe on a Hanna Instruments 2210 pH meter. The values where then put in a plot and the MATLAB curve fit function was used to derive the constants K and β in the expression for the resistance of a negative temperature coefficient thermistor, given as $R_T = Ke^{\frac{\beta}{T}}$ where T is the temperature in Kelvin. The resulting expression is given as

$$R_T = 0.0289e^{\frac{3795}{T}} .$$

As the temperature was read manually this expression can not be considered to be accurate, but for the purpose of this project it is sufficient as no major temperature changes will be experienced.

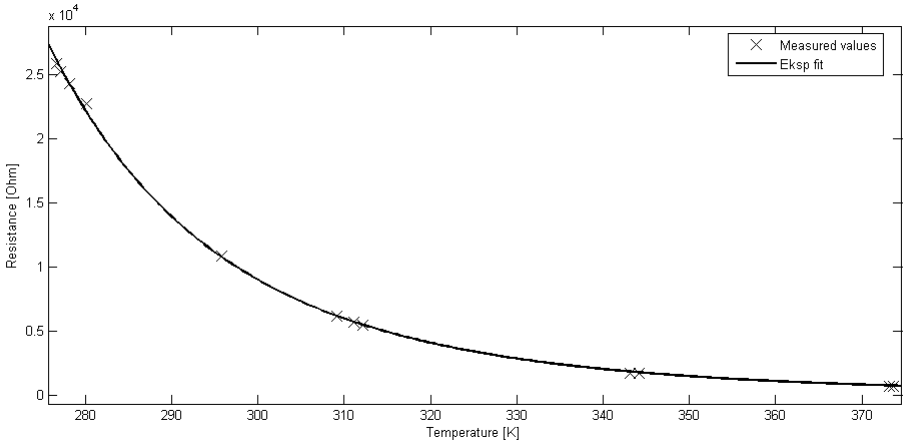

Figure 4.8: Calibration curve fit for NTC Thermistor

4.3 Results from Position Sensitive Device

The aim of the experimental part of the thesis is to determine if the instrument performs according to the predictions made by the computer simulation described in section A and to evaluate the instruments accuracy. The experiments are performed on the samples described in section 2.4.5. All the samples are of known refractive index, through equations 2.70 and 2.74.

In total, four measurements will be performed on both the seawater and $NaCl$ solution sample sets. Two of these experiments will be conducted on one day with the same ambient conditions to measure the instruments ability to produce repeatable results. It will also determine if any hysteresis is present by first measuring the samples in the order of increasing salinity and then decreasing salinity. The series are labeled 1 to 4 for both seawater and $NaCl$ solution. Series 1 and 3 are performed on increasing sample salinity, while series 2 and 4 are performed on decreasing sample salinity. Then the instrument will be partly disassembled and put together again, and two tests will be performed the next day. The purpose of this is to measure the instruments ability to reproduce the results under slightly different conditions.

The process of conducting an experiment involves some preparation. All parts of the instrument must be given time to warm up and reach a state of

thermal equilibrium before any measurements are taken. This is estimated to be approximately 20 minutes. Then a pure water sample is placed in the measurement chamber and the instrument is prepared by slightly adjusting the laser angle to achieve a rightmost possible reading from the position sensitive photodetector. The instrument is now ready to measure the remaining samples.

The actual experiment is done by placing the sample in the measurement chamber and start the measurement in the presentation program. The number of measurements per water sample is chosen to 1000. When the measurement is done, the liquid sample is removed and the a new liquid sample is pumped into in the chamber. This process is repeated until all the samples have been measured. The post processing of the data is done by finding the mean position displacement of the 1000 measured values along with its standard deviation, corresponding to a given salinity or salt concentration.

We start be presenting the data from the measurements of the seawater sample set and then present the data from the sodium chloride solution sample set. The results and trends will be commented and discussed briefly in the text. Observe that the units on the axis are different on the seawater samples [psu] and $NaCl$ solutions samples [$g/100g$].

4.3.1 Seawater samples

The data from the four measurement series conducted on the seawater sample set are shown in figure 4.9. The figure shows the displacement of the laser beam for each series and for each sample salinity. The length is defined as the distance from the leftmost part of the detector active area. The standard deviation of each point on the figure is small compared to the range of the data, and they are therefore presented in figure 4.10. The first observation we can make is that a salinity input range of $\Delta S_{sea} = 36.2\,psu$, results in a displacement output range of $8.4 - 2.5 = 5.9\,mm$. The ideal input range is $0 - 40\,psu$. The ideal output range is $10\,mm$, as discussed in section 2.4.1. If we extrapolate the data points in figure 4.9 linearly, the approximate reading from a $40\,psu$ sample would be $2\,mm$, extending the output range to $6.4\,mm$. If we compare this to the ideal output range we see that the instrument resolution is approximately 64 % of the ideal case described in the computer simulation.

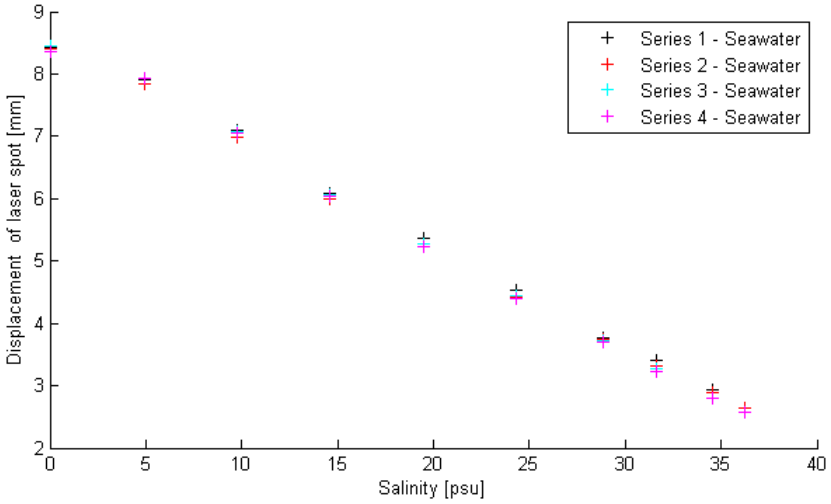

Figure 4.9: Measured displacement of laser spot versus salinity of seawater samples.

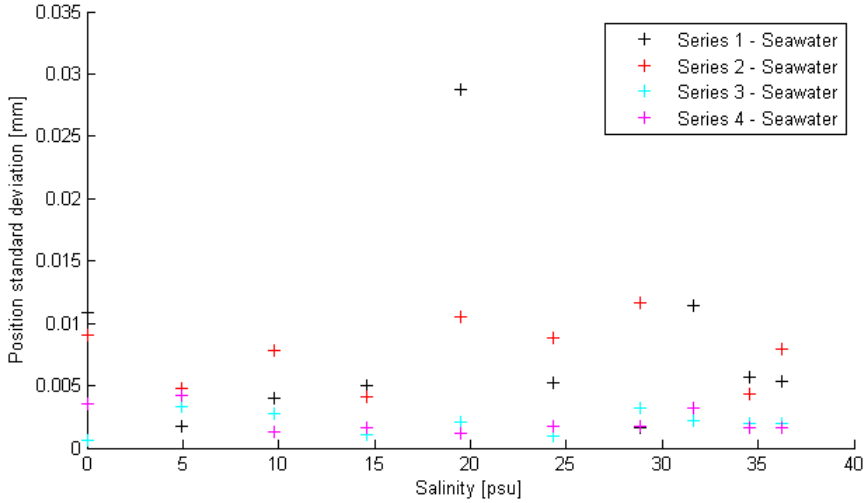

Figure 4.10: Standard deviation of measured values in figure 4.9.

4.3.2 Sodium chloride solution

The data from the four measurement series conducted on the sodium chloride solution sample set is shown in figure 4.11. The standard deviation of the measured data are presented in figure 4.12. During the experiments on the last two measurement series, two user error occurred. In series 3, the $2.5\,{}^{g}/_{100g}$ sample was contaminated with pure water, and in series 4, the same thing happened with the $2.0\,{}^{g}/_{100g}$ sample. The results from these two instances have been omitted in the presentation. We observe a concentration input range of $\Delta S_{NaCl} = 4\,{}^{g}/_{100g}$

resulting in a displacement output range of approximately $8.5 - 2.2 = 6.3\,mm$. This is almost the same as for the seawater data.

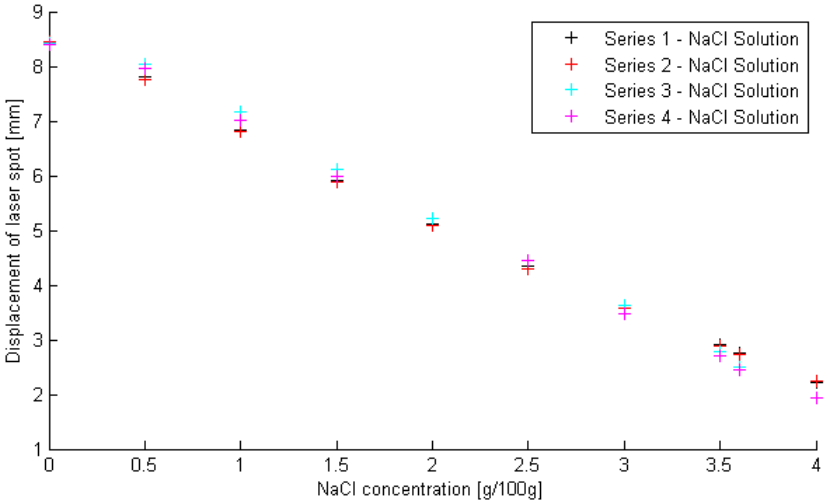

Figure 4.11: Measured displacement of laser spot versus concentration of sodium chloride solution samples.

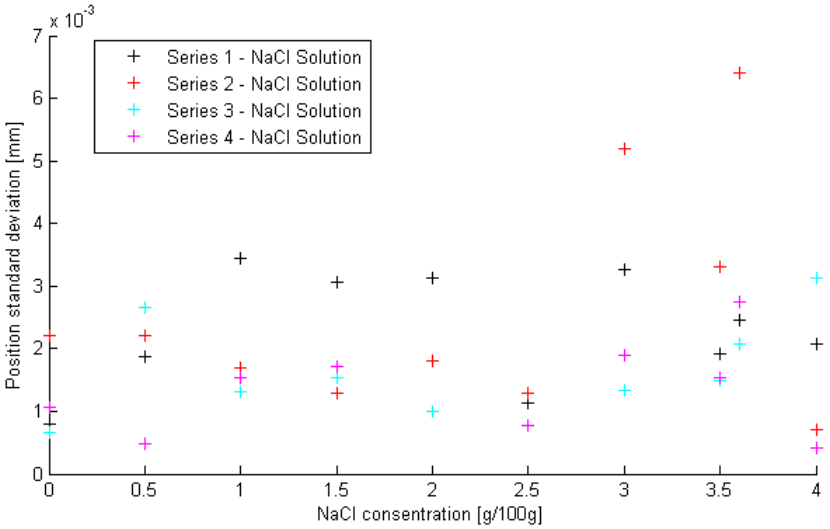

Figure 4.12: Standard deviation of measured values in figure 4.11.

4.4 Results from quadrant cell photodiode

The experiment on the quadrant cell detector was performed in a simplified manner compared to the experiments on the position sensitive detector. A new set of $NaCl$ solution samples where used, as the measurement range of the quadrant cell detector is $1\,mm$. The new sample set consists of 6 samples with concentration

from 1 to 1.5 $g/100g$ to achieve a sufficient number of data points to evaluate the detector. The experiment was conducted two times. The first time with increasing salt concentration, then directly afterwards with decreasing salt concentration. The result is shown in figure 4.13.

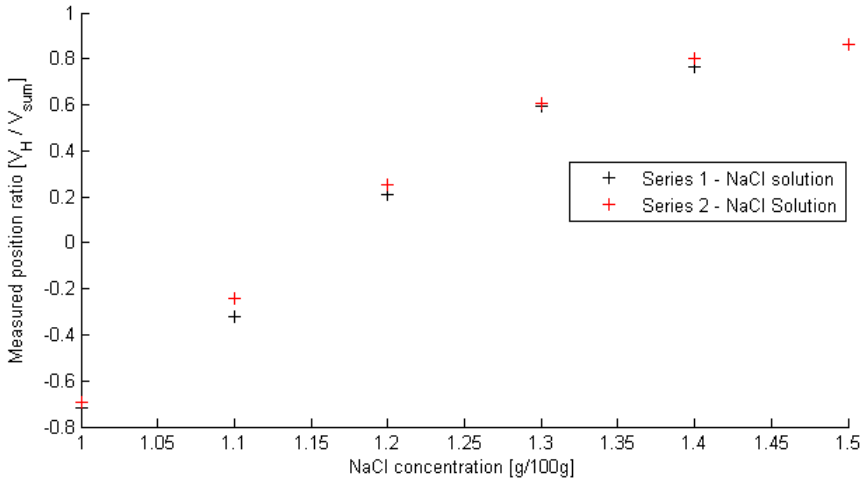

Figure 4.13: Measured position voltage ratio versus concentration of sodium chloride solution samples.

Chapter 5

Discussion and Conclusion

This chapter will discuss the results of the experiment. We start by discussing the measured and calculated noise in the instrument. Further we look at the data from the position sensitive detector, determining the overall measurement uncertainty and the achieved accuracy of the instrument. Does the computer simulation actually predicts the measured values? The results from the quadrant cell diode are discussed in the same manner. We then discuss the impact of biological fouling on the instrument. This topic was not investigated experimentally but is of major importance for an instrument designed to operate *in-situ*. What possible improvements and further work can enhance the performance of the instrument? Finally the conclusion assess how the specific goals of the thesis have been fulfilled.

5.1 Noise

5.1.1 Data acquisition noise

The magnitude of the data acquisition noise is as presented in table 5.1. We see from figure 4.1 that the steady increase of the mean value is caused by the fact that the sensor was cold at the start of the measurement. The mean offset value in table 5.1 is therefore taken from the last 1500 s of the series. The standard deviation σ_{adc} based on 1000 samples is fairly stable.

Error type	Magnitude
Gain error at $\pm 10V$ input	0.1 %
Mean offset error short circuited terminals	$1.9 \cdot 10^{-4}\, V$
Maximum standard deviation short circuited terminals σ_{adc}	$7.1 \cdot 10^{-6}\, V$

Table 5.1: Measured data acquisition error and noise

5.1.2 Detector noise

The mean measured voltage $\bar{V}_{dark} = 7.35 \cdot 10^{-3}\, V$ and its standard deviation σ_{dark} experienced little time dependency and were stable through the entire measurement. To evaluate the contribution from each noise source we must first look at equation 2.81. As no light is incident on the detector we can neglect the contribution from i_{sn}, i_{ln} and i_{gn}. This makes the resulting noise current $i_n = \sqrt{i_{jn}^2 + i_{an}^2}$. We then insert this into equation 2.83 and get the expression

$$\sigma_{dark} = \sqrt{G^2(i_{jn}^2 + i_{an}^2) + \sigma_{V_{jn}}^2 + \sigma_{V_{adc}}^2}.$$

The expression can be turned around to find the ambient noise current i_{an} based on the already measured or calculated values:

$$i_{an} = \sqrt{\frac{\sigma_{dark}^2 - \sigma_{V_{jn}}^2 - \sigma_{V_{adc}}^2}{G^2} - i_{jn}^2}.$$

The input values and result for the equation are listed in table 5.2. The table shows that the contribution from ambient noise and leakage current accounts for approximately $64\mu V$. It is highly unlikely that it is caused by ambient noise since the detector was completely dark during the measurement. As the other possible sources of noise are already determined, this noise most likely originates in the detector or its signal processing circuit. Its exact origin is most likely related to the signal processing circuit, as the derived equation for the noise voltage in the amplifier network is a simple approximation and the value has not been determined experimentally.

Noise type	Magnitude
Maximum measured dark detector voltage standard deviation σ_{dark}	$6.45 \cdot 10^{-5}\, V$
Measured data acquisition standard deviation $\sigma_{V_{adc}}$	$7.1 \cdot 10^{-6}\, V$
Calculated Johnson noise standard deviation from detector i_{jn}	$1.8 \cdot 10^{-12}\, A$
Calculated amplifier noise standard deviation $\sigma_{V_{jn}}$	$2 \cdot 10^{-7}\, V$
= Ambient and leakage noise current i_{an}	$6.42 \cdot 10^{-10}\, A$

Table 5.2: Measured detector noise

5.1.3 Laser noise

Figure 4.3 showed that the standard deviation over the last 1000 samples of the SUM voltage σ_{sum} was stable. From the histogram in figure 4.6 we can conclude that the total noise in the instrument can be treated as gaussian noise. This means that we can rightfully assume that all the noise currents are gaussian as well. We can continue the investigation on the sources of noise in the circuit by again looking at equation 2.81. We have determined all of the noise sources except for the laser noise i_{ln}. We can turn equation 2.83 around to express i_{ln} by the measured and calculated values:

$$i_{ln} = \sqrt{\frac{\sigma_{sum}^2 - \sigma_{V_{jn}}^2 - \sigma_{V_{adc}}^2}{G^2} - (i_{jn}^2 + i_{sn}^2 + i_{gn}^2 + i_{an}^2)}.$$

Table 5.3 lists the input values and result for the equation. The resulting laser noise $\bar{i}_{ln}$ can then be used to calculate the value of the laser noise factor Δl from $\Delta l = \frac{i_{ln}}{2P_0 S}$ where $P_0 = 0.95 \cdot 10^{-3}\,W$ and $S = 0.4\,{}^{A}/_{W}$. We get a value of the laser noise factor $\Delta l = 1.7 \cdot 10^{-6}$ which is fairly small compared to other sources.[57]

	Noise type	**Magnitude**
	Maximum measured SUM voltage standard deviation, σ_{sum}	$1.4 \cdot 10^{-4}\,V$
	Calculated shot noise current i_{sn}	$1.8 \cdot 10^{-11}\,A$
	Calculated generation recombination noise current i_{gn}	$2.6 \cdot 10^{-12}\,A$
=	Resulting contribution from laser noise current i_{ln}	$1.31 \cdot 10^{-9}\,A$
	Maximum measured laser position voltage standard deviation σ_{pos}	$1.8 \cdot 10^{-4}\,V$
	Maximum measured laser position voltage standard deviation from water sample, σ_{pos}^{w}	$7.1 \cdot 10^{-4}\,V$

Table 5.3: Measured laser noise

The maximum standard deviation of the position voltage from figure 4.4, equals $\sigma_{pos} = 1.8 \cdot 10^{-4}\,V$. By using equation 2.60, this corresponds to a position displacement standard deviation of $1.2 \cdot 10^{-6}\,m$ which is about one order of magnitude larger than the minimum detectable displacement of the detector. In figure 4.5 we see how the standard deviation of the measured position increases with a factor of 4 when the measurement is performed in the proper instrument configuration with a sample of pure water in the sample compartment of the instrument. The maximum standard deviation then equals $\sigma_{sum}^{w} = 7.1 \cdot 10^{-4}\,V$. This corresponds to a displacement standard deviation of $4.7 \cdot 10^{-6}\,m$ when the conditions are similar to those of an ordinary experiment. The increase in noise from passing through the water sample can be explained in two ways. Firstly, when the laser beam passes through the water sample, some of the light is absorbed in the water. This causes the temperature of the water to increase, and

refractive index to change. The heated water will then rise due to convection in the water, causing colder water to flow into the area occupied by the laser beam.[16] This will most likely cause the refractive index of the sample to oscillate with very low amplitude, which again causes a more noisy measurement. Secondly there will be a portion of the light experiencing scattering effects in the molecules of the water. Assuming that the photons in the beam scatter of the arbitrarily placed molecules in a random direction, the result is that the laser beam spot will be slightly less defined when arriving at the detector surface. This will cause a certain level of noise in the measured position.

The measured power at the detector was found to be $P_{detector} = 0.150\,mW$, which is larger than the calculated value from equation 3.5 which was $0.07\,mW$. This difference can be partly explained by looking at figure 2.6. If the incident angle θ_i on the prism-water interface of the first prism is less than the expected value of 30.7^o the transmittance of the interface will be larger than the assumed value of $T = 0.7$. This means that a larger portion of the light actually is transmitted. Further more, considering that the measured laser power $P_0 = 1.123\,mW$ was found to be slightly larger than its specifications, the difference is even smaller.

5.2 Measurement uncertainty

The total measurement uncertainty is a very important parameter of any instrument. It describes the instruments ability to replicate the actual value of the measured parameter. In this case the instrument measures the refractive index of the sample. When calculating the uncertainty we consider three different factors to quantify it. First we look at the instruments ability to accurately measure a given refractive index. The experiment was conducted by measuring the refractive index 1000 times per water sample with an effective frequency of $10\,Hz$, using the mean value as the best representation of the measured values. The standard deviation of this measurement describes how accurately the measured refractive index can be expressed. The cause of the standard deviation is the noise sources in the system. Secondly, we have conducted each measurement two times in a row. The difference between the two measured values from the same water sample describes the instruments ability to measure the same value over time. This is often called repeatability. Thirdly, we have repeated the double experiment after the instrument has been disassembled and then reassembled. The difference between the measured values prior to and after this describes the instruments ability to reproduce the same value in slightly different conditions.

In the following text we will discuss these three factors and finally determine the measurement uncertainty.

5.2.1 Position sensitive detector

The standard deviations of the measurements in figure 4.10 showed that 39 of the 40 samples have standard deviation below $12\,\mu m$, and 30 of 40 have a standard deviation below $5\,\mu m$. We know from the investigation of the noise sources that the position standard deviation originating from the noise in the laser and electrical components from an ordinary water sample accounts for approximately $4.7\,\mu m$ of this value. The difference between the sample series is also evident. Series 1 and 2 have significantly higher values than series 3 and 4. The instrument was partially disassembled and put together again after the first two experimental series. This could have introduced more stability in the system, but the exact cause is not known. There is no correlation between the level of salinity and standard deviation of the measurement.

The effective minimum detectable displacement can now be considered to have increased from $0.3\,\mu m$ to $12\,\mu m$. If we insert this into equation 3.3 we get a new value for the minimum detectable change of refractive index:

$$\Delta n_{min}^{sea} \approx 0.01 \cdot 12 \cdot 10^{-4} \approx 1.2 \cdot 10^{-5}.$$

We do however see from figure 4.9 that there is a difference between the measured values for each series. Series 1 shows the largest deviation from the other series. The maximum difference between each sample series, the instruments reproducibility, is shown in figure 5.1. It can be seen that the maximum deviation is approximately $0.16\,mm$, which through equation 3.3 corresponds to a precision in detectable refractive index of $\Delta n_{prec} = 1.6 \cdot 10^{-4}$. Figure 5.2 shows the hysteresis, or dependence on previous states of the system, of series 1 versus series 2 and for series 3 vs series 4. The average value of the hysteresis is much larger in the first two series compared to the last two. The maximum value of the hysteresis, representing the instruments repeatability, is approximately $0.12\,mm$. This corresponds to $\Delta n_{prec} = 1.2 \cdot 10^{-4}$. The cause of the hysteresis is most likely found in the shape of the sample chamber of the instrument and in the hosing leading to the water pump. When a water sample is removed from the sample chamber a random amount of the water sample will remain in the chamber. This was observed early in the construction phase. It is also observed that a portion of water is left in the hose leading from the sample chamber to the water pump. The

remaining water will decrease the salinity of the next sample if the experiment is conducted on increasing sample salinity, and increase the salinity of the sample if the experiment is conducted on decreasing sample salinity. The cause of different hysteresis in the two pairs of measurement series can not be explained directly by the experimental data. But if we look at the mean position voltage in figure 4.4 we could get an indication, as the position voltage never seem to stabilize properly even after 1 hour of continuos operation. The slight slope of the plot means that a single water sample will be measured with one displacement value at time t_1 and a different value at later time, t_2.

Another factor that could play a role is the thermo-optic coefficient of the $ZnSe$ prism. The thermo-optic coefficient of the prism is given as $1.1 \cdot 10^{-4}\, K^{-1}$. The temperature of the water samples where found to vary 0.4^o within one sample series. If we assume that the prism experienced the same temperature change, this results in a refractive index change of

$$\Delta n_{ZnSe} \approx 4.4 \cdot 10^{-5}.$$

From the derivation in appendix A we find that this corresponds to a laser beam displacement error of $0.034\, mm$. This effect can account for one third of the observed repeatability error.

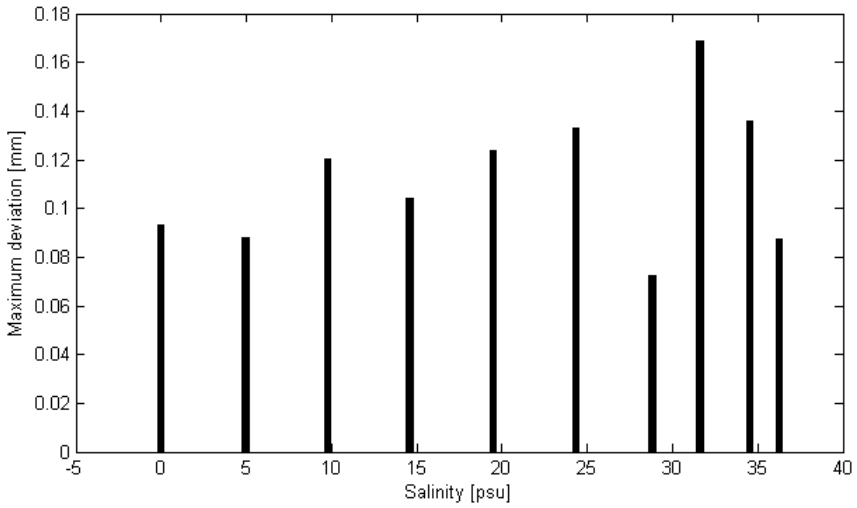

Figure 5.1: Maximum deviation in all seawater series

The standard deviations from the $NaCl$ solution sample series were presented in figure 4.12. We observe that 36 of 38 measurements have standard deviations below $4\mu m$. This is approximately one third the value of the results observed in the seawater data. By using equation 3.3, it corresponds to a min-

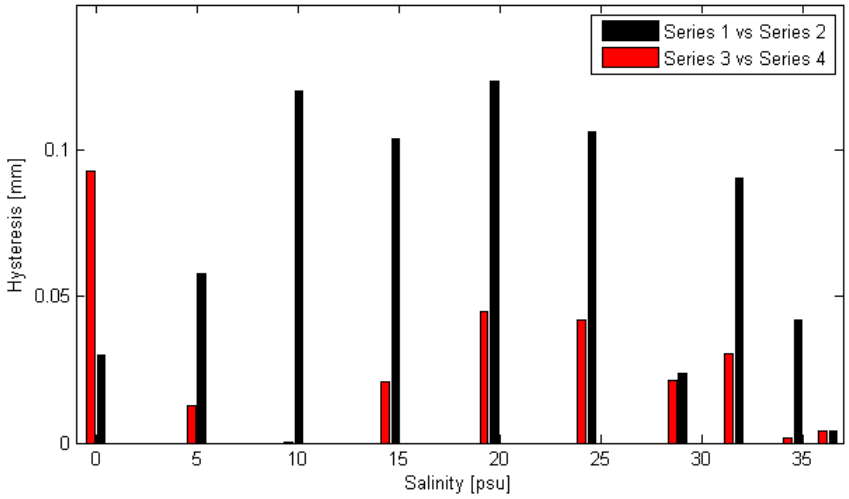

Figure 5.2: Hysteresis in seawater series

imum detectable refractive index change of $\Delta n_{min}^{NaCl} = 0.01 \cdot 4 \cdot 10^{-4} = 4 \cdot 10^{-6}$. This indicates that the sea water samples cause more noise.

If we look at the maximum deviation between all the measured positions for each level of concentration, shown in figure 5.3, we see values of $0.35\,mm$, which is almost twice the values observed in the seawater data. This could be caused by a slightly different placement of one or more of the components after the instrument was disassembled. Considering the hysteresis for each pair of measurement series shown in figure 5.4, we see that the first two measurement series conducted on the same day shows a hysteresis of less than $0.06\,mm$. The second pair of series, conducted the following day after disassembling the instrument, shows a hysteresis of less than $0.15\,mm$. The lacking data for concentrations 2 and 2.5 are caused by the user error described in chapter 4. We see the same effect as in the seawater data, where one pair of sample series have less hysteresis than the other. The overall cause of the hysteresis is most likely the same as described for the seawater measurements, being left over water in the chamber and hose from the last measurement. The cause of the deviation between the two pairs of measurement series is also most likely related the same issue as described for the seawater measurements.

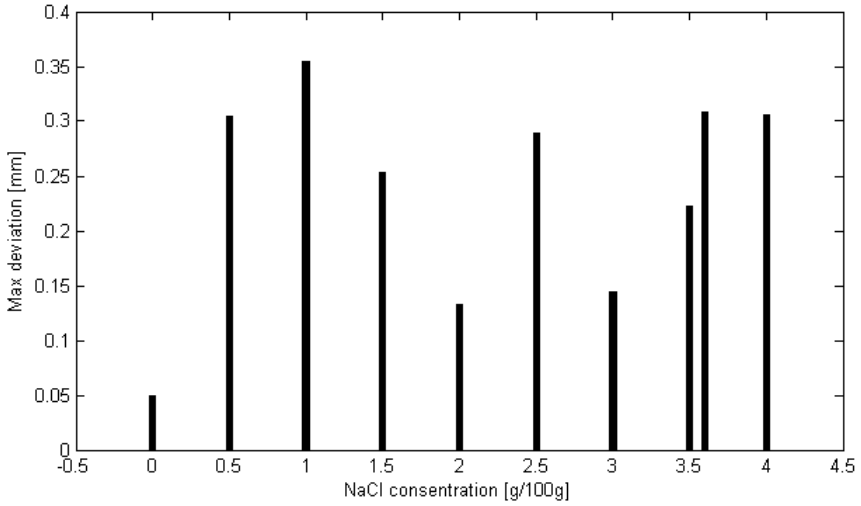

Figure 5.3: Maximum deviation in all $NaCl$-series

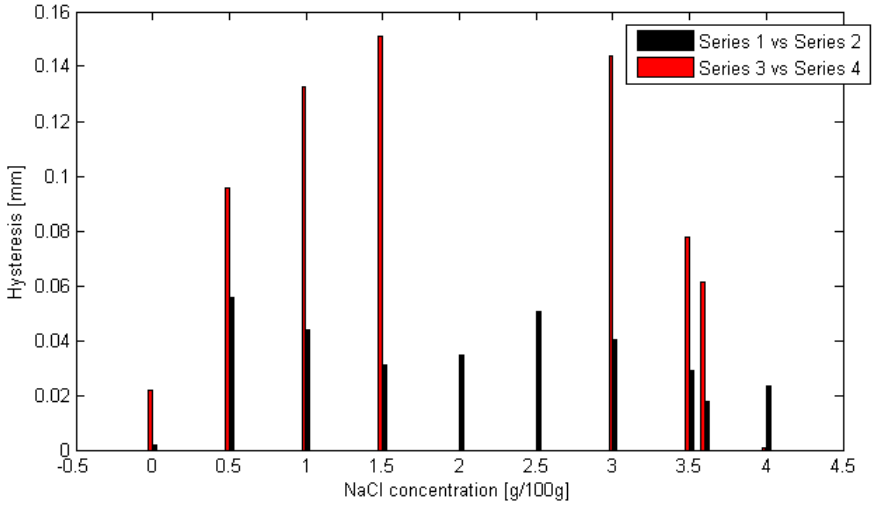

Figure 5.4: Hysteresis in $NaCl$-series

5.2.2 Quadrant cell photodiode

The measured data from the quadrant cell diode sample series were presented in figure 4.13. To extract position information from the from the measured position voltage ratio V_H/V_{sum} we must apply equation 2.62 to measured values. The equation is based on the assumption that the beam is circular and that the intensity is evenly distributed inside the spot area. This is determined by observing the beam after it has passed through the measurement chamber as shown in figure 4.7. It can be seen that the beam is almost circular and the radius is measured to be $0.38\,mm$. It is also obvious that the beam intensity is unevenly distributed. This

will cause error in the exact position determination. We then plot the standard deviation of the measured values as length in stead of voltage ratio, as shown in figure 5.5. The maximum position standard deviation is $3.91 \cdot 10^{-6}$ which is similar to the results from the position sensitive device $NaCl$ sample series. If we insert this into equation 3.3 we get a value for the minimum detectable change of refractive index:

$$\Delta n_{min}^{quad} \approx 0.01 \cdot 4 \cdot 10^{-4} \approx 4 \cdot 10^{-6}.$$

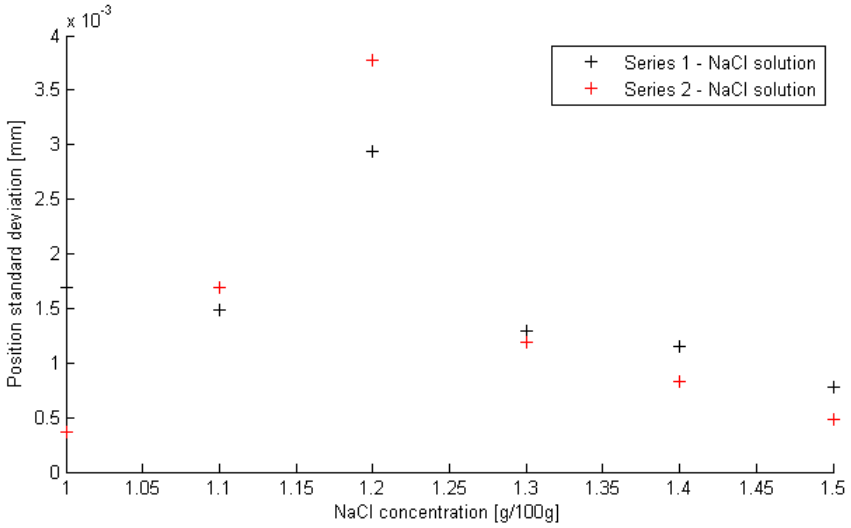

Figure 5.5: Standard deviation of measured position

To evaluate these results we can define the measurement uncertainty of the instrument in two ways. Firstly, by defining the uncertainty of a measurement series where the instrument is left untouched. The maximum error of the instrument is given by the largest value of the accuracy and the repeatability, represented by the hysteresis. Both the seawater and $NaCl$ solution data then give the refractive index precision as $\Delta n_{prec} \approx 1.5 \cdot 10^{-4}$ as dictated by the repeatability. Secondly, we can define an absolute precision, taking into account the possibility of disassembling the instrument, the refractive index precision increases to approximately $\Delta n_{prec} = 3.5 \cdot 10^{-3}$. From the discussion we see that it is the time dependence of the output from the position sensitive detector, described in 4.4, is a major contributor to this uncertainty, along with the temperature change of the prism. We must also consider the constructive limitations of the measurement chamber and pump hose which cause hysteresis. When the instrument is used to measure the refractive index of several samples of discrete salinity, the hysteresis which follows from the water left in the chamber and hose will affect the uncertainty of the measurement.

If we look beyond the impact of hysteresis, the instrument could have had an refractive index detection limit of $1 \cdot 10^{-5}$ for seawater samples and $4 \cdot 10^{-6}$ for $NaCl$ samples. The major contribution to this figure is given by the laser noise and the noise from the signal processing circuit, as described in table 5.3. The quadrant cell photodiode performs much in the same way as the position sensitive detector in terms of uncertainty, but the experiment is limited and does not take repeatability and reproducibility into account.

5.3 Theoretical fit

To compare the relationship of refractive index and resulting displacement of the laser beam of the instrument to the computer simulation represented by equation 3.1, we can plot the measured laser spot displacement along with the calculated refractive index of the samples. We calculate the refractive index of each sample by using equation 2.74 for the seawater data and equation 2.70 for the $NaCl$ solution data, by inserting the known salinity or salt concentration along with the measured temperature of each sample. The results for each configuration is presented below.

5.3.1 Position sensitive detector

We start by looking at the seawater data. We plot the measured laser beam displacement on the x-axis versus the refractive index of each sample on the y-axis as done in figure 5.6 along with a modified version of equation 3.1:

$$n_{adj} = 1.344 - 0.0115 \cdot X + 0.9618 \cdot 10^{-3} \cdot X^2 + 0.1293 \cdot 10^{-3} X^3 + 3.823 \cdot 10^{-6} X^4 - \Delta n_{adj}, \tag{5.1}$$

where Δn_{adj} describes the deviation of position of the detector in the instrument versus the simulated position. This value was found to be $\Delta n_{adj} = 3.2 \cdot 10^{-3}$. The range of the refractive index is $\Delta n_{sea} = 6.5 \cdot 10^{-3}$. We also observe the range of the measured displacement being less than the range predicted by the simulation. To explain this we must look at the transmitted angle as a function of the incident angle on the prism-water interface in Prism 1 from figure 3.1, described in figure 2.7. The response of the transmitted angle to change in refractive index is less sensitive the further away from the critical angle you get. This is directly related to the incident angle, which in the simulation is chosen to be 30.7^o. We can conclude that the incident angle on the instrument must be less than the value

from the simulation. This could be caused by inaccuracy in the placement of the prism and the laser compared to their position in the simulation.

From the figure we can observe that the simulation predicts the refractive index fairly well. We do however see some measurements that does not correlate with the simulation. The data points representing the pure water samples does not coincide with the plot of equation 5.1. This can not be explained from the experiment or theory. A reference measurement of the water sample refractive index would provide better knowledge of this discrepancy.

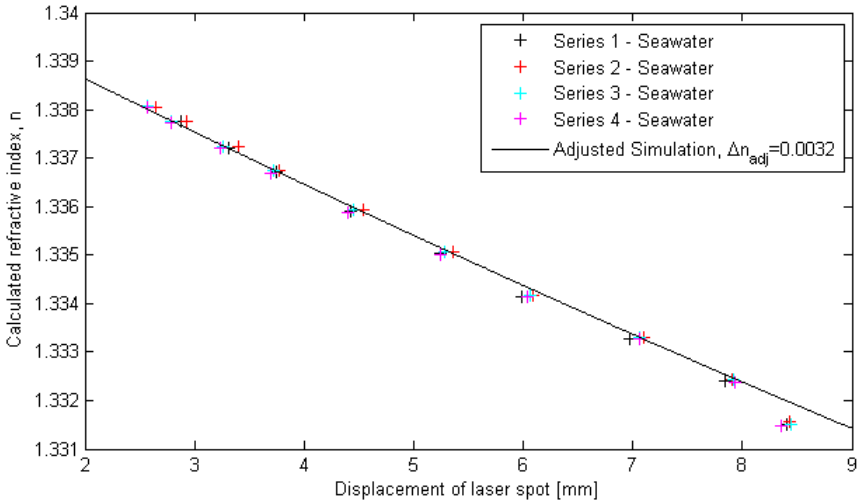

Figure 5.6: Calculated refractive index versus measured displacement of laser spot. Plot of equation 5.1 superimposed on measured data.

We then look at the $NaCl$ solution data. We plot the measured laser beam displacement and the calculated refractive index in figure 5.7, with equation 5.1 superimposed. The value of Δn_{adj} was found to be $1.8 \cdot 10^{-3}$. The range of measured refractive index is $\Delta n_{NaCl} = 6.8 \cdot 10^{-3}$. The difference of Δn_{adj} here compared to the seawater data is a source of concern, as the detector placement is the same is for the seawater data. The Seaver-Millard relation and the IAPWS equation described in appendix B give deviating values for the refractive index of the pure water sample. The same deviation is found when comparing tables in Refs [47] and [52]. Figure 5.6 indicates that the Seaver-Millard equation fails to describe the refractive index of pure water, as all samples except the pure water sample coincide with the computer simulation.

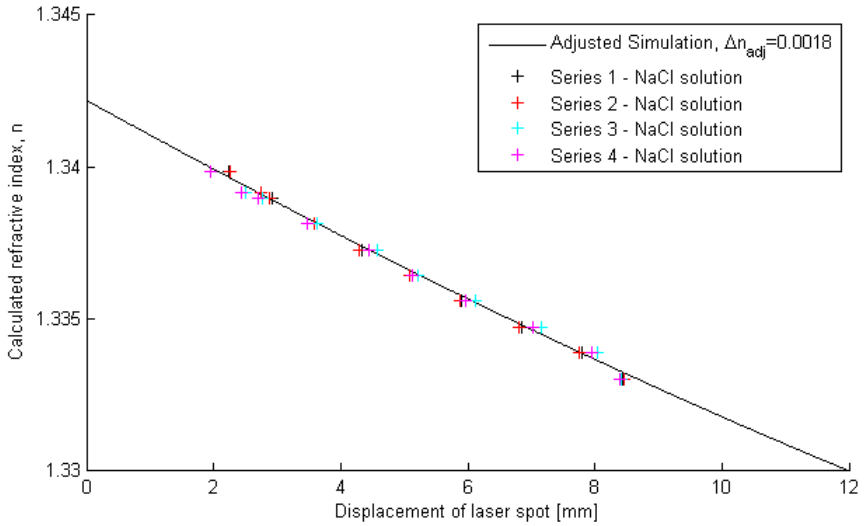

Figure 5.7: Calculated refractive index versus measured displacement of laser spot. Plot of equation 5.1 superimposed on measured data.

5.3.2 Quadrant cell photodiode

We plot the measured position on the x-axis and the calculated refractive index on the y-axis, along with the adjusted version of equation 5.1 in figure 5.8. The position scale has been adjusted so that the center of the detector is defined as $6\,mm$. We see that the measured values behave almost as predicted when inside $\pm 0.3\,mm$ of the center of the detector, corresponding to a concentration range of $\Delta S_{quad} = 0.2\,{}^{g}/_{100g}$ within this range. The refractive index range is $\Delta n_{quad} = 8.5 \cdot 10^{-4}$. The deviation from the adjusted simulation plot is most likely caused by the uneven distribution of the light intensity inside the laser spot. The measured values further from the center of the detector than the beam radius will, as discussed in section 2.4.2, not give accurate position measurements. This explains how the computer simulation fails to describe the two samples of highest refractive index.

We see that both detectors replicate the computer predicted instrument performance in a good manner after a calibration term Δn_{adj} has been introduced. We do observe some discrepancies from the predicted values in the seawater data which could have been avoided if a reference measurement of the refractive index of each sample had been done parallel to the experiment. The quadrant cell photodiode is not performing perfectly according to theory and calculations. The cause is most likely the uneven distribution of intensity inside the laser beam.

We have now determined the refractive index range Δn and the refractive

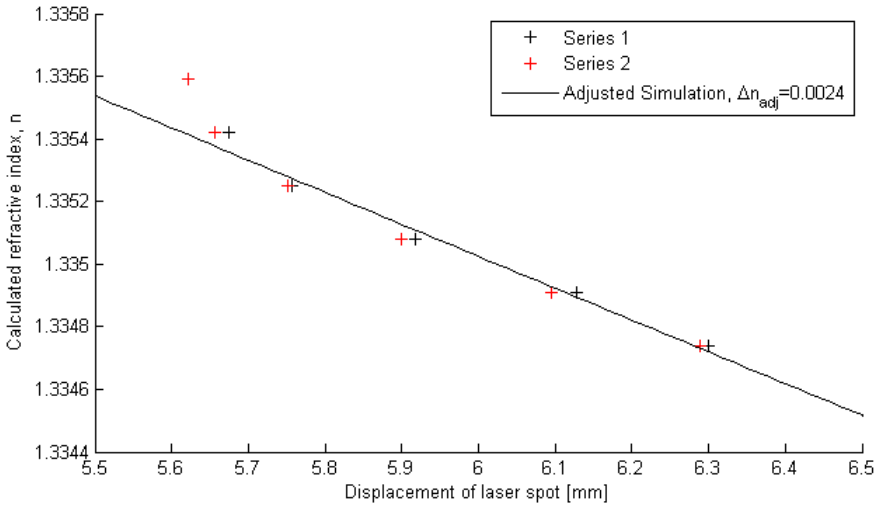

Figure 5.8: Calculated refractive index versus measured displacement of laser spot. The adjusted computer simulation is superimposed on measured data.

index precision Δn_{prec}. We also know the range of the salinity ΔS. This means that we can determine the salinity precision ΔS_{prec} by the following formula:

$$\frac{\Delta n_{prec}}{\Delta n} = \frac{\Delta S_{prec}}{\Delta S}.$$

This gives a seawater salinity precision of $\Delta S_{prec}^{sea} = 8.35 \cdot 10^{-1}\, psu$ when the refractive index precision is $\Delta n_{prec}^{sea} = 1.5 \cdot 10^{-4}$. The $NaCl$-solution concentration precision is $\Delta S_{prec}^{NaCl} = 8.82 \cdot 10^{-2}\, {}^{g}/_{100g}$ when the refractive index precision is $\Delta n_{prec}^{NaCl} = 1.5 \cdot 10^{-4}$. The quadrant cell detector $NaCl$-solution concentration precision is $\Delta S_{prec}^{quad} = 6.37 \cdot 10^{-5}\, {}^{g}/_{100g}$ when the refractive index precision is $\Delta n_{prec}^{quad} = 4 \cdot 10^{-6}$. This number is low as the refractive index precision is based on a limited experiment, but it still indicates that the quadrant cell detector may be capable of better or at least equal performance as the position sensitive device within a small refractive index range. This could be interesting, since a dominant part of the seawater has a salinity very close to $35\, psu$.

5.4 Biological fouling errors

Biofouling is the effect of having growth of biological organisms on an optical surface. The effect has not been examined experimentally, but a theoretical exploration of the effect of fouling will now be given, along with some possible reduction techniques. In a marine environment there are several thousand dif-

ferent organisms capable of fouling an optical surface. The size of the organisms provides a way of distinguishing the different types of growth. On the micro end of the scale we have biofilm, being the result of microscopic organisms growth, while macroscopic growth of barnacles and mussels defines the other end. Between these stages there will be an increase in the size and complexity of the organisms. It is also partially time dependent as the biofilm forms in minutes after submersion, while the bigger organisms occur after hours or days. It is however very difficult to predict how and when the different stages of fouling occur. Several factors comes in to consideration such as temperature, salinity, pH, dissolved oxygen, light, location and several other biological and physical factors. [66]

It is clear that the described effects will have major implications for deployment of optical measurement systems in marine environments. The fouling will cause attenuation of the laser light by means of absorption and scattering. [67, 68] For the instrument being discussed in this thesis, both of these effects are unwanted and a cause of error and noise. The absorption will, at a given level, cause such a low transmission of optical power that the instrument will be rendered useless. Scattering could cause a portion of the photons in the light to deviate from their intended beam path. It would however be reasonable to assume that the biological particles causing the scattering are randomly distributed on the optical window. This means that the laser beam passing through this layer of particles will be scattered equally in all directions and the net effect of scattering would only be that of reduced intensity in the center of the beam and a slightly increased size of the beam. It would therefore be reasonable to add the attenuative effects of both scattering and absorption into one attenuation coefficient α_{bio}. This coefficient then describes the attenuation of a beam through the Lambert-Beer law as

$$I = I_0 e^{-\alpha_b l_{bio}},$$

where I_0 is the intensity of the source, I is the intensity of the wave after passing through a substance of length l_{bio} and attenuation coefficient α_{bio}. This attenuation comes in addition to the already determined attenuation in the seawater.

We can reduce biofouling by a number of methods. We can make the instrument compartment inhospitable to organic organisms by adding poisonous substances such as copper, chlorine or tributyltin in the form of coatings or paint to the sample water or surfaces of the cabinet. We can filter the water before it enters an enclosed measurement chamber, or we can use an open measurement setup and clean the optical surfaces regularly either by integrated systems or by

hand when the instrument is taken out of the water. Experiments indicate that a combination of poison and open or closed instrument is the best alternative.[67]

The instrument constructed for this thesis was built as a closed system with a pump to introduce the water to the measurement chamber. This would however not be the ideal choice for an in-situ instrument. The pump system would increase the overall size, which is unwanted. The most plausible solution for the realization of this particular setup in an in-situ instrument is to convert it to an open system by removing the walls in the measurement chamber. The compact design of the instrument limits the possibilities of integrated mechanical cleaning devices, and it would therefore need to be cleaned by external systems or by hand. The deployment of poison in the measurement chamber is considered to be possible, for instance by using paint or coatings on the framework of the measurement chamber.

5.5 Further work

In the previous discussion of this chapter we have identified some disadvantages that have limited the accuracy of the instrument. This section will give some proposals on how this could be modified to improve the accuracy and reliability of the instrument. The most significant problems in the instrument setup are related to the laser and the detector. The continuos wave laser beam produced by the laser diode module is not ideal for this kind of measurement setup, as it heats and thereby changes the refractive index of prisms and water sample, as well as a thermal effect causing temporal variations in photocurrent output. The impact of component heating would most likely be significantly reduced if a pulsed laser with low duty cycle had been used instead. The use of a $ZnSe$ prism is also a drawback in this respect, because of its relatively high absorption and thermo-optic coefficients. The significant temperature dependency in the detector is a major source of measurement uncertainty in the system. By removing this effect, the overall accuracy of the system would increase significantly. This could be done by attaching a miniature controlled Peltier element and temperature probe directly behind the position sensitive detector, and in this way monitor and control the temperature of the detector.

There are also possible improvements which were considered in the planning process but later disregarded for practical reasons. The most important issue in this context is the construction of the instrument cabinet and placement

of components. This was largely done by hand, resulting in several small discrepancies between the computer simulation and the physical instrument. It is especially visible in the actual laser beam displacement range of $6.8\,mm$, compared to the simulated range of $10\,mm$. It could be improved by constructing the instrument cabinet on the basis of a precise computer design process. The use of lenses to shrink the beam could also extend the active length of the detector closer to $12\,mm$. Another possible improvement is to include two lasers of different wavelength in the instrument. This would improve the reliability of the measured refractive index, and would also to a certain extent make the system redundant to for instance biological fouling or component failure. Research on how the instrument tolerates biological fouling would also be a natural progression of the investigation.

5.6 Conclusion

The thesis has documented the construction and experimental testing of a compact refractometer for measuring the refractive index and salinity of seawater and $NaCl$ solutions. Compared to the specific size goal presented in chapter 1, the work presented suggest that it is possible to construct a compact refractometer with a volume of $103\,cm^3$, which is comparable to the cylindrical modular sensor with a volume of $82\,cm^3$. The desired level of precision in refractive index measurement was set to 10^{-6} refractive index units. When repeated measurements are taken, the precision in refractive index measurement is $1.5 \cdot 10^{-4}$ refractive index units. The quadrant cell diode achieved a precision of 10^{-6}. The cause of the increased uncertainty compared to the design goal is considered to be a temperature dependent process in the position sensitive detector.

References

[1] Darcy J. Gentleman and Karl S. Booksh. Determining salinity using a multimode fiber optic surface plasmon resonance dip-probe. *Talanta*, 68:504–515, 2006.

[2] Robert H. Stewart. *Introduction to physical oceanography.* Augusta, 2003.

[3] E. M. Stanley. The refractive index of sea water as a function of temperature, pressure and two wavelengths. *Deep-Sea Research*, 18:833–840, 1971.

[4] Frank J. Millero, Rainer Feistel, Daniel G. Wright, and Trevor J. McDougall. The composition of standard seawater and the definition of the reference-composition salinity scale. *Deep-Sea Research I*, (55):50–72, 2008.

[5] Arthur M. Pederson and Michael C. Greg. Development of a small in-situ conductivity instrument. *IEEE Journal in Oceanic Engineering*, OE-4(3):69–75, 1979.

[6] Philippe Grosso, Marc Le Menn, Jean-Louis De Bougrenet De La Tocnaye, Zong Yan Wu, and Damien Malarde. Practical versus absolute salinity measurements: New advances in high performance seawater salinity sensors. *Deep-Sea Research I*, 1(57):151–156, October 2010.

[7] Lynne D Talley. *Descriptive Physical Oceanography, Sixth Edition.* Academic Press, 2011.

[8] *The international thermodynamic equation of seawater -2010.* The Intergovermental Oceanographic Comission, 2010.

[9] Jimmy Castillo, Carlos Canelon, Socrates Acevedo, Herve Carrier, and Jean-Luc Daridon. Optical fiber extrinsic refractometer to measure ri of samples in

a high pressure and temperature systems: Application to wax and asphaltene precipitation measurements. *Fuel*, 85:2220–2228, 2006.

[10] Kenichi Asakawa, Yasuhisa Ishihara, Yukio Takahashi, Tomohiko Sugiyama, and Akito Araya. Basic experiments on measurement of salinity using a heterodyne michelson interferometer. In *OCEANS 2010*, pages 1–5. IEEE, 2010.

[11] Yong Zhao and Yanbiao Liao. Novel optical fiber sensor for simultaneous measurement of temperature and salinity. *Sensors and Actuators*, B(86):63–67, 2002.

[12] Christian Hubner, Ingo Klimant, Christian Krause, Tobias Werner, Torsten Mayr, and Otto S. Wolfbeis. Optical sensor for seawater salinity. *Fresenius J Anal Chem*, 368:196–202, 2000.

[13] N Diaz-Herrera, O Esteban, M C Navarrete, M Le Haitre, and A Gonzalez-Cano. In situ salinity measurements in seawater with a fibre-optic probe. *Measurement Science And Technology*, 17:2227–2232, 2006.

[14] SCOR/IAPSO WG127. *Certified Research and Development Need - Refractive index of sea water*, 2009.

[15] Aadi seaguard - last checked: 2011-08-10. `http://www.aadi.no/Aanderaa/Products/Seaguard/Default.aspx`.

[16] Hugh D. Young and Roger A. Freedman. *University Physics With modern Physics*. Pearson, 13th. edition, 2011.

[17] Max Born and Emil Wolf. *Principels of optics*. Cambridge University Press, 7th edition, 1999.

[18] Charles Kittel. *Introduction to Solid State Physics*. John Wiley and Sons, 7th edition, 1996.

[19] Kamal M. My and E. Esmai. Refractive index of salt water: effect of temperature. *Optical Materials*, 2, 1993.

[20] Sophocles J. Orfanidis. Electromagnetic waves and antennas - last checked: 2012-05-02. `http://www.ece.rutgers.edu/~orfanidi/ewa`, 2010.

[21] Gorachand Ghosh. Sellmeier coefficients and dispersion of thermo-optic coefficients for some optical glasses. *Applied Optics*, 36(7), 1997.

[22] Justin Peatross and Michael Ware. *Physics of light and optics*. Brigham Young Universit, 2008.

[23] B. E. A. Saleh and M. C. Teich. *Fundamentals of Photonics*. Wiley, 2006.

[24] C. de Greef E. Moreels and R.Finsy. Laser light refractometer. *Applied Optics*, 23(17):3010–3013, 1984.

[25] Shyam Singh. Refractive index measurement and its applications. *Physica Scripta*, 65:167–180, 2002.

[26] A Brandenburg, Rainer Edelhauser, and Frank Hutter. Integrated optical gas sensor using organically modified silicates as sensitive films. *Sensors and Actuators B*, 11:361–374, 1993.

[27] Zhi-Cheng Jian, Po-Jen Hsieh, Hung-Chih Hsieh, Huei-Wen Chen, and Der-Chin Su. A method for measuring two-dimensional refractive index distribution with the total internal reflection of p-polarized light and the phase-shifting interferometry. *Optics Communications*, 268:23–26, 2006.

[28] L.E. Helseth. Simultaneous measurements of absorption spectrum and refractive index in a microfluidic system. *Optics Express*, 20(4), 2012.

[29] G. Seaver, V. L. Vlasov, and A. G. Kostianoy. Laboratory calibration in distilled water and seawater of an oceanographic multichannel interferometer-refractometer. *J. Atmos. Ocean. Tech.*, 14:267, 1997.

[30] Chuang Wu, Bai-Ou Guan, Chao Lu, and Hwa-Yaw Tam. Salinity sensor based on polyimide-coated photonic crystal fiber. *Optics Express*, 19(21):20003–20008, 2011.

[31] Oscar Esteban, Maria Cruz-Navarrete, Agustin Gonzalez-Cano, and Eusebio Bernabe. Measurement of the degree of salinity of water with a fiber-optic sensor. *Applied Optics*, 38(25):5267–5271, 1999.

[32] E. Hutter, J. H. Fendler, and D. Roy. Surface plasmon resonance studies of gold and silver nanoparticles linked to gold and silver substrates by

2-aminoethanethiol and 1,6-hexanedithiol. *J. Phys. Chem. B*, 105:11159–11169, 2001.

[33] Kuang-An Chang, Ho-Joon Lim, and Chin B Su. A fibre optic fresnel ratio meter for measurements of solute concentration and refractive index change in fluid. *Measurement Science And Technology*, 12:1962–2965, 2002.

[34] Hamamatsu. Psd s3932 data sheet - last checked: 2012-05-02. `http://sales.hamamatsu.com/assets/pdf/parts_S/s3931_etc_kpsd1002e06.pdf`.

[35] Rakesh Singh, Joni M. Hattuniemi, and Anssi J. Mäkynen. Analysis of accuracy of laser spot centroid estimation. *Proc. of SPIE*, 7022, 2008.

[36] Hamamatsu. Opto-semiconductor handbook - last checked: 2012-05-02. `http://jp.hamamatsu.com/sp/ssd/tech_handbook_en.html`.

[37] Hamamatsu. Signal processing circuit c3683-01 - last checked: 2012-05-02. `http://sales.hamamatsu.com/assets/pdf/parts_C/C3683-01.pdf`.

[38] John P. Bentley. *Principles of Measurement Systems*. Pearson Education Limited, 4th edition, 2005.

[39] OSI Optoelectronics. Quadrant and bi-cell silicon photodiode amplifier module data sheet - last checked: 2012-05-02. `http://www.osioptoelectronics.com/standard-products/silicon-photodiodes/position-sensing-detectors/position-sensing-detectors-overview.aspx`.

[40] W. Sellmeier. Zur erklärung der abnormen farbenfolge im spectrum einiger substanzen. *Annalen der Physik und Chemie*, (219), 1871.

[41] *Handbook of Optics*, volume 4. McGraw-Hill Professional, 3 edition, 2009.

[42] K. T. Tang. One-term sellmeier formula for dispersion of dilute gases. *Journal of the Opical Society of America*, 62(5):644–648, 1972.

[43] Schott optical glass datasheet - last checked: 2012-05-02. `http://edit.schott.com/advanced_optics/us/abbe_datasheets/schott_datasheet_all_us.pdf`.

[44] R. J. Harris, G. T. Johnston, G. A. Kepple, P. C. Krok, and H. Mukai. Infrared thermooptic coefficient measurement of polycrystalline znse, zns, cdte, caf2 , and baf2 , single crystal kci, and ti-20 glass. *Applied Optics*, 16(2):436–438, 1997.

[45] H.H. Li. Refractive index of zns, znse and znte and its wavelength and temperature derivates. *J. Phys. Chem. Ref. Data*, 13(103), 1984.

[46] Guildline. Guildline 8410a portsal data sheet - last checked: 2012-05-02. `http://www.guildline.com/Datasheet/Guildline8410ADatasheet.pdf`.

[47] P. Schiebener, J. Straub, J. M. H. Leveit Sengers, and J. S. Gallagher. Refractive index of water and steam as function of wavelength, temperature and desnisty. *J. Phys. Chem. Ref. Data*, 19(3):667–717, 1990.

[48] IAPWS. *Release on the Refractive Index of Ordinary Water Substance as a Function of Wavelength, Temperature and Pressure*, 1997.

[49] Jon P. Longtin and Ching-Hua Fan. Precision laser-based consentration and refractive index measurement of liquids. *Microscale Thermophysical Eng*, 2:261–272, 1998.

[50] David R. Linde, editor. *CRC Handbook of Chemistry and Physics*. CRC Press, 85th edition, 2004.

[51] K. Nortemann, J. Hilland, and U. Kaatze. Dielectric properties of aqueous nacl solutions at microwave frequencies. *J. Phys. Chem. A*, 101:6864–6869, 1997.

[52] R.C. Millard and G. Seaver. An index of refraction algorithm for seawater over temperature, pressure, salinity, density, and wavelength. *Deep Sea Resaerch*, 37(12):1909–1926, 1990.

[53] Xiaohong Quan and Edward S. Fry. Empirical equation for the index of refraction of seawater. *Applied Optics*, 34(18):3477–3480, 1995.

[54] W B Florian and M.A.C Nascimento. Dielectric constant and density of water as a function of pressure at constant temperature. *Brazilian Journal of Physics*, 34(1):38–41, 2004.

[55] Geir Anton Johansen. Pc i instrumentering og prosessregulering. Course material from UIB-PHYS327.

[56] Terry W. McDaniel and Randall H. Victoria, editors. *Handbook of Magneto-Optical Data Recording*. Noyes Publications, 1996.

[57] L.E. Helseth and T.M. Fischer. Fundamental limits of optical microrheology. *Journal of Colloid and Interface Science*, 275:322–327, 2004.

[58] Chubing Peng and M. Mansuripu. Sources of noise in erasable optical disk data storage. *Applied Optics*, 37(5):921–928, 1998.

[59] Amnon Yariv. *Optical Electronics in Modern Communications*. Oxford University Press, fifth edition, 1997.

[60] Dieter K. Schroder. Carrier lifetimes in silicon. *IEEE Transactions on Electron Devices*, 44(1):160, 1997.

[61] H. T. Friis. Noise figures of radio recivers. *Proceedings of the I.R.E*, pages 419–422, July 1944.

[62] National Instruments. National instruments usb9239 data sheet - last checked: 2012-05-02. `http://www.ni.com/pdf/manuals/372409a.pdf`.

[63] Carmetal dynamic cad software - last checked: 2012-05-02. `http://db-maths.nuxit.net/CaRMetal/index_en.html`.

[64] E. Rzepka, J.P. Roger, P. Lemasson, and R. Triboulet. Optical transmission of znse crystals grown by solid phase recrystallization. *Journal of Crystal Growth*, 197:480–484, 1999.

[65] A. Morel. *Optical aspects of oceanography*. Academic Press, 1974.

[66] L. Delauney, C. Compere, and M. Lehaitre. Biofouling protection for marine enviromental sensors. *Ocean Sci*, 6:503–511, 2010.

[67] Derek V. Manov, Grace C. Chang, and Tommy D. Dickey. Methods for reducing biofouling of moored optical sensors. *Journal of Atmospheric and Oceanic Technology*, 21(6):958–968, 2004.

[68] A. Kerr, M.J. Cowling, C.M. Beveridge, M.J. Smith, and A.C.S. Parr. The

early stages of marine biofouling and its effect on two types of optical sensors. *Environment International*, 24(3):331–343, 1998.

[69] D Malarde, Z Y Wu, P Grosso, J-L de Bougrenet de la Tocnaye, and M Le Menn. High-resolution and compact refractometer for salinity measurements. *Measurement Science And Technology*, (20):1–8, 2009.

[70] Les Kirup and Bob Frenkel. *An introduction to Uncertianty in Measurment.* Cambridge University Press, 2006.

[71] Dana R. Kester, Iver W. Deudall, Donald N. Connors, and Ricardo M. Pytkowicz. Preparation of artificial seawater. *Limnology and Oceanography*, 12(1):176–179, 1967.

APPENDICES

Appendix A

Refractive index as function of beam position displacement

To describe how the refractive index of the water affects the position of the laser beam, we must look at how the laser beam is affected by reflection and refraction on its path from the laser to the detector. The derivation of the expression is intricate, but by using figure A.1 we can explain how this will function. We start by defining the relationships of the different angles in the figure. They are denoted by lower case letters. All angles necessary to perform the calculation is included in the figure, except for the prism angles which are 45^o and 90^o. When calculating the angles it is useful to apply the sine rule, defined as

$$\frac{sin\,A}{a} = \frac{sin\,B}{b} = \frac{sin\,C}{c}\,,$$

where the upper case letters are the three angles of triangle, and the corresponding lower case letters are the length of the sides opposite to the angle. When all the angles have been defined we go on to determine the lengths, denoted by l_i where $i = 1, 2, 3....$ The length of the laser beam path is denoted by 1.,2. and 3.

The first definition we make is the transmitted angle from the prism-water interface in the lower left corner. It is not necessary to include the beam propagation prior to this point, as it will be constant. We set this angle to 30.7^o. The expression for the transmitted angle is determined through Snells law as:

$$x = arcsin\left(\frac{n_{ZnSe}}{n_{water}} sin(30.7^o)\right)\,.$$

We start by defining angle $a = 165 - x$. We can the imagine a four sided polygon with the sides l_1, l_2 , l_4 and 1.. The sum of the internal angles in a four sided polygon always equals 360^o. We can then define angle $b = -30 + x$. The incident and reflected angle in the mirror is $c = 120 - x$. If we imagine that the mirrors

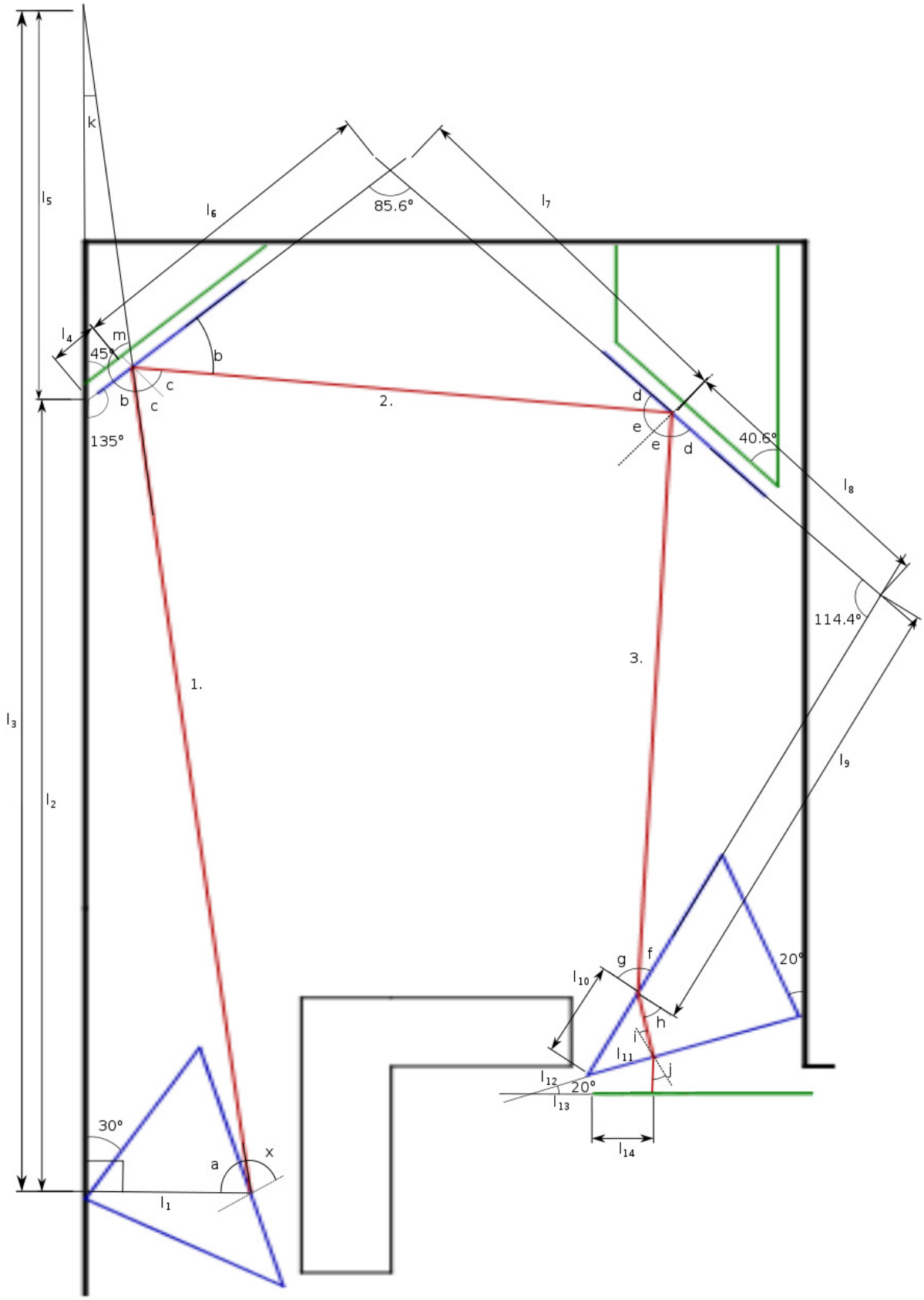

Figure A.1: Laser beam propagation calculation

are prolonged until they intersect, the intersection angle will be 85.6^o. We can then define the angle $d = 124.4 - x$ as the sum of the internal angles of triangle with the sides l_6, l_7 and 2. is 180^o. The incident and reflected angle on the second mirror can then be defined as $e = -34.4 + x$.

We can then imagine that the second mirror and the second prism are prolonged until they intersect. The intersection angle will then be 114.4^o. We can the imagine a triangle with the sides l_8, l_9 and 3. As the internal angles equal 180^o, we can define angle $f = -58.8+x$ and the incident angle on the water-prism interface as $g = 148.8 - x$. The transmitted angle from the water-prism interface is determined by Snells law as:

$$h = arcsin\left(\frac{n_{water}}{n_{BK-7}} sin(148.8 - x)\right) .$$

The sum of the internal angles of the prism gives the incident angle on prism-air interface as $i = -45 + arcsin\left(\frac{n_{water}}{n_{BK-7}} sin(148.8 - x)\right)$. The transmitted angle is again given by Snells law as:

$$j = arcsin\left[\frac{n_{BK-7}}{n_{air}} sin\left\{-45 + arcsin\left(\frac{n_{water}}{n_{BK-7}} sin\left[148.8 - arcsin\left(\frac{n_{ZnSe}}{n_{water}} sin(30.7^o)\right)\right]\right)\right\}\right]$$

We have now determined the effect of refractive index of water on the angles of the laser beam path. Although the nested inverse sine functions makes it messy, the only variable is the refractive index of water n_{water}.

We can now go on to determine the lengths. Some of the lengths must be measured, but as it is very difficult to measure the lengths on the physical instrument, the measurements will be taken from the simulation sketch. We start by measuring $l_1 = 0.916cm$ and $l_2 = 5.742$. We can then find the length of $l_3 = l_1 \cdot tan(a)$, and $l_5 = l_3 - l_2$. We can calculate the angles $m = 210 - x$ and $k = -75 + x$ and thereby get an expression for $l_4 = \frac{l_5 \cdot sin(k)}{sim(m)}$. We can know get the length of 1. $= \frac{l_1}{cos(a)} - l_4$.

To proceed we measure the length of $l_4 + l_6 = 2.335cm$. We can then express 2. $= \frac{l_6 \cdot sin(85.6)}{sin(d)}$ and $l_7 = \frac{l_6 \cdot sin(b)}{sin(d)}$. We then measure $l_7 + l_8 = 4.134cm$, and define 3. $= \frac{l_8 \cdot sin(114.4)}{sin(f)}$ and $l_9 = \frac{l_8 \cdot sin(d)}{sin(f)}$.

We measure $l_9 + l_{10} = 3.834cm$ and express $l_{11} = \frac{l_{10} \cdot sin(90-h)}{sin(90+i)}$. Lastly we measure $l_{12} = 0.386cm$ and $l_{13} = 0.407cm$ and express the laser beam position relative to the left edge of the sensor as

$$X = l_{14} = \frac{(l_{11} + 0.386) \cdot sin(90 - j)}{sin(70 + j)} - 0.407cm\,.$$

The exact function can then be found by expressing X as a function of the refractive index of water n_{water}, but as this expression is cluttered by several nested functions and occupies an entire page it is instead presented as a graph. Figure A.2 describes the laser beam position relative to the left edge of the photodetector as a function of the refractive index of seawater in the range $1.332 \leq n_{water} \leq 1.340$. The function is almost linear in the described range. The slight unlinearity is caused by the fact that the transmitted angle from the first prism-water interface is very close to the critical angle, as explained in section 3.2. By using MATLAB we can approximate the expression to a 4th degree polynom by using the least squares method, which will match the exact expression very well in the described range. We can then express the refractive index as a function of the measured laser beam position as:

$$n_{water} = 1.344 - 0.0115 \cdot X + 0.9618 \cdot 10^{-3} \cdot X^2 + 0.1293 \cdot 10^{-3} X^3 + 3.823 \cdot 10^{-6} X^4. \tag{A.1}$$

The quality of the fit can be defined in terms of the sum of the squares due to error or SSE. This is given as $SSE = 5.3 \cdot 10^{-17}$ where lower is better.

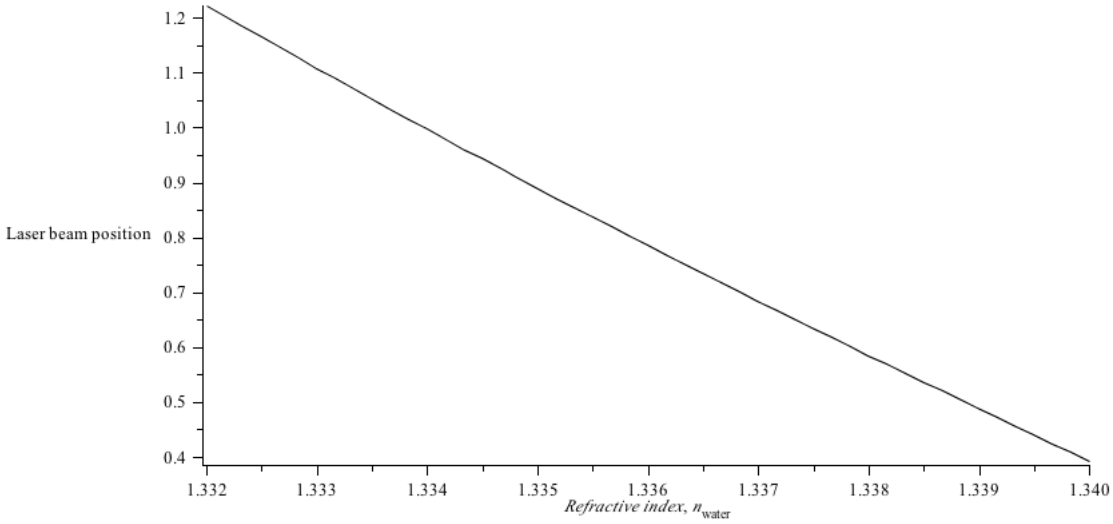

Figure A.2: Laser beam position as a function of refractive index of seawater

Appendix B

Empirically derived optical equations of state

B.1 IAPWS optical equation of state equation

The International Association on the Properties of Water and Steams "Release on the Refractive Index of Ordinary Water Substance as a Function of Wavelength, Temperature and Pressure" from 1997 [48], based on the work done by Schiebener et al. [47], describes the relationship of the refractive index to the mentioned basic environmental variables.

The presented equation is based on the Sellmeier equation derived in chapter 2, but also includes terms to take into account the pressure and temperature dependence. The constants are empirically derived from numerous relevant data sets. Its calculated absolute uncertainty in the refractive index is given as $1.5 \cdot 10^{-5}$, when the sample is at room temperature, the wavelength is that of visible light and the pressure is atmospheric. As the equation is applicable on both the liquid and gaseous phases of water, the pressure is expressed through the density. The equation is given as:

$$\frac{n^2-1}{n^2+2}\frac{1}{\rho^*} = a_0 + a_1\rho^* + a_2 T^* + a_3\lambda^{*2}T^* + \frac{a_4}{\lambda^{*2}} + \frac{a_5}{\lambda^* - \lambda_{UV}^{*2}} + \frac{a_6}{\lambda^* - \lambda_{IR}^{*2}} + a_7\rho^*, \quad \text{(B.1)}$$

where

$$\begin{aligned} \rho^* &= \rho/\rho_0 \quad & \rho_0 &= 1000\,kg\,m^{-3} \\ \lambda^* &= \lambda/\lambda_0 \quad & \lambda_0 &= 0.589\mu m \\ T^* &= T/T_0 \quad & T_0 &= 273.15\,K \end{aligned}$$

The coefficients are given as

$$\begin{aligned} a_0 &= 0.244257733 & a_4 &= 1.58920570 \cdot 10^{-3} \\ a_1 &= 9.74634476 \cdot 10^{-3} & a_5 &= 2.45934259 \cdot 10^{-3} \\ a_2 &= -3.73234996 \cdot 10^{-3} & a_6 &= 0.900704920 \\ a_3 &= 2.68678472 \cdot 10^{-4} & a_7 &= -1.66626219 \cdot 10^{-2} \\ \lambda_{UV} &= 0.2292020 & \lambda_{IR} &= 5.432937 \end{aligned}$$

B.2 Seaver-Millard equation

The Seaver-Millard equation is an empirically derived relationship describing the refractive index of seawater.[52] The equation is cited in several articles describing optical salinity measurements.[6, 69, 13] The independent variables in the equation are salinity S $[psu]$, wavelength L $[\mu m]$, temperature T $[^oC]$ and pressure P $[dbar]$. The equation is derived by the least square method curve fit from four independent data sets of high accuracy. The data sets spans different ranges of the independent variables. The 27 term equation can be divided into 4 sub equations based on each data set:

$$N = N_I + N_{II} + N_{III} + N_{IV},$$

where N is the total refractive index of the seawater sample. Each sub equation includes a total of 27 curve fit coefficients. The data sets and their sub equation are presented below.

Region I The first region is based on measurements of refractive index in pure water in standard atmospheric conditions. The independent variables in this sub equation are therefore the wavelength L and the temperature T. The coefficients are presented in table B.1.

$$\begin{aligned} N_I = & A_0 + L_2 \cdot L^1 + \frac{LM_2}{L^2} + \frac{LM_4}{L^4} + \frac{LM_6}{L^6} + \\ & T_1 \cdot T + T_2 \cdot T^2 + T_3 \cdot T^3 + T_4 \cdot T^4 + TL \cdot T \cdot L + \\ & T_2L \cdot T^2 \cdot L + T_3L \cdot L \cdot T^3 \end{aligned}$$

$A_0 = 1.3280657$	$T_2 = -.0000030738272$
$L_2 = -.0045536802$	$T_3 = .000000030124687$
$LM_2 = .0025471707$	$T_4 = -2.0863178 \cdot 10^{-10}$
$LM_4 = .000007501966$	$TL = .000010508621$
$LM_6 = .000002802632$	$T_2L = .00000021282248$
$T_1 = -.0000052883907$	$T_3L = -.000000001705881$

Table B.1: Region I coefficients

Region II The second region is based on measurements of refractive index in seawater in standard atmospheric conditions. The independent variables in this sub equation are therefore the salinity S, the wavelength L and the temperature T. The coefficients are presented in table B.2.

$$N_{II} = S_0 \cdot S + S_1LM_2 \cdot \frac{S}{L^2} + S_1T \cdot S \cdot T + S_1T_2 \cdot S \cdot T^2 \\ S_1T_3 \cdot S \cdot T^3 + STL \cdot S \cdot T \cdot L$$

$S_0 = .00019029121$	$S_1T_2 = .0000000089818478$
$S_1LM_2 = .0000024239607$	$S_1T_2 = 1.2078804 \cdot 10^{-10}$
$S_1T = -.0000007396029$	$STL = -.0000003589495$

Table B.2: Region II coefficients

Region III The third region is based on measurements of refractive index in pure water at high pressure. The independent variables in this sub equation are therefore the pressure P, the wavelength L and the temperature T. The coefficients are presented in table B.3.

$$N_{III} = P_1 \cdot P + P_2 \cdot P^2 + PLM_2 \cdot \frac{P}{L^2} + PT \cdot P \cdot T \\ PT_2 \cdot P \cdot T^2 + P_2T_2 \cdot P^2 \cdot T^2$$

$P_1 = .0000015868363$	$PT = -.0000000094634486$
$P_2 = -1.574074 \cdot 10^{-11}$	$PT_2 = 1.0100326 \cdot 10^{-10}$
$PLM_2 = .000000010712063$	$P_2T_2 = 5.8085198 \cdot 10^{-15}$

Table B.3: Region III coefficients

Region IV The fourth region is based on measurements of refractive index in seawater of constant salinity and at constant wavelength at high pressure. The

independent variables in this sub equation are therefore the pressure P and the temperature T. The coefficients are presented in table B.4.

$$N_{IV} = P_1S \cdot P \cdot S + PTS \cdot P \cdot T \cdot S + PT_2S \cdot P \cdot T^2 \cdot S$$

$P_1S = -.0000000011177517$
$PTS = 5.7311268 \cdot 10^{-11}$
$PT_2S = -1.5460458 \cdot 10^{-12}$

Table B.4: Region IV coefficients

Appendix C

Statistical representation of noise sources

In any measurement system, a sequence of repeated measurements will produce slightly differing values. This is caused by random errors or noise in the instrument electronics or the measured process. It causes an uncertainty in the measured result. We can calculate the mean value of the measured results to give the best representation of the measured value. The mean value $\bar{x}$ of a sequence of n samples x_i is defined as

$$\bar{x} = \frac{1}{n}\sum_{i=1}^{n} x_i.$$

We can define the standard deviation σ of the n values as

$$\sigma = \sqrt{\frac{\sum_{i=1}^{n}(x_i - \bar{x})^2}{n}}.$$

This defines how much the measured values differ from the mean value $\bar{x}$. If the mean value of a set of samples equals zero, the standard deviation σ equals the root-mean-square of the measured value.[70] The probability density function f describes the probability that the measurement will assume a certain value x_i. If the probability function is bell shaped with a maximum at the mean value $\bar{x}$, the measured values are said to be distributed according to a Gaussian distribution with a probability density function of

$$f(x; \bar{x}, \sigma) = Ae^{-\frac{1}{2}\left(\frac{x-\bar{x}}{\sigma}\right)^2},$$

where A is a constant depending on the number of samples and the standard deviation. Noise generated in physical systems are often considered to be gaussian. [38] To determine if a sequence of repeated measurements is distributed in a gaussian fashion one can plot the deviation of each measured value to the mean value in a histogram, along with the gaussian distribution function.

If the measured value x is an indirect measurement, where several input

quantities a_i are sequentially dependent, x is a function $x = f(a_1, a_2, ..., a_i)$ of these input quantities, the total standard deviation σ_{tot} will then be dependent on each input quantities standard deviation σ_i by the following relation [70]:

$$\sigma_{tot}^2 = \left(\frac{\partial x}{\partial a_1}\right)^2 \sigma_1^2 + \left(\frac{\partial x}{\partial a_2}\right)^2 \sigma_2^2 + ... \left(\frac{\partial x}{\partial a_i}\right)^2 \sigma_i^2.$$

Appendix D

Screenshots of LabView program

The following pages presents two screenshots of the Labview virtual instrument block diagrams. Figure D.1 describes the main program. It starts by initialization of the measurement channels before it starts the main loop of the program. The main loop consists of a case structure where one can choose to output the data to the screen, or to store it in a file. Inside the case structure we call the sub routine described in figure D.2. This routine reads the measurement channels, filters the data in a $10\,Hz$ digital filter and converts the measured voltages to relevant units. The position voltage input is converted to millimeter displacement output, and the temperature voltage is converted to ^oC output. The sub routine output is then stored to a file or presented on screen according to the case structure. The quadrant photodiode has a slightly different sub routine, since the conversion formula from voltage to position is different.

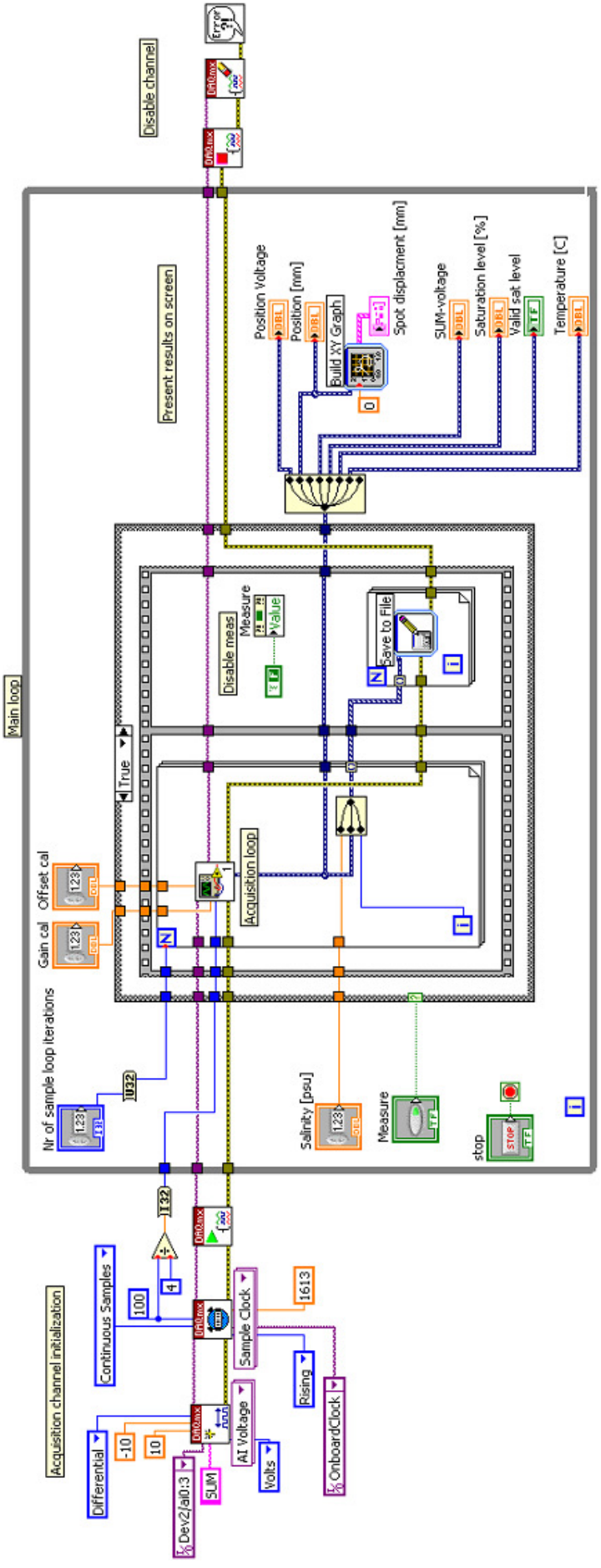

Figure D.1: Main virtual instrument block diagram

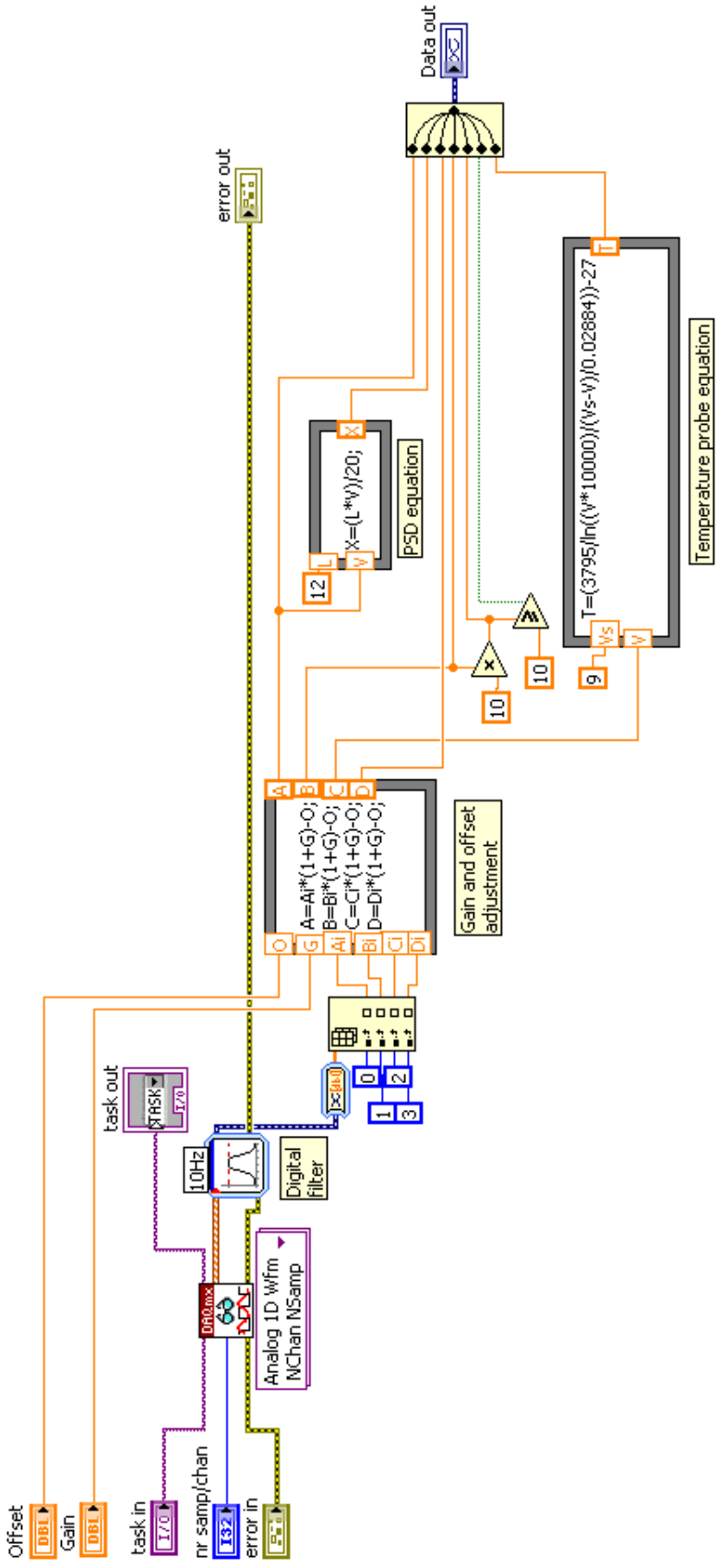

Figure D.2: Acquisition loop block diagram

Appendix E

Seawater composition

Ref [71] presents a description of the ionic composition of seawater with a mass fraction of dissolved ions of approximately $3.52\,{}^{g}/_{100g}$. The mass fractions of each ion is presented in the table below.

Ion	**Mass fraction** ${}^{g}/_{100g}$
Cl^-	1.9353
Na^+	1.0764
SO_4^{2-}	0.2701
Mg^{2+}	0.1297
Ca^{2+}	0.0406
K^+	0.0387
HCO_3^-	0.0142
Br^-	0.0066
Sr^{2+}	0.0014
H_3BO_3	0.0026
F^-	0.0001

Table E.1: Mass fractions of seawater ions